



Diploma Thesis

Modelling of mercury adsorption in natural gas pipelines

Eleni Grammenou

Supervisor: Epaminondas Voutsas, Professor

Athens, June 2019

ACKNOWLEDGMENTS

The present diploma thesis was conducted in the Thermodynamics and Transport Phenomena Laboratory at the School of Chemical Engineering of the National Technical University of Athens, during the academic year 2018-2019.

Firstly, I would like to use this opportunity to express my appreciation to my thesis' supervisor Professor Epaminondas Voutsas for his proper guidance, exceptional direction and expertise. This work could not have been completed without his unconditional support and motivation.

I am greatly thankful to Dr. Nefeli E. Novak for her invaluable assistance in this endeavor. I am truly indebted to her for the constant psychological and academic support.

Moreover, I would like to thank Professor Andreas Boudouvis for offering valuable comments on my thesis, Dr. Antonis Spyropoulos for devoting time to go through all the computational difficulties that occurred, Dr. Vassiliki Louli and Dr. Georgia Pappa for their instructional feedback.

I wholeheartedly thank Equinor ASA, Norway for giving me the opportunity to start this project as part of a summer internship and develop it further in my diploma thesis, as well as Dr. Efstathios Skouras, Dr. Eleni Panteli and Ms. Marlene Lund for their cooperation.

Finally, I wish to express my love and profound gratitude to my family: Hara, Giannis, Christina, Eleni and friends: Dimitris, Anastasia, Aris, Giorgos, Orestis for fueling me with continuous encouragement and optimism throughout my years of study, and through the process of researching and writing this thesis. This accomplishment would not have been possible without them.

Thank you.

ΔΙΠΛΩΜΑΤΙΚΗ ΕΡΓΑΣΙΑ

ΜΟΝΤΕΛΟΠΟΙΗΣΗ ΤΗΣ ΠΡΟΣΡΟΦΗΣΗΣ ΥΔΡΑΡΓΥΡΟΥ ΣΕ ΑΓΩΓΟΥΣ ΜΕΤΑΦΟΡΑΣ ΦΥΣΙΚΟΥ ΑΕΡΙΟΥ

ΠΕΡΙΛΗΨΗ

Ο υδράργυρος (Hg) και οι ενώσεις του απαντώνται εγγενώς στα ορυκτά καύσιμα, συμπεριλαμβανομένου του φυσικού αερίου (ΦΑ), του αργού πετρελαίου και του γαιάνθρακα. Κατά την εκμετάλλευση των κοιτασμάτων, ο στοιχειακός υδράργυρος και οι άλλες του μορφές που μπορεί να υπάρχουν στον ταμιευτήρα, βρίσκονται διαλυμένοι στις ξεχωριστές φάσεις (πετρέλαιο, αέριο και νερό) και ταξιδεύουν με αυτές κατά την παραγωγή και την επεξεργασία του πετρελαίου και του φυσικού αερίου. Αν και οι γεωλογικοί μηχανισμοί που εξηγούν την ύπαρξη του Hg στο αργό πετρέλαιο και το φυσικό αέριο δεν έχουν διερευνηθεί σε βάθος από την επιστημονική κοινότητα, η πιο πιθανή εξήγηση είναι η απελευθέρωση του υδραργύρου από τον φλοιό της Γης μέσω γεωλογικών δυνάμεων (πίεση και θερμοκρασία) και η μετανάστευσή του ως αέριο στους θύλακες όπου συσσωρεύεται το αργό πετρέλαιο και το φυσικό αέριο [1].

Η ποσότητα του υδραργύρου στους ταμιευτήρες, ολοένα και αυξάνεται, αφενός λόγω του εμπλουτισμού των ρευστών ταμιευτήρα σε υδράργυρο εξαιτίας της εξάντλησης των κοιτασμάτων και αφετέρου λόγω της ανάγκης για εκμετάλλευση μικρότερων και βαθύτερων κοιτασμάτων. Η συγκέντρωση υδραργύρου στο αργό πετρέλαιο και το φυσικό αέριο ποικίλλει σημαντικά, με βάση τη γεωλογική του προέλευση. Ορισμένες ποικιλίες αργού πετρελαίου που υποβάλλονται σε επεξεργασία στις ΗΠΑ εκτιμάται ότι περιέχουν από 1 έως 1000 ppb Hg (wt), με μέσο όρο κοντά στα 5 ppb [2]. Στα συμπυκνώματα φυσικού αερίου και στο φυσικό αέριο, οι συγκεντρώσεις υδραργύρου κυμαίνονται συνήθως από 1 έως 200 μικρογραμμάρια ανά πρότυπο κυβικό μέτρο (μg/Scm) [1]. Στο φυσικό αέριο, ο υδράργυρος υπάρχει σχεδόν αποκλειστικά στη στοιχειακή του μορφή (Hg⁰) και σε συγκεντρώσεις πολύ κάτω από τον κορεσμό, ενδεικτικό της απουσίας υγρής φάσης υδραργύρου στα περισσότερα κοιτάσματα [3]. Η μέση συγκέντρωση στοιχειακού υδραργύρου στο φυσικό αέριο δεν είναι γνωστή με στατιστική βεβαιότητα, αλλά θεωρείται ότι είναι μικρότερη από 10 μg/Scm [4].

Ακόμη και σε μικρές συγκεντρώσεις (λίγα ppb), οι διάφορες μορφές υδραργύρου μπορούν να προκαλέσουν σοβαρά προβλήματα κατά την επεξεργασία του πετρελαίου και του φυσικού αερίου. Οι συνέπειες του υδραργύρου στο φυσικό αέριο αναφέρθηκαν για πρώτη φορά το 1973, όταν προκλήθηκε διάβρωση εναλλάκτη θερμότητας αλουμινίου, που λειτουργούσε σε κρυογονικές συνθήκες, στο εργοστάσιο υγροποιημένου φυσικού αερίου Skikda, στην Αλγερία [5]. Η τελευταία γνωστοποιημένη περίπτωση ατυχήματος που σχετίζεται με τον υδράργυρο στη βιομηχανία φυσικού αερίου, είναι αυτή στην περιοχή Moomba της Αυστραλίας το 2004, όπου σημειώθηκε έκρηξη λόγω διάβρωσης από Hg ενός στομίου κρυογονικού εναλλάκτη [6]. Μέχρι σήμερα, περίπου 10 βιομηχανικά ατυχήματα συνδέονται με διάβρωση εξοπλισμού λόγω ύπαρξης υδραργύρου [7], καθιστώντας σαφές ότι η σωστή διαχείριση του υδραργύρου κατά την επεξεργασία του πετρελαίου και του φυσικού αερίου είναι κρίσιμης σημασίας.

Αν και ο υδράργυρος, ως στοιχείο του φυσικού αερίου, μεταφέρεται μέσω χαλύβδινων αγωγών, από τους ταμιευτήρες προς τις εγκαταστάσεις επεξεργασίας ΦΑ, ανιχνεύεται στην είσοδο των εγκαταστάσεων μετά από παρατεταμένο διάστημα λειτουργίας, λόγω της αργής συσσώρευσης του, μέσω μηχανισμών προσρόφησης, στους αγωγούς. Αυτό είναι γνωστό ως «φαινόμενο υστέρησης εμφάνισης του υδραργύρου (mercury lag effect)» [8]. Ο χρόνος που απαιτείται μέχρι η συγκέντρωσή του στην είσοδο της μονάδας επεξεργασίας να φθάσει ένα τυπικό κρίσιμο όριο, το οποίο καθορίζει την αναγκασιότητα

εγκατάστασης ή όχι μονάδας απομάκρυνσης του Hg από το ρεύμα του ΦΑ, ονομάζεται χρόνος για breakthrough.

Η αντίδραση και η ενσωμάτωση υδραργύρου στις χαλύβδινες επιφάνειες και η καθυστέρηση εμφάνισής του στην έξοδο του αγωγού, απαιτούν αυστηρά μέτρα ασφαλείας, όσον αφορά τη λειτουργία και τη συντήρηση του εξοπλισμού, καθώς η εκπομπή ατμών στοιχειακού υδραργύρου στο περιβάλλον εργασίας, είναι τοξική για τους εργαζομένους. Επιπρόσθετα, εκτός από την προσβολή των αγωγών, ο υδράργυρος έχει καταστρεπτική επίδραση στον εξοπλισμό, κυρίως στις μονάδες κρυογονικής επεξεργασίας, και τους καταλύτες. Εξαιτίας της ικανότητάς του να σχηματίζει αμαλλάματα με άλλα μέταλλα (Al, Cu, Zn, Ni κ.ά.), προκαλεί διάβρωση στον εξοπλισμό είτε γιατί τα αμαλλάματα είναι πιο εύθραυστα από το καθαρό μέταλλο είτε γιατί, όπως στην περίπτωση του αλουμινίου, το αμάλγαμα αντιδρά με το νερό προς σχηματισμό οξειδίου του μετάλλου και ελεύθερου Hg, με αποτέλεσμα να επαναλαμβάνεται η διαδικασία της διάβρωσης μέχρι όλο το Al να οξειδωθεί [9].

Παρά την πρόοδο στην κατανόηση των μηχανισμών και τη διαθεσιμότητα συστημάτων πρόληψης της μόλυνσης του εξοπλισμού με υδράργυρο, η ύπαρξη πειραματικών δεδομένων σχετικά με την κινητική και τους μηχανισμούς προσρόφησης υδραργύρου στα τοιχώματα των χαλύβδινων αγωγών είναι περιορισμένη. Το γεγονός αυτό, σε συνδυασμό με την εμπιστευτική πολιτική της βιομηχανίας πετρελαίου και φυσικού αερίου σχετικά με τη δημοσίευση αξιόπιστων δεδομένων, καθιστά πρόκληση την ανάπτυξη ενός μοντέλου προσρόφησης υδραργύρου σε αγωγούς.

Ο σκοπός της παρούσας Διπλωματικής Εργασίας είναι η ανάπτυξη ενός μοντέλου για την προσρόφηση/εκρόφιση υδραργύρου στους αγωγούς μεταφοράς φυσικού αερίου, το οποίο βασίζεται στην απλοποιημένη προσέγγιση της συσσώρευσης υδραργύρου, λόγω φυσικής προσρόφησης του στην χαλύβδινη επιφάνεια ενός αγωγού. Το μοντέλο εκτιμά το χρόνο που απαιτείται για να φθάσει η συγκέντρωση υδραργύρου στην είσοδο της μονάδας επεξεργασίας το κρίσιμο όριο, που τυπικό ορίζεται ίσο με 10 ng/Sm^3 . Επιπλέον, παράγει τα χρονικά εξαρτώμενα προφίλ συγκεντρώσεων και κάλυψης της επιφάνειας του αγωγού για πλήθος συγκεντρώσεων εισόδου ($100\text{-}5000 \text{ ng/Sm}^3$) και για διαφορετικές τιμές προσροφητικής ικανότητας του αγωγού ($0.0038\text{-}10 \text{ g/m}^2$). Το μοντέλο κατασκευάστηκε με τη χρήση του λογισμικού MATLAB [10].

Αρχικά, διεξάγεται βιβλιογραφική ανασκόπηση σχετικά με πιθανές μεθόδους συσσώρευσης υδραργύρου σε μεταλλικές επιφάνειες. Η προσρόφηση είναι μια διεργασία κατά την οποία ένα ή περισσότερα συστατικά που περιλαμβάνονται σε ένα υγρό ή αέριο ρεύμα μεταφέρονται εκλεκτικά (προσροφημένες ουσίες) στην επιφάνεια ενός στερεού (προσροφητικό μέσο/προσροφητή), σχηματίζοντας ένα μοριακό ή ατομικό φιλμ [11]. Η εκρόφιση περιγράφει την αντίστροφη διαδικασία. Ανάλογα με τη φύση των διαμοριακών δυνάμεων μεταξύ του προσροφητή και της προσροφημένης ουσίας, η προσρόφηση μπορεί να χωριστεί σε δύο κατηγορίες: φυσική προσρόφηση και χημική προσρόφηση (χημειορρόφιση)[12].

Η πλειονότητα των επιστημονικών ευρημάτων για την προσρόφηση υδραργύρου σε επιφάνειες, επικεντρώνεται στην προσρόφηση υδραργύρου σε μονοκρυσταλλικά υλικά, ενώ για πολυκρυσταλλικά είναι πολύ περιορισμένη. Η βιβλιογραφία περιλαμβάνει την μελέτη προσρόφησης υδραργύρου σε μονοκρύσταλλους αργύρου και χρυσού [13], καθώς και σε μονοκρυσταλλικές και πολυκρυσταλλικές επιφάνειες χαλκού [14, 15], ψευδαργύρου [14, 15], και σιδήρου [14, 16, 17]. Η αξιολόγηση της προσρόφησης σε πολυκρυσταλλικά δειγμάτων έλαβε χώρα τόσο σε θερμοκρασία δωματίου (RT) 298 K όσο και σε χαμηλή θερμοκρασία (LT) που κυμαίνεται από 82-111K. Επιπλέον, διερευνήθηκε η επίδραση της "μόλυνσης" στο μηχανισμό προσρόφησης υδραργύρου για τα ίδια διαστήματα θερμοκρασίας, με προεπεξεργασία των καθαρών πολυκρυσταλλικών επιφανειών με χλώριο και οξυγόνο [14].

Οι πειραματικές μετρήσεις για μονοκρυσταλλικές επιφάνειες [13, 14, 16], ουσιαστικά, επιβεβαιώνουν την ισχυρή εξάρτηση της ρόφησης από την θερμοκρασία και αποκαλύπτουν τις ισχυρές αλληλεπιδράσεις μεταξύ των ατόμων υδραργύρου που

προσροφώνται. Οι αλληλεπιδράσεις αυτές, λόγω της απωστικής φύσης τους, είναι υπαίτιες για μείωσης του ενεργειακού φράγματος που πρέπει να υπερπηδήσουν τα άτομα του υδραργύρου κατά την εκρόφηση, μέγεθος γνωστό και ως «ενέργεια ενεργοποίησης εκρόφησης». Έτσι, με αύξηση του ποσοστού κορεσμού, αναμένεται μείωση της ενέργειας ενεργοποίησης εκρόφησης. Επιπλέον, γίνεται αναφορά στην εμφάνιση του «compensation effect» το οποίο αφορά ισχυρή συσχέτιση μεταξύ του προεκθετικού παράγοντα της εκρόφησης, v , και της ενέργειας ενεργοποίησης εκρόφησης σε μηδενική κάλυψη επιφάνειας, E_0 [18]. Συνοψίζοντας τα αποτελέσματα της προσρόφησης υδραργύρου σε πολυκρυσταλλικές επιφάνειες [14, 15, 17], διαπιστώνεται ότι οι χαμηλές θερμοκρασίες συμβάλλουν στην προσρόφηση υδραργύρου λόγω της φυσικής προσρόφησης. Το χλώριο ευνοεί την προσρόφηση υδραργύρου, καθώς παρουσιάζεται αυξημένη κάλυψη υδραργύρου σε χαμηλές θερμοκρασίες στον πολυκρυσταλλικό σίδηρο, χαλκό και ψευδάργυρο. Το οξυγόνο, ωστόσο, βρέθηκε ότι δρα ανασταλτικά στην ρόφηση του υδραργύρου, ιδιαίτερα σε θερμοκρασία δωματίου. Με βάση την ανασκόπηση της βιβλιογραφίας, με έμφαση στις πολυκρυσταλλικές επιφάνειες σιδήρου, συνάγεται το συμπέρασμα ότι σε θερμοκρασία δωματίου, οι οποίες είναι πιο κοντά στη θερμοκρασία λειτουργίας του αγωγού, η προσρόφηση υδραργύρου περιορίζεται στον σχηματισμό μονοστοιβάδας. Ωστόσο, καθώς οι αγωγοί φυσικού αερίου είναι κατασκευασμένοι από χάλυβα, κράμα δηλαδή σιδήρου και άνθρακα, κρίνεται αναγκαία η μελέτη των μηχανισμών συσσώρευσης υδραργύρου σε χαλύβδινες επιφάνειες.

Οι Wilhelm & Nelson [19] κατέληξαν ότι ένας ή περισσότεροι από τις ακόλουθους μηχανισμούς είναι υπεύθυνοι για τη ρόφηση υδραργύρου στον εξοπλισμό και στους αγωγούς.

α) Φυσική προσρόφηση στην επιφάνεια του χάλυβα.

β) Φυσική προσρόφηση σε επιφανειακές εναποθέσεις οξειδίου σιδήρου και θείουχου σιδήρου.

γ) Αντίδραση με H_2 / και ενσωμάτωση σε εναποθέσεις της επιφάνειας.

δ) Προσρόφηση στο κρυσταλλικό πλέγμα του χάλυβα.

ε) Προσρόφηση στα όρια των κόκκων του χάλυβα και αντίδραση με τοπικές ενώσεις.

στ) Σχηματισμός αμαλλάματος μεταξύ υδραργύρου και χάλυβα.

Σε συμφωνία με τα ευρήματα των Jones και Perry [16], η έρευνα των Wilhelm & Nelson [19] απορρίπτει την ρόφηση του υδραργύρου στο κρυσταλλικό πλέγμα του σιδήρου λόγω του σχετικού μεγέθους των ατόμων υδραργύρου. Η διάμετρος των ατόμων Hg ισούται με 0.296 nm, και είναι μεγαλύτερη του διαθέσιμου χώρου ανάμεσα στα άτομα Fe, η διάμετρος των οποίων είναι 0.287 nm. Επιπλέον, η πιθανότητα αντίδρασης προς σχηματισμό αμαλλάματος σε αγωγούς μεταφοράς αερίου δεν υφίσταται, δεδομένης της αέριας φάσης του υδραργύρου στο εσωτερικό των αγωγών. Πειράματα σε μικρά χαλύβδινα δείγματα (steel coupons) εκτεθειμένα σε ατμούς υδραργύρου αποκάλυψαν ότι η ρόφηση στο κρυσταλλικό πλέγμα του χάλυβα ή στα όρια των κόκκων δεν λαμβάνει στους χαλύβδινους αγωγούς, εφόσον δεν παρατηρήθηκε μεταβολή στις μηχανικές τους ιδιότητες [19].

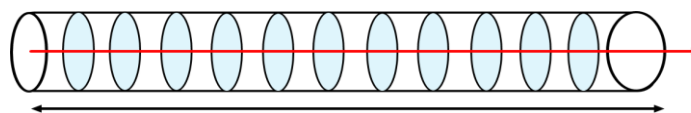
Ως αποτέλεσμα, η χημειορρόφηση στις εναποθέσεις της επιφάνειας και η φυσική προσρόφηση φαίνεται να είναι οι κύριοι μηχανισμοί συσσώρευσης υδραργύρου. Ωστόσο, ο σχηματισμός θείουχου υδραργύρου (HgS), όταν ο υδράργυρος αντιδρά με το υδρόθειο (H_2S) που βρίσκεται διαλελυμένο στο φυσικό αέριο, καθώς και η εμφάνιση χημικά ενσωματωμένου Hg^{2+} στο οξείδιο του σιδήρου, αντιστοιχούσαν σε λιγότερο από 10% του συνολικού υδραργύρου που προσροφήθηκε από το εξεταζόμενο δείγμα. Αυτή η παρατήρηση καθιστά τη φυσική προσρόφηση υπεύθυνη για τη συσσώρευση υδραργύρου κατά μήκος του αγωγού [19].

Εν συνεχεία, ερευνάται η ύπαρξη μοντέλων προσρόφησης υδραργύρου σε αγωγούς στην βιβλιογραφία. Οι δημοσιευμένες επιστημονικές εργασίες επικεντρώνονται, κατά κύριο λόγο, στη μεταφορά ρύπων, όπως το αρσενικό και το χλώριο, στα συστήματα διανομής νερού (WDS)[20-22]. Οι σιδερένιοι σωλήνες, που χρησιμοποιούνται για τη

μεταφορά πόσιμου νερού, υπόκεινται διάβρωση, γεγονός που δημιουργεί πολυάριθμες ανησυχίες για την ποιότητα του νερού. Λόγω αυτών των ανησυχιών, η ανάπτυξη μοντέλων που περιλαμβάνουν φαινόμενα προσρόφησης, εκρόφησης και μεταφοράς μάζας ενήργησε ως απαραίτητη επέκταση στο λογισμικό μοντελοποίησης του συστήματος διανομής νερού EPANET που αναπτύχθηκε από τον Οργανισμό Προστασίας Περιβάλλοντος της Αμερικάνικης κυβέρνησης [23, 24]. Με βάση τα μοντέλα προσρόφησης ρύπων σε αγωγούς νερού, με κατάλληλη προσαρμογή στην πολυπλοκότητα της ρόφησης διαλυμένου στην αέρια φάση υδραργύρου σε αγωγούς μεταφοράς ΦΑ, προκύπτουν οι κύριες μεταβλητές του μελετώμενου φαινομένου και ακολούθως, επιτρέπεται η μαθηματική του διατύπωση.

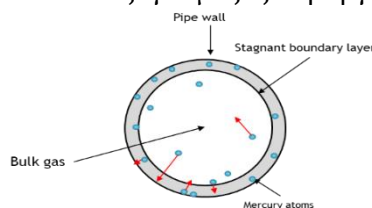
Η προσρόφηση υδραργύρου σε αγωγούς ΦΑ περιγράφεται από τρία ξεχωριστά φαινόμενα, την αξονική ροή του αερίου (και συνεπώς του αερίου υδραργύρου) εντός του αγωγού, την ακτινική ροή υδραργύρου από τον κύριο όγκο του αερίου (bulk gas) στο στάσιμο οριακό στρώμα κοντά στα τοιχώματα του αγωγού (stagnant boundary layer) και την προσρόφηση υδραργύρου στην επιφάνεια του χάλυβα. Ομοίως, η αντίστροφη διαδικασία μπορεί να λάβει χώρα, όπου ένα άτομο υδραργύρου μπορεί να εκροφηθεί από το τοίχωμα του αγωγού και να διαχυθεί πίσω στον κύριο όγκο του ρευστού. Το φαινόμενο θεωρείται ισόθερμο.

Για την περιγραφή της ροής του αερίου στην αξονική διεύθυνση, επιλέγεται η διακριτοποίηση του αγωγού σε τμήματα, όπως απεικονίζεται στο Σχήμα 1. Εντός κάθε τμήματος, γίνεται η παραδοχή ότι η ροή του αερίου στον κύριο όγκο ρευστού είναι καλά αναμειγμένη, λόγω της τυρβώδους φύσης της και ως αποτέλεσμα, η σύνθεση του αερίου και όλες οι εντατικές και εκτατικές ιδιότητές του είναι ομοιόμορφες. Η διακριτοποίηση του αγωγού χρησιμοποιείται επιπροσθέτως για την εκτίμηση της πτώσης πίεσης λόγω τριβών. Η αξονική ροή του υδραργύρου περιγράφεται μαθηματικά από το αντίστοιχο ισοζύγιο μάζας στον κύριο όγκο του αερίου.



Σχήμα 1. Διακριτοποίηση αγωγού στην αξονική διεύθυνση.

Ο υδράργυρος ρέει επίσης στην ακτινική κατεύθυνση από τον κύριο όγκο ρευστού προς το στάσιμο στρώμα, όπως απεικονίζεται στο Σχήμα 2. Η κλασική προσέγγιση του οριακού στρώματος χρησιμοποιείται για τον προσδιορισμό του ρυθμού μεταφοράς μάζας κατά την προσρόφηση και την εκρόφηση του υδραργύρου. Τα άτομα υδραργύρου διαχέονται από τον κύριο όγκο μέσω του στάσιμου οριακού στρώματος, το οποίο αντιπροσωπεύει όλη την αντίσταση μεταφοράς μάζας, προτού ροφηθούν στις κενές θέσεις του χαλύβδινου τοιχώματος. Η συγκέντρωση υδραργύρου στο εσωτερικό του οριακού στρώματος κοντά στην επιφάνεια του αγωγού θεωρείται ότι βρίσκεται σε ισορροπία με τον προσροφημένο υδράργυρο στην επιφάνεια του αγωγού. Η τυρβώδης ροή του ΦΑ που οδηγεί στην καλή ανάμιξη του αερίου, επιτρέπει την παραδοχή του σταθερού προφίλ ακτινικής συγκέντρωσης. Στην αξονική κατεύθυνση, η ταχύτητα θεωρείται μηδενική στο στάσιμο οριακό στρώμα. Επομένως, οποιαδήποτε αξονική μεταφορά μάζας θεωρείται αμελητέα. Η συγκέντρωση υδραργύρου στο στάσιμο στρώμα διαμορφώνεται μαθηματικά από το ισοζύγιο μάζας υδραργύρου στο στάσιμο στρώμα.



Σχήμα 2. Απεικόνιση της μεταφοράς μάζας Hg στην ακτινική διεύθυνση.

Δεδομένου ότι η ρόφηση είναι δυναμικό φαινόμενο, η αντίστροφη διαδικασία της εκρόφησης από την επιφάνεια και της διάχυσης στον κύριο όγκο του λαμβάνουν χώρα ταυτόχρονα. Όταν το σύστημα φθάσει σε θερμοδυναμική ισορροπία, ο ρυθμός προσρόφησης και εκρόφησης εξισώνονται. Η προσρόφηση μοντελοποιείται ως μη ενεργοποιημένη, φυσική προσρόφηση μέχρι σχηματισμού μονοστρώματος υδραργύρου, ενώ η εκρόφηση ως χημική αντίδραση μεταξύ των ατόμων υδραργύρου της επιφάνειας και αυτών που εκροφώνται.

Τα φαινόμενα που μελετώνται στις δύο διευθύνσεις περιγράφονται από τρεις συνήθεις διαφορικές εξισώσεις (Εξ.1-Εξ.3). Η αξονική ροή του υδραργύρου περιγράφεται μαθηματικά από την αντίστοιχο ισοζύγιο μάζας του Hg στον κύριο όγκο του αερίου με συγκέντρωση $C_{bulk(Hg)}$, Εξ. 1, η συγκέντρωση υδραργύρου στο στάσιμο στρώμα, $C_{stagnant(Hg)}$, προκύπτει από το ισοζύγιο μάζας υδραργύρου στο στάσιμο στρώμα (Εξ. 2), ενώ η Εξ. 3 εκφράζει το ρυθμό προσρόφησης και εκρόφησης σε όρους κάλυψης επιφάνειας του αγωγού, θ . Τα υπόλοιπα μεγέθη που λαμβάνουν μέρος στις διαφορικές εξισώσεις είτε υπολογίζονται από την καταστατική εξίσωση UMR-PRU [25], η οποία έχει αποδεδειγμένα καλή απόδοση στα μίγματα φυσικού αερίου, είτε από κατάλληλες σχέσεις στην πίεση και θερμοκρασία του εκάστοτε διακριτού τμήματος.

$$\frac{dC_{bulk(Hg)}(t,n)}{dt} = \frac{F_{vol\ in}^{v}(total)(n)[C_{bulk(Hg)}(t,(n-1))-C_{bulk(Hg)}(t,n)]+k_m(n)A_{stagnant}[C_{stagnant(Hg)}(t,n)-C_{bulk(Hg)}(t,n)]}{V_{bulk}(n)} \quad \text{Εξ. 1}$$

$$\frac{dC_{stagnant(Hg)}(t,n)}{dt} = \frac{k_m(n)A_{stagnant}[C_{bulk(Hg)}(t,n)-C_{stagnant(Hg)}(t,n)]-\frac{d\theta(t,n)}{dt}A_{pipe}q_{max}SSA}{V_{stagnant}(n)} \quad \text{Εξ. 2}$$

$$\frac{d\theta(t,n)}{dt} = Rate_{ads} - Rate_{des} = \frac{\varphi_{(Hg)}^{v}C_{stagnant(Hg)}(t,n)ZRTN_A}{M_w(Hg)\sqrt{2\pi M_w(Hg)RT}} \cdot \frac{s_o(1-\theta(t,n))}{N_{max}} - v\theta(t,n)\exp\left[-\frac{(151-28.82\theta(t,n))}{RT}\right] \quad \text{Εξ. 3}$$

Το σύστημα των τριών διαφορικών εξισώσεων επιλύεται διαδοχικά για όλα τα τμήματα σε κάθε χρονική στιγμή. Κατά την ανάπτυξη του μοντέλου, οι μεταβλητές καταχωρούνται είτε ως χωρικά εξαρτώμενες είτε ως χωρο-χρονικά εξαρτώμενες. Επιπλέον, ο χρόνος αποτελεί συνεχή μεταβλητή, ενώ ο χώρος είναι διακριτή μεταβλητή.

Το μοντέλο επιλύεται χρησιμοποιώντας τον ενσωματωμένο MATLAB solver ode15s για άκαμπτα (stiff) συστήματα συνήθων διαφορικών εξισώσεων.

Στην ανάλυση πεπερασμένων στοιχείων, η πυκνότητα του πλέγματος είναι ένα κρίσιμο θέμα που σχετίζεται στενά με την ακρίβεια της λύσης, ενώ καθορίζει άμεσα το επίπεδο πολυπλοκότητάς του μοντέλου [26]. Ωστόσο, πλέγματα υψηλότερης πυκνότητας συνήθως χρειάζονται περισσότερο χρόνο για να επιλυθούν. Για το λόγο αυτό, εξετάστηκε διακριτοποίηση του αγωγού σε 50 έως 1000 τμήματα. Διαπιστώθηκε ότι κατάτμηση του αγωγού σε 500 τμήματα και άνω, δεν έχει επίδραση στην ακρίβεια των αποτελεσμάτων του μοντέλου. Δεδομένου ότι η επιλογή του αριθμού των τμημάτων στο παρόν μοντέλο γίνεται με κριτήριο την ακρίβεια της λύσης αλλά αποτελεί «συμβιβασμό» μεταξύ του υπολογιστικού χρόνου και της ακρίβειας της λύσης, επιλέχθηκαν 800 τμήματα.

Για την επίλυση των διαφορικών εξισώσεων, είναι απαραίτητος ο προσδιορισμός των αρχικών οριακών συνθηκών και της συνθήκης εξόδου. Συγκεκριμένα, όταν το ΦΑ εισέρχεται για πρώτη φορά στον αγωγό:

- i. Το τοίχωμα του αγωγού θεωρείται ομαλό και απαλλαγμένο από αποθέσεις.
- ii. Η συγκέντρωση του υδραργύρου του στάσιμου οριακού στρώματος ορίζεται μηδενική.
- iii. Η κάλυψη της επιφάνειας του προσροφημένου υδραργύρου ορίζεται μηδενική.

Η συγκέντρωση υδραργύρου στην έξοδο του αγωγού (είσοδος της μονάδας επεξεργασίας ΦΑ) περιορίζεται στα 10 ng/Sm³, που αποτελεί την κρίσιμη συγκέντρωση υδραργύρου στην έξοδο του αγωγού.

Το δυναμικό μοντέλο προσρόφησης υδραργύρου σε αγωγούς φυσικού αερίου εφαρμόζεται σε αγωγό 20 χιλιομέτρων που λειτουργεί στους 6°C. Το φυσικό αέριο εισέρχεται στον αγωγό στα 143.2 bara, με σύνθεση και παροχή, όπως περιγράφονται λεπτομερώς στον Πίνακα 1. Ο αγωγός καταταμείται σε 800 μέρη.

Πίνακας 1. Δεδομένα εισόδου ΦΑ και χαρακτηριστικά μεγέθη αγωγού.

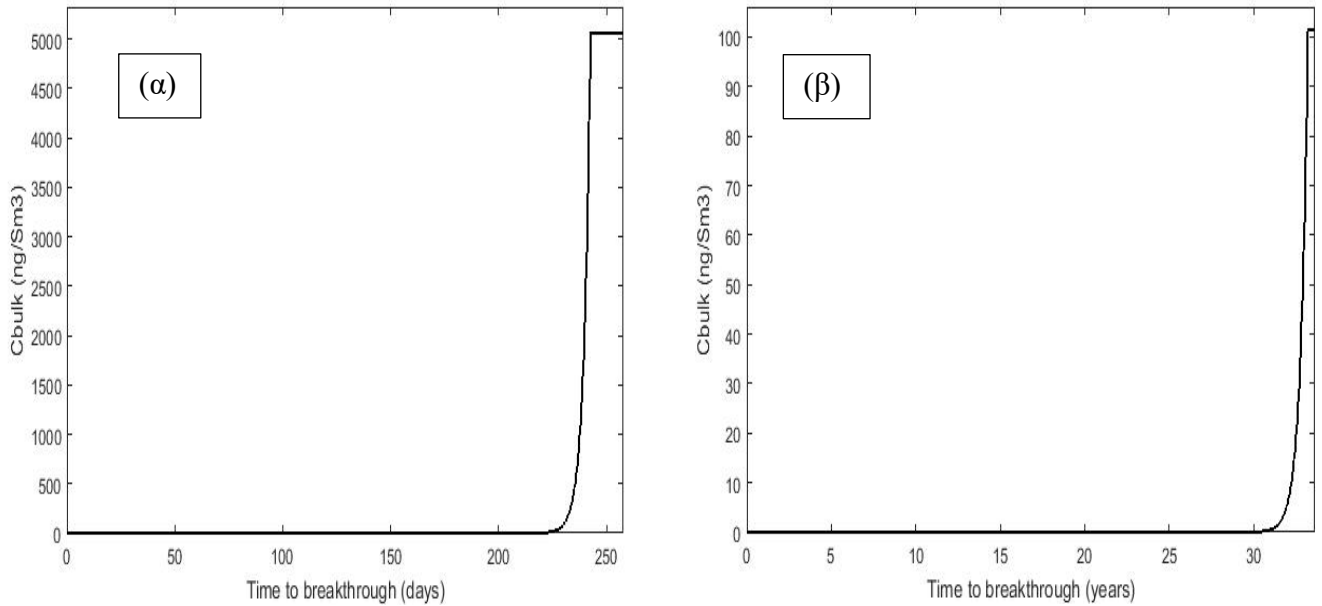
Παράμετρος	Τιμή
P _{in}	143.2 bara
F _{vol,in total}	24E6 Sm ³ /d
T	279.15 K
L	20,000 m
d _{pipe}	0.7112 m
n	800
Σύσταση ΦΑ	
Συστατικό	Γραμμομοριακό κλάσμα
Υδράργυρος	5.87462E-10
Διοξείδιο του άνθρακα	2.86724E-2
Μεθάνιο	8.04302E-1
Αιθάνιο	9.4531E-2
Προπάνιο	4.45561E-2
Ισοβουτάνιο	5.77915E-3
κ-Βουτάνιο	1.14475E-2
Ισοπεντάνιο	2.30854E-3
κ-Πεντάνιο	2.26116E-3
Νερό	6.60068E-8
Άζωτο	6.14254E-3

Τα αποτελέσματα της προσομοίωσης για 12 διαφορετικές περιπτώσεις καταγράφονται στον Πίνακα 2. Οι περιπτώσεις αφορούν 3 διαφορετικές συγκεντρώσεις εισόδου υδραργύρου 5000, 1000 και 100 ng/Sm³ και για κάθε περίπτωση καλύπτουν 4 διαφορετικές τιμές προσροφητικής ικανότητας της επιφάνειας του αγωγού. Η μικρότερη προκύπτει από τα πειράματα των Jones & Perry [16], δύο μέτριες εκτιμήσεις από τη μελέτη Wilhelm και Nelson [19] για βιομηχανικό αγωγό ΦΑ και μια υψηλή τιμή.

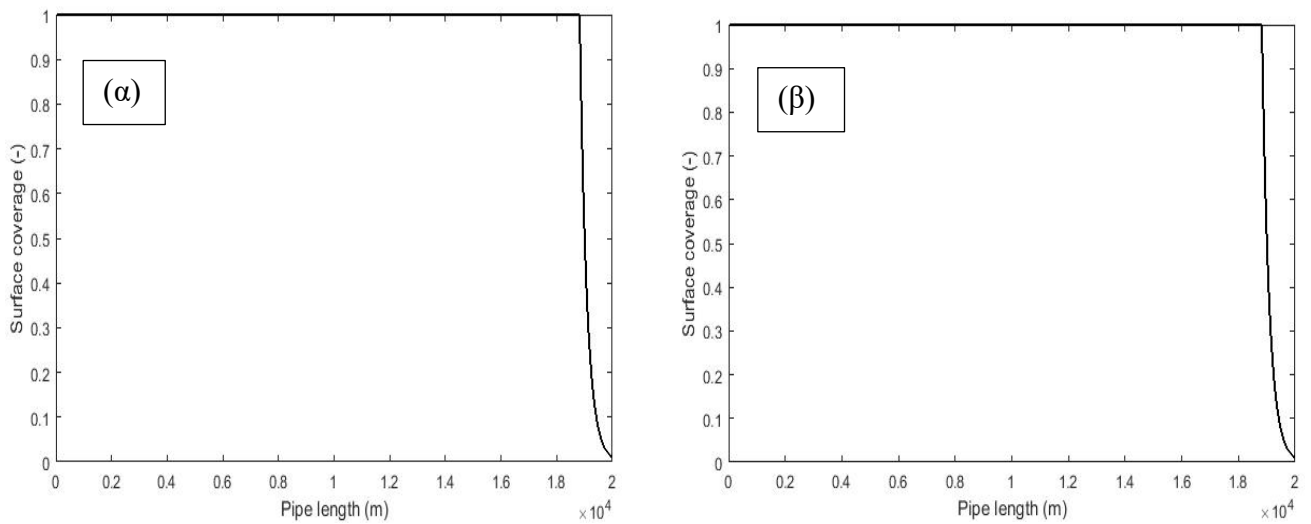
Πίνακας 2. Αποτελέσματα μοντέλου προσρόφησης Hg σε αγωγούς ΦΑ.

Μελετώμενη περίπτωση	Συγκέντρωση Hg στην είσοδο (ng Hg/Sm ³ ΦΑ)	Ειδική Επιφάνεια-SSA(m ² /m ²)	Χρόνος που απαιτείται ώστε η συγκέντρωση εξόδου να φθάσει τα 10 ng/Sm ³	
			hours	years
1-0	5000	1	1.5	-
1-1	5000	160	223.4	-
1-2	5000	263	367.1	1.0
1-3	5000	2632	3673.3	10.1
2-0	1000	1	7.2	-
2-1	1000	160	1141.8	3.1
2-2	1000	263	1876.8	5.1
2-3	1000	2632	18781.9	51.5
3-0	100	1	73.6	-
3-1	100	160	11759.1	32.2
3-2	100	263	19329.0	53.0
3-3	100	2632	193436.3	530.0

Ενδεικτικά, τα προφίλ συγκέντρωσης στην έξοδο του αγωγού με το χρόνο από την αρχή του φαινομένου ως τον πλήρη κορεσμό του αγωγού, παρουσιάζονται για τιμή ειδικής επιφάνειας (SSA) ίση με $160 \text{ m}^2/\text{m}^3$ για δύο διαφορετικές συγκεντρώσεις εισόδου υδραργύρου στα Σχήματα 3(α) και (β). Επιπρόσθετα, στα Σχήματα 4(α) και (β), παρατίθεται το μέτωπο κάλυψης του αγωγού την χρονική στιγμή του breakthrough, για την ίδια συγκέντρωση εισόδου αλλά για διαφορετικές τιμές SSA.



Σχήμα 3. Συγκέντρωση υδραργύρου στην έξοδο του αγωγού συναρτήσει του χρόνου για συγκέντρωση εισόδου υδραργύρου (α) $5000 \text{ ng}/\text{Sm}^3$ και $SSA=160$ και (β) $100 \text{ ng}/\text{Sm}^3$ και $SSA=160$.



Σχήμα 4. Μέτωπο κάλυψης του αγωγού για συγκέντρωση εισόδου υδραργύρου $1000 \text{ ng}/\text{Sm}^3$ και (α) $SSA=160$ (β) $SSA=263$.

Τα αποτελέσματα είναι ενδεικτικά των κύριων τάσεων:

- a. Για χρόνους που προηγούνται της αύξησης της συγκέντρωσης υδραργύρου στο κρίσιμο όριο των 10 ng/Sm^3 , δεν ανιχνεύεται υδράργυρος στην έξοδο του αγωγού.
- b. Αύξηση της συγκέντρωσης του υδραργύρου στην είσοδο, οδηγεί, ως αναμένεται, σε μείωση του χρόνου που απαιτείται για breakthrough για την ίδια τιμή ειδικής επιφάνειας (SSA) του χαλύβδινου αγωγού. Ο χρόνος αυτός είναι σχεδόν αντιστρόφως ανάλογος της συγκέντρωσης του υδραργύρου στην είσοδο.
- c. Ο χρόνος μέχρι η συγκέντρωση στην έξοδο να φθάσει την κρίσιμη τιμή, μεταβάλλεται αναλογικά με την προσροφητική ικανότητα ή ισοδύναμα με την ειδική επιφάνεια (SSA) για την ίδια εισερχόμενη συγκέντρωση υδραργύρου.
- d. Η τιμή SSA δεν επηρεάζεται το μέτωπο της ρόφησης.
- e. Οι παρατηρήσεις b και c οδηγούν στην εξαγωγή μιας επιτυχημένης σχέσης μεταξύ του χρόνου για breakthrough, της ειδικής επιφάνειας του αγωγού και της συγκέντρωση εισόδου υδραργύρου.

Η παραμετρική ανάλυση ευαισθησίας είναι μια συστηματική προσέγγιση για την πρόβλεψη της ευαισθησίας του μοντέλου σε πιθανές αλλαγές. Επιδιώκοντας να διασφαλισθεί η αξιοπιστία των αποτελεσμάτων και να κατανοηθούν καλύτερα οι σχέσεις μεταξύ των μεταβλητών εισόδου και εξόδου, προσδιορίζονται οι αβέβαιες παράμετροι και διερευνάται η επίδρασή τους στον χρόνο του breakthrough και στην κάλυψη της επιφάνειας. Σε προκαταρκτικό στάδιο, υπολογίζονται οι παράγωγοι των μεταβλητών του μοντέλου, C_{bulk} , $C_{stagnant}$ και θ , βάσει των παραμέτρων που εμφανίζουν αβεβαιότητα και αυτές είναι ο συντελεστής μεταφοράς μάζας, k_m , ο συντελεστής τάσης διαφυγής υδραργύρου, φ^{Hg} και ο συντελεστής συμπίεστότητας, Z . Ο συντελεστής μεταφοράς μάζας, k_m , εμφανίζεται να συμβάλλει σημαντικά στα αποτελέσματα του μοντέλου. Εντούτοις, διερευνάται, ενδελεχώς η επίδραση όλων των προαναφερθεισών παραμέτρων, η παραδοχή που αφορά το πάχος του στάσιμου οριακού στρώματος στα όρια του τοιχώματος του αγωγού που υπεισέρχεται στα ισοζύγια μάζας με τους όρους των όγκων ελέγχου, καθώς και παραμέτρων που σχετίζονται με την κινητική, όπως ο προεκθετικός παράγοντας του ρυθμού εκρόφησης, ν , και η ενέργεια ενεργοποίησης της εκρόφησης, $E_{\alpha,des}$.

Παρατηρείται ότι μία μικρή μείωση του συντελεστή μεταφοράς μάζας, k_m , συμβάλλει σε πιο μικρό αλλά επίμηκες μέτωπο ρόφησης και απότομη πτώση του χρόνου για breakthrough. Ο συντελεστής μεταφοράς μάζας, k_m , εξαρτάται από το ιξώδες, την πυκνότητα και τον συντελεστή διάχυσης του αερίου. Ως εκ τούτου, είναι μέγεθος που περιέχει σημαντικές ανασφάλειες και η ακριβής εκτίμησή του αποτελεί προϋπόθεση για την επιτυχή ανάπτυξη του μοντέλου. Όσον αφορά το συντελεστή συμπίεστότητας του ΦΑ, Z , μια μεταβολή $\pm 10\%$ στην τιμή του, όπως αυτή υπολογίστηκε με το μοντέλο UMR-PRU [25], οδηγεί σε μετατόπιση του προφίλ κάλυψης του αγωγού. Αύξηση του Z , οδηγεί σε μικρότερη και πιο απότομη κάλυψη της επιφάνειας του, και όπως είναι αναμενόμενο, μείωση του χρόνου που απαιτείται για να φθάσει η συγκέντρωση του υδραργύρου στην έξοδο τα 10 ng/Sm^3 . Τα αποτελέσματα του μοντέλου δεν παρουσιάζουν καμία ευαισθησία στην αλλαγή του συντελεστή τάσης διαφυγής, $\varphi^{(Hg)}$ καθώς και στις μεταβολές του πάχους του οριακού στρώματος.

Οι κινητικές παράμετροι της ρόφησης και της εκρόφησης είναι ιδιαίτερα αβέβαια μεγέθη, δεδομένης της έλλειψης πειραματικών δεδομένων που να περιγράφουν, λεπτομερώς, την κινητική προσρόφησης υδραργύρου σε χάλυβα. Για το λόγο αυτό, στην παρούσα Διπλωματική Εργασία, χρησιμοποιήθηκαν δεδομένα που προκύπτουν από πειράματα ρόφησης σε μονοκρυστάλλους σιδήρου [16]. Η ανάλυση ευαισθησίας επιβεβαιώνει την ύπαρξη του "compensation effect" μεταξύ του ν και το E_0 και υπογραμμίζει τη σημασία της χρήσης τους ως ζεύγη, στην έκφραση του ρυθμού της εκρόφησης για αξιόπιστα αποτελέσματα. Μεταβάλλοντας κάθε παράγοντα ξεχωριστά, παρατηρείται μεταβολή στο χρόνο του breakthrough και στην κάλυψη της επιφάνειας. Η σχέση μεταξύ της ενέργειας ενεργοποίησης και της κάλυψης της επιφάνειας εμφανίζεται

δεύτερου βαθμού, ωστόσο δεν επηρεάζονται τα αποτελέσματα του μοντέλου, όταν χρησιμοποιείται γραμμική συνάρτηση των μεγεθών.

Μετά από μια επιτυχημένη ανάλυση ευαισθησίας, το μοντέλο αναπτύσσεται χρησιμοποιώντας το εργαλείο Aspen Plus Custom Modeler [27]. Δεδομένου ότι το μοντέλο απαιτεί τον υπολογισμό ορισμένων ιδιοτήτων που ποικίλλουν ανάλογα με το χρόνο και την απόσταση, το ACM επιτρέπει τη διεξαγωγή εσωτερικών υπολογισμών χρησιμοποιώντας το Aspen Physical Properties Engine, απλοποιώντας έτσι την διαδικασία επίλυσης. Το θερμοδυναμικό μοντέλο που χρησιμοποιείται είναι η κυβική καταστατική εξίσωση Peng Robinson [28], με μηδενικές δυαδικές παραμέτρους αλληλεπίδρασης. Το μήκος του αγωγού διακριτοποιείται κατά αντιστοιχία με την διακριτοποίηση στο MATLAB και το σύστημα των διαφορικών εξισώσεων, ολοκληρώνεται χρονικά χρησιμοποιώντας είτε τη μέθοδο Implicit Euler είτε τη μέθοδο Runge-Kutta [29].

Για να επαληθευθεί η ορθή ανάπτυξη του μοντέλου ACM, αρχικά, η προσομοίωση διεξάγεται σε μόνιμες και μη μόνιμες συνθήκες για τον εξεταζόμενο αγωγό, με δεδομένες παραμέτρους και τα αποτελέσματα συγκρίνονται. Προκύπτει ταύτιση των αποτελεσμάτων.

Εν συνεχεία, το μοντέλο επεκτείνεται σε εργαλείο αλληλεπίδρασης με τον χρήστη, δίνοντας την δυνατότητα μελέτης του φαινομένου της ρόφησης σε οποιοδήποτε χαλύβδινο αγωγό με οποιαδήποτε σύσταση ΦΑ. Ο χρήστης αρκεί να εισάγει τις συνθήκες εισόδου ρεύματος, τα χαρακτηριστικά του αγωγού και την επιθυμητή τιμή τμημάτων για την διακριτοποίηση του αγωγού. Η προσομοίωση παράγει την καμπύλη συγκέντρωσης του υδραργύρου στην έξοδο του αγωγού συναρτήσει του χρόνου, καθώς και το διάγραμμα κάλυψης της επιφάνειας κατά μήκος του αγωγού, επιτρέποντας στον χρήστη εποπτεία του φαινομένου της ρόφησης σε αληθινό χρόνο.

Η επιτυχής ανάπτυξη του μοντέλου προσρόφησης από το MATLAB στο Aspen Custom Modeler αποτελεί εργαλείο μελέτης της ρόφησης υδραργύρου στην επιφάνεια αγωγών σε εμπορικούς προσομοιωτές. Επιπλέον, δίνει την δυνατότητα εξαγωγής του μοντέλου ως μονάδα στην παλέτα εργαλείων του ASPEN PLUS / Hysys [30] με τις απαραίτητες τροποποιήσεις για προσαρμογή στο περιβάλλον προσομοίωσης.

Εν κατακλείδι, στην παρούσα Διπλωματική Εργασία, αναπτύσσεται επιτυχώς ένα μοντέλο ρόφησης υδραργύρου σε αγωγούς μεταφοράς φυσικού αερίου, το οποίο αποτελεί χρήσιμο εργαλείο για τη βιομηχανία φυσικού αερίου, καθώς μπορεί να εκτιμήσει το χρόνο που απαιτείται μέχρι η συγκέντρωση του υδραργύρου να φθάσει σε κρίσιμα επίπεδα και συνεπώς, να επισημάνει το χρονικό περιθώριο προτού η εγκατάσταση εγκαταστάσεων επεξεργασίας υδραργύρου γίνει επιτακτική για την ασφάλεια του προσωπικού και τη συντήρηση του εξοπλισμού. Το φαινόμενο της ρόφησης μελετάται για εύρος συγκεντρώσεων Hg εισόδου μεταξύ 100 και 5000 ng/Sm³ και για διαφορετικές τιμές της ειδικής επιφάνειας χαλύβδινου αγωγού. Για τα διαφορετικά αυτά σενάρια, υπολογίζεται ο χρόνος που απαιτείται για την υπέρβαση του ορίου προδιαγραφών συγκέντρωσης υδραργύρου (10 ng/Sm³), στην έξοδο του αγωγού, και αναπαράγονται τα χρονικά εξαρτώμενα προφίλ συγκέντρωσης υδραργύρου στην έξοδο του αγωγού και κορεσμού της επιφάνειας. Συμπεραίνεται ότι μια αύξηση στη συγκέντρωση εισόδου υδραργύρου μειώνει τον χρόνο που απαιτείται για να φθάσει η συγκέντρωση την κρίσιμη τιμή, ενώ αύξηση της ικανότητας προσρόφησης του σωλήνα αυξάνει τον χρόνο εμφάνισης του υδραργύρου, όπως αναμένεται από το θεωρητικό υπόβαθρο της προσρόφησης. Η παραμετρική ανάλυση αποκαλύπτει την ευαισθησία του μοντέλου στον συντελεστή μεταφοράς μάζας και τον συντελεστή συμπίεστικότητας, ενώ ρίχνει φως στην επιλογή των κατάλληλων κινητικών παραμέτρων. Επιπρόσθετα, η ενσωμάτωση του μοντέλου στο λογισμικό Aspen Custom Modeler αποτελεί εργαλείο προσομοίωσης της ρόφησης υδραργύρου σε αγωγούς μεταφοράς φυσικού αερίου, προάγοντας την αλληλεπίδραση με το χρήστη σε ένα ιδιαίτερος απλό στη χρήση περιβάλλον, και διευρύνοντας, τοιουτοτρόπως, το κοινό χρηστών που απευθύνεται.

Τα παραπάνω οδηγούν σε ορισμένες προτάσεις για μελλοντική μελέτη. Έτσι, κρίνεται απαραίτητο να διερευνηθούν περαιτέρω οι κινητικές παράμετροι της προσρόφησης και εκρόφησης του υδραργύρου σε χαλύβδινες επιφάνειες αγωγών μεταφοράς ΦΑ καθώς και να προσδιορισθούν πειραματικά μεγέθη, όπως η ειδική επιφάνεια του αγωγού (*SSA*). Δεδομένου ότι το μοντέλο επικεντρώνεται στην μονοστρωματική φυσική προσρόφηση του υδραργύρου στον χάλυβα, πρέπει να επεκταθεί προκειμένου να συμπεριλάβει όλους τους πιθανούς μηχανισμούς συσσώρευσης. Ένα πρώτο βήμα είναι η ενσωμάτωση των χημικών αντιδράσεων του υδραργύρου με συστατικά του ΦΑ, όπως το υδρόθειο (H_2S), προς σχηματισμό θειούχου υδράργυρου (HgS), ο οποίος μπορεί να προσροφηθεί στα τοιχώματα, καθώς και αλληλεπίδραση του υδραργύρου με αποθέσεις της επιφάνειας. Η διερεύνηση των δυνατοτήτων πειραματικής επαλήθευσης των αποτελεσμάτων και η αντίστοιχη προσαρμογή των παραμέτρων σε πειραματικές δεδομένα, αποτελούν επιτακτική ανάγκη για την ανάπτυξη ενός λιγότερο συντηρητικού μοντέλου.

ΛΕΞΕΙΣ ΚΛΕΙΔΙΑ: υδράργυρος, φυσικό αέριο, προσρόφηση, χαλύβδινοι αγωγοί, προσομοίωση

ABSTRACT

Mercury (Hg) and its compounds are inherently traceable in fossil fuels, including natural gas, crude oil and coal. When reservoirs are exploited, elemental mercury and the other forms that may be present in the reservoir, partition to separated phases (oil, gas and water) and travel throughout production and processing systems. Even if present in minor concentration (a few ppb), different forms of mercury can provoke severe implications during gas and oil processing.

Besides its toxic nature, mercury might be responsible for catalyst deactivation and it is highly corrosive when interacting with materials of processing equipment, as it amalgamates. In the past, the detrimental interactions of mercury with downstream aluminum heat exchangers, such as those used in cryogenic hydrocarbon recovery natural gas plants and in natural gas liquefaction plants, have been reported to result in major industrial accidents, due to mechanical failure and gas leakage.

Mercury, as a trace component of natural gas, can be transported through pipelines, from the well to the reception facility. However, mercury is detected in the inlet facilities after an extended period of operating time, due to its slow accumulation, via adsorption mechanisms, inside the flowlines. This is known as “mercury lag effect”. Once the pipe walls become saturated, mercury will “breakthrough”. The time, prior to mercury concentration reaching a critical point which ordains the installation of mercury treatment units, is called time to breakthrough.

Although the interaction of mercury with steel and stainless steel is known, there is a lack of extensive research on the primary mechanisms of mercury uptake in pipelines and on the conditions which favour the adsorption and desorption kinetics. Considerable scientific work is currently under way. Aside from the above-mentioned difficulties, the confidential character of the gas and oil industry impedes the publication of valid field and experimental data.

The scope of this Diploma Thesis is the development of a model for mercury adsorption/desorption in natural gas transport pipelines, able to estimate the time taken for mercury breakthrough based on first principles. Moreover, it provides the time-dependent adsorption profiles of mercury for several inlet concentrations (100-5000 ng/Sm³) and pipe’s adsorption capacities (0.0038-10 g/m²). The model was built and run in MATLAB.

To this end, a literature review was conducted regarding possible methods of mercury accumulation onto metal surfaces and already existing adsorption models. Hereupon, the variables of the model are defined, the main assumptions are stated, and the mathematical formulation permits a rigorous description of mercury physical adsorption, limited to the formation of a monolayer. The reverse process of desorption is, also, studied. Since segmentation is a popular approach to fluid dynamics, the examined pipeline was effectively discretised to ensure model results’ accuracy and reduce the computational intensity associated with solving the model. Using the thermodynamic model UMR-PRU, which has been successfully applied to natural gas mixtures, physical properties, such as gas density and mercury fugacity coefficient, were calculated, and the rest of the parameters were defined by appropriate methods. Furthermore, the effect of main model assumptions and parameters, on mercury adsorption profile and breakthrough time, was investigated.

Afterwards, the model was developed in Aspen Plus Custom Modeler. Initially, the simulation was run in dynamic and steady state mode, to validate MATLAB model results, with fixed parameters. At a later stage, it was extended to serve a user-interactive environment, enabling the study of the adsorption phenomenon in any pipeline, provided that the user defines of stream inlet conditions and pipe characteristics.

The simulation produces the mercury concentration profile at the exit of the pipeline over time, as well as the adsorption front along the pipe, allowing the user to closely

observe the adsorption phenomenon in real time. The successful implementation of the mercury adsorption model from MATLAB Aspen Custom Modeler, renders it an easy-to-use pipeline simulation tool. It shall not be neglected that the ACM mercury adsorption model holds, also, great potential to be integrated, with minor modifications, into the Aspen Plus/Hysys units' palette.

This work presents a model for estimating the time for mercury breakthrough in natural gas transport pipelines, based on the simplified approach of mercury accumulation due to physical adsorption onto the steel surface of the pipe wall. A systematic and thorough approach is attempted regarding the calculation of the model parameters, and a sensitivity analysis is employed to examine the effect of parameters' uncertainty. The model reveals that an increase in the mercury inlet concentration decreases breakthrough time at the reception facilities, whereas increasing adsorption capacity of the pipe increases the time for mercury breakthrough, as it is expected by the theoretical background of adsorption process. An empirical equation for the prediction of the breakthrough time as a function of the mercury concentration in the pipeline inlet and the pipeline adsorption capacity, expressed in Specific Surface area terms, has been developed. The parametric analysis reports the sensitivity of the model to the mass transfer coefficient, which participates in the mercury mass transfer term to the pipe walls and vice-versa, the compressibility factor of the gas, as well as parameters related to desorption kinetics, such as the activation energy and pre-exponential factor.

The model of mercury adsorption is a useful tool for the natural gas industry, as it points out the time limit before the installation of mercury treatment facilities becomes imperative for personnel safety and equipment maintenance. For this reason, its implementation in Aspen Custom Modeler allows its use by a broader audience.

KEY WORDS: mercury, natural gas, adsorption, steel pipelines, breakthrough, simulation

Contents

ACKNOWLEDGMENTS.....	i
ΠΕΡΙΛΗΨΗ.....	ii
ABSTRACT.....	xii
FIGURES, TABLES & ILLUSTRATIONS.....	v
Figures.....	v
Tables.....	vi
Illustrations.....	vi
NOMENCLATURE.....	vii
Greek Symbols.....	viii
Subscripts.....	viii
Superscripts.....	viii
1. INTRODUCTION.....	1
2. BACKGROUND.....	3
2.1. Physical adsorption and Chemisorption.....	3
2.2. Adsorption Isotherms.....	4
2.3. Adsorption Kinetics.....	5
2.4. Desorption Kinetics.....	6
3. ADSORPTION OF MERCURY ONTO MONOCRYSTALLINE AND POLYCRYSTALLINE SURFACES.....	7
3.1. Adsorption to Au(111) and Ag(111).....	7
3.2. Adsorption to Cu(100) and Polycrystalline Copper Surfaces.....	8
3.3. Adsorption to Zn(0001) and Polycrystalline Zinc Surfaces.....	9
3.4. Adsorption to Fe(100) and Polycrystalline Iron Surfaces.....	9
3.5. Mercury Adsorption in Operational Gas Pipelines.....	11
4. MODELLING OF ADSORPTION AND ADSORPTION-RELATED PARAMETER IDENTIFICATION.....	12
4.1. Modelling of Adsorption in Pipelines.....	12
4.2. Activation Energy of Desorption and Pre-exponential Factor.....	13
4.3. Adsorption Capacity and SSA.....	14
4.4. UMR-PRU Model.....	15
5. MODEL DESCRIPTION.....	16
5.1. Model description, assumptions and simplifications.....	16
5.2. Mass Transfer in the Bulk Gas.....	17
5.3. Mass Transfer in the Stagnant Boundary Layer.....	17
5.4. Adsorption Kinetics on Iron Surfaces.....	17
5.5. Desorption Kinetics on Iron Surfaces.....	18
6. MODEL IMPLEMENTATION.....	19
6.1. Fixed Parameters.....	19
6.2. Model Solving.....	19
6.3. Initial Conditions and Specification Limits.....	20
7. MODEL COMPONENTS AND PARAMETERS.....	21
7.1. Segmentation.....	21

7.2.	Investigation of Flow's Compressibility.....	22
7.3.	Pressure Drop	23
7.4.	Mass Transfer Coefficient.....	23
7.5.	Stagnant Boundary Layer in a Discrete Section.....	23
7.6.	Other properties	24
7.7.	Diffusivity.....	24
7.8.	Viscosity.....	25
7.9.	Calculation of Activation Energy of Desorption and Pre-exponential Factor.....	26
7.10.	Adsorption Capacity and Specific Surface Area of the Pipe	28
8.	RESULTS & DISCUSSION	29
8.1.	Results.....	29
8.2.	Sensitivity Analysis.....	34
8.2.1.	Effect of Mass Transfer Coefficient.....	36
8.2.2.	Effect of Compressibility Factor.....	37
8.2.3.	Effect of Fugacity Coefficient.....	38
8.2.4.	Effect of the Stagnant Boundary Layer Thickness.....	38
8.2.5.	Confirmation of the Compensation Effect.....	40
8.2.6.	Curve Fitting for the Activation Energy of Desorption and Surface Coverage.....	44
9.	MODEL IMPLEMENTATION IN ASPEN CUSTOM MODELER.....	46
9.1.	Aspen Custom Modeler	46
9.2.	ACM Model Development.....	46
9.3.	Validation of MATLAB Model Results	49
9.4.	ACM Model Testing.....	51
10.	CONCLUSIONS AND RECOMMENDATION	54
10.1.	Conclusions	54
10.2.	Recommendations.....	55
	REFERENCES	56
	APPENDIX	60
	MATLAB Model Values.....	60
	ACM Model Values for Trial Case.....	60

FIGURES, TABLES & ILLUSTRATIONS

Figures

Figure 7-1: The effect of segmentation on the accuracy of model's solution (breakthrough time).....	21
Figure 7-2: CPU time vs number of segments.....	22
Figure 7-3: Equilibrium adsorption isotherms for Hg on Fe(100) at various temperatures [16].	26
Figure 7-4: Activation energy of desorption vs surface coverage with varying pairs of v and E_0	28
Figure 8-1: Mercury outlet concentration vs time for Case 1-0.....	30
Figure 8-2: Mercury outlet concentration vs time for Case 1-1.	30
Figure 8-3: Mercury outlet concentration vs time for Case 3-0.	31
Figure 8-4: Mercury outlet concentration vs time for Case 3-1.	31
Figure 8-5: Mercury outlet concentration vs time for Case 2-1.	32
Figure 8-6: Length of Mercury Adsorption Front for Case 2-1.....	32
Figure 8-7: Length of Mercury Adsorption Front for Case 2-2.....	33
Figure 8-8: Breakthrough time estimated by the model vs the corresponding time estimated by Equation 8-1.....	33
Figure 8-9: Length of mercury adsorption front for Case 2-2.....	34
Figure 8-10: Derivates of bulk gas mercury concentration for the first segment dependent on the model parameters k_m , Z and $\varphi^{v_{Hg}}$ for Case 1-0.....	35
Figure 8-11 Derivates of surface coverage for the last segment dependent on the model parameters k_m , Z and $\varphi^{v_{Hg}}$ for Case 1-0.	35
Figure 8-12: Effect of mass transfer coefficient on breakthrough time for Case 1-0.	36
Figure 8-13: Effect of mass transfer coefficient on mercury adsorption front for Case 1-0 at breakthrough.....	36
Figure 8-14: The effect of compressibility factor on surface coverage at breakthrough for Case 1-0.....	37
Figure 8-15: Adsorption front at 110 days for varying fugacity coefficient, $\varphi^{v_{Hg}}$, for Case 1-2.	38
Figure 8-16: Adsorption front for varying stagnant boundary layer thickness, at breakthrough, for Case 1-0.....	39
Figure 8-17: Relation between activation energy for adsorption at zero coverage and pre-exponential factor, v	40
Figure 8-18: Adsorption front length at breakthrough for Case 2-1 for different pairs of E_0 - v	41
Figure 8-19: Adsorption front length at breakthrough for Case 3-1 for different pairs of E_0 - v	41
Figure 8-20: Comparison of adsorption length at breakthrough for Cases 1-1, 2-1 and 3-1 with $E_0=151$ kJ/mol and 302 kJ/mol.....	42
Figure 8-21: Adsorption length at breakthrough for Cases 1-1, 2-1 and 3-1 with $E_0=75.5$ kJ/mol.....	42
Figure 8-22: Effect of varying pre-exponential factor on maximum surface coverage for Case 1-1.....	43
Figure 8-23: Effect of varying pre-exponential factor on breakthrough time for Case 1-1.	43
Figure 8-24: Best fit for activation energy of desorption vs surface coverage.	44

Figure 8-25: Comparison of adsorption profile for 2 nd order polynomial and linear function of $E_{a,des}-\theta$ for Cases 1-1, 2-1 and 3-1 at breakthrough.	45
Figure 9-1: Adsorption front for Case 1-0 at the start of the phenomenon (3.43 hours), as produced in ACM.....	50
Figure 9-2: Adsorption front for Case 1-0 at 20 hours, as produced in ACM.....	50
Figure 9-3: Comparison of adsorption front length at breakthrough, as produced in MATLAB and ACM.	51
Figure 9-4: Adsorption front for Trial Case after breakthrough.....	51
Figure 9-5: Mercury outlet concentration at steady state conditions.	52

Tables

Table 3-1: Results of mercury layer thickness on polycrystalline copper surfaces.....	8
Table 3-2: Results of mercury layer thickness on polycrystalline zinc surfaces.....	9
Table 3-3: Results of mercury layer thickness on polycrystalline iron surfaces.....	10
Table 7-1: Deviations in breakthrough time due to segmentation (Mercury Inlet concentration: 5000 ng/Sm ³ and SSA=1).....	21
Table 7-2: Calculation of the Mach number.....	22
Table 7-3: Parameters used for the calculation of diffusion coefficient.	25
Table 7-4: Variation of E_0 with v using the quasi-chemical approach [16].	26
Table 7-5: Variation of surface coverage with pressure at 322.5 K [16].....	27
Table 7-6: Rate of adsorption for varying values of surface coverage, equal to the rate of desorption at equilibrium.	27
Table 7-7: Activation energy of desorption as a function of surface coverage and pre-exponential factor.....	27
Table 8-1: Pipeline adsorption model results.....	29
Table 8-2: The effect of compressibility factor on breakthrough time for varying Z.	37
Table 8-3: The effect of varying Z on the steepness of adsorption front at breakthrough time.....	38
Table 8-4: Tested alues of stagnant boundary layer thickness.	39
Table 8-5: Compensation effect vs time to breakthrough for Cases 2-1 & 3-1.	41
Table 8-6: Effect of E_0 on time to breakthrough.....	43
Table 8-7: Effect of best fit curve of $E_{a,des}-\theta$ on breakthrough time and comparison with the linear function used in the model.....	44

Illustrations

Illustration 5-1: Pipeline segmentation.....	16
Illustration 5-2: Illustration of the radial direction of the pipe.....	16
Illustration 9-1: The ACM mercury adsorption model flowsheet.....	47
Illustration 9-2: Pipeline icon in ACM.	47
Illustration 9-3: User-defined pipe characteristics and segmentation.....	48
Illustration 9-4: User-defined feed inlet conditions.....	48
Illustration 9-5: Outlet stream conditions in simulation time.	49

NOMENCLATURE

Symbol	Description
A	Area
A_{constant}	Cubic EoS Specific Constant
ACM	Aspen Custom Modeler
B	Adsorbate
b	Co-volume parameter of cubic EoS
C	Concentration
c	constant
D	Diffusivity
d	constant
d_{pipe}	Pipe diameter
E_{α}	Activation energy
E_0	Activation energy of desorption at zero coverage
$G_{AC}^{E,SG}$	Staverman-Guggenheim term of excess Gibbs free energy from Activity Coefficient Model
$G_{AC}^{E,res}$	Residual term of excess Gibbs free energy from Activity Coefficient model
F_{vol}	Volumetric flowrate
f_D	Darcy friction factor
K	Equilibrium constant
k	Boltzmann constant
k_{ads}	Adsorption rate constant
k_{des}	Desorption rate constant
k_m	Mass transfer coefficient
L	Pipe length
M_{α}	Mach number
M_w	Molecular weight
ML	Monolayer
N	Number of particles per unit surface area
N_A	Avogadro's number
N_{max}	Maximum number of particles per unit surface area
n	Number of discrete section
P	Pressure
p	Adsorbed concentration
p^*	Partial pressure
Q_{max}	Maximum surface coverage
R	Universal gas constant
RT	Room temperature
LT	Low temperature
RD	Relative Difference
Rate	Rate
Re	Reynolds number
S	Vacant adsorption site on adsorbent
S_{max}	Maximum surface concentration
SB	Adsorbed Phase
Sc	Schmidt number
Sh	Sherwood number
s	Sticking probability
s_0	Initial sticking probability
Species	Species
SSA	Specific surface area

T	Temperature
t	Time
u	Velocity
V	Volume
W	Areal Concentration
w	Speed of sound
x	Length of discrete section
Z	Compressibility factor
z	Molar fraction

Greek Symbols

Symbol	Description
α	Parameter of cubic EoS accounting for dispersion forces
δ	Stagnant boundary layer thickness
δ_c	Concentration boundary layer thickness
ϵ/k	Parameter of the Lennard Jones potential
ζ	Reaction order
θ	Surface coverage
μ	Viscosity
ν	Pre-exponential factor, desorption
π	Pi
ρ	Density of the vapour-gas mixture
σ	Molecular radius for hard-sphere
φ	Fugacity coefficient
Ω	Collision integral for the Lennard-Jones potential

Subscripts

Symbol	Description
A	Component A
ads	Adsorption
B	Component B
bulk	Bulk mixture
des	Desorption
Fe	Iron
gas	Gas mixture
Hg	Mercury
i	Component i
in	Inlet
j	Component j
out	Outlet
pipe	Pipe
stagnant	Stagnant Boundary Layer
total	Total of all components

Superscripts

Symbol	Description
V	Vapour
std	Standard conditions

1. INTRODUCTION

Crude oil and natural gas originate from geological formations associated with ancient basins, where organic material was chemically transformed to molecular hydrocarbons, under conducive conditions of pressure and temperature [2]. Mercury occurs naturally in soil and rock throughout the earth's crust, including the formations that comprise oil and gas reservoirs. There is still scientific uncertainty, regarding the origin of mercury in deposits, with the most prevailing hypothesis associated with the liberation of mercury by geological forces from the mantle, and its mitigation as a vapour to the traps in which oil and gas accumulate [1].

The concentration of mercury in crude oil and natural gas varies significantly, based on their geological origin. Some varieties of crude oil, processed in the USA, are estimated to contain from 1 to 1000 ppb Hg (wt), with the mean close to 5 ppb [2]. In natural gas and natural gas condensates, mercury concentrations typically range from 1 to 200 micrograms per standard cubic meter ($\mu\text{g}/\text{Scm}$) [1]. The world's average for elemental mercury in gas is not known with statistical certainty but it is thought to be less than 10 $\mu\text{g}/\text{Scm}$ [4]. The amount of mercury in the reservoirs is rising, on one hand, due to depletion of the reservoirs and on the other hand, due to the need for exploiting smaller and deeper deposits.

A concrete approach towards categorisation of mercury species is of paramount importance to develop successful methods for mercury management. In natural gas, mercury exists almost exclusively in its elemental form (Hg^0) and at concentrations far below saturation, indicative of the absence of liquid mercury phase in most reservoirs [3]. The prevalence of dialkylmercury, in the form of methylmercury (CH_3HgCl) and dimethylmercury ($\text{CH}_3)_2\text{Hg}$, is largely unknown but is speculated to appear in traces (<1% THg), based on the limited speciation data reported in the literature for gas condensates. In natural gas condensates, the dominant mercury species is the elemental mercury (>50% του THg), followed by smaller percentages of several other mercury compounds, such as suspended HgS and diluted HgCl_2 (10-50% του THg) [2].

The existence of elemental mercury in natural gas is highly correlated with natural gas processing plant failures. The implications of mercury in natural gas were first reported in 1973, when a catastrophic failure of aluminum heat exchangers, operating at cryogenic conditions, occurred at Skikda liquefied natural gas plant, in Algeria [5]. The investigation pointed out that the failure was caused by mercury corrosion. After the failure in Skikda, a study on Groningen fields in the Netherlands revealed similar corrosion in the gas gathering system, with mercury concentrations ranging from 0.001 to as high as 180 $\mu\text{g}/\text{Nm}^3$ [3]. The latest reported case of mercury-related accident in the gas industry, is that of Moomba Gas Processing Plant, in 2004. The failure of an inlet nozzle, due to liquid metal embrittlement (LME) by elemental mercury, in the cryogenic heat exchanger, was the cause of gas release, which led to fire and explosion at the LRP section [6]. To date, approximately 10 reported industrial incidents [7], which are connected with corrosion due to mercury, reveal that, although mercury in natural gas is found in traces, failure to remove it from produced gas streams carries significant liability, if gathering, pipeline, and downstream processing facilities become contaminated.

Due to its cumulative effect, the appearance of elemental mercury at processing facilities can be delayed by months or years, as steel pipelines act as scavengers of mercury. However, over time, the mercury concentration measured at the plant inlet will rise to close to the wellhead level [1]. This is known as "mercury lag effect" [8].

The reaction and incorporation of mercury into steel surfaces and its lag effect call for stringent safety precautions, regarding operation and equipment maintenance, as the emission of elemental mercury vapor to the work environment is toxic to workers. Moreover, apart from mercury accumulation within pipelines, cryogenic processing

plants are subject to increased risks from processing natural gas with trace components of mercury [31]. When condensed, elemental mercury forms an amalgam with the surface layer of the metal it contacts (Al, Cu, Zn, Ni etc), thus causing equipment corrosion. Corrosion is provoked either by Liquid Metal Embrittlement (LME), when certain ductile metals experience drastic loss in tensile ductility or undergo brittle fracture or, as in the case of aluminum, the amalgam reacts with water to form metal oxide and free Hg, resulting in Amalgam Corrosion (AMC) on surfaces of Aluminum Heat Exchangers (AHX) [9]. The latter leads to immediate and catastrophic pressure loss. Mercury has also been found to be a serious poison to metal catalysts used in the hydrocarbon processing.

To avoid the aforementioned risks, operators of LNG and conventional gas processing plants seek the total removal of mercury from natural gas and NGL plants, via the installation of removal systems [3]. However, despite the advancement in understanding of mechanisms and availability of systems to prevent contamination, the availability of experimental data on the kinetics and mechanisms of mercury adsorption on steel pipe walls is limited. This fact, in combination with the confidential policy of the oil and gas industry, regarding data publication on mercury concentration, render the development of a predictive mercury adsorption model challenging.

Taking the above into consideration, the scope of the present diploma thesis is the development of a mercury adsorption model in natural gas pipelines. The model estimates the time interval between mercury introduction to the pipeline and its appearance at critical concentrations at the entrance of the reception facility, which is called "time to breakthrough". Moreover, it provides the time-dependent adsorption profiles of mercury for several inlet concentrations and pipe wall's adsorption capacities.

In the first step, a literature review is conducted regarding possible methods of mercury accumulation onto metal surfaces and already existing adsorption models. Hereupon, the variables of the model are defined, and the mathematical formulation permits a rigorous description of the physical phenomenon. The model is developed in MATLAB [10]. Using the thermodynamic model UMR-PRU [25], which has been successfully applied to natural gas mixtures [32], the fugacity coefficient of mercury and the compressibility factor of the gas mixture are calculated, and the rest of the parameters are defined by appropriate methods. Furthermore, the effect of the mass transfer coefficient, compressibility factor, mercury fugacity coefficient, stagnant boundary layer thickness and kinetic-related parameters, such as the pre-exponential factor and activation energy of desorption on the model results is investigated.

Finally, the model is developed in Aspen Custom Modeler and it is extended to respond to the needs of gas industry stakeholders for real-time results of mercury at the outlet of the pipeline. The model is built to accept user-defined inlet gas conditions, as well as pipe characteristics, demonstrating great potential for integration in an ASPEN PLUS/Hysys flowsheet.

2. BACKGROUND

2.1. Physical adsorption and Chemisorption

Adsorption is a surface phenomenon that occurs when a gas or liquid solute (adsorbate) accumulates on the surface of a solid or liquid condensed phase (adsorbent), forming a molecular or atomic film [11]. An unbalanced force of attraction on the surface of the adsorbent is generally responsible for the adsorption to occur [33]. Being a way to approach equilibrium, adsorption is a spontaneous process, usually exothermic in nature [34]. Desorption describes the reverse process, this being the release of molecules from the adsorbent to the surrounding phase. In the context of this study, the gas-solid interaction is further examined.

Depending on the nature of the intermolecular forces between the adsorbent and the adsorbate, adsorption on solid surfaces may be divided into two categories: physical adsorption (physisorption) and chemical adsorption (chemisorption). Occasionally, it may be complicated to identify what type of adsorption is predominant, as it is possible that a combination of both occurs [12].

Physical adsorption is non-specific, rapid and highly reversible. Physisorbed molecules have low bonding energies, in the range of 0.5-10 kJ/mol, in comparison to average bond energies of atoms that are calculated higher than 96 kJ/mol [35], and large equilibrium distances, 0.3 – 1.0 nm [36]. The weak bonding is attributed to dipole interactions or van der Waals forces, which do not provoke any significant change in the orbital patterns [37]. The forces responsible for physisorption are essentially the same as those responsible for the condensation of a vapour to the liquid state [34]. Given the weak interaction, physisorption generally occurs at low temperatures, with low values of heat evolved (2-25 kJ/mol) and activation energy ranging between 21-42 kJ/mol. Equilibrium between the solid surface and the gas molecules is usually attained rapidly and it is reversible due to the low energy requirements. Multiple layers of adsorbed molecules are possible, especially near the condensation temperature [38].

Unlike physisorption, chemisorption is specific and often irreversible. Chemisorbed molecules form chemical bonds of high energy, in the order of 96 kJ/mol or higher, with the substrate, and the reaction is exothermic and measurable through calorimetric methods [39]. Chemisorption may cause the rearrangement of the electronic structure of the solid, and therefore adsorbed molecules may dissociate, forming new reaction products. Since the process involves chemical bond formation, the amount of heat evolved in chemisorption is large (e.g. 50–500 kJ/mol) [38]. Chemisorption usually occurs at elevated temperatures, where activation energy varies between 42-419 kJ/mol [12]. Since the adsorbed molecules are linked to the surface by valence bonds, they usually occupy certain adsorption sites on the surface, hence, the surface coverage is limited to a monolayer [38].

Prior to proceeding further, it is of paramount importance to clarify frequently used terms in adsorption theory, which will emerge throughout the analysis. A monolayer (ML) is defined as the maximum attainable concentration of adsorbed particles on the surface of the substrate (with a typical surface density value of about 10^{15} atoms per cm^2). According to Lüth [40] one monolayer of molecules is formed per second at a pressure of $\sim 1.3 \cdot 10^{-4}$ Pa, provided that bonding occurs. Surface atoms react with one gas molecule per second at this pressure and the amount of gas is expressed in Langmuir (L). References to dosing, in the present Diploma Thesis, are expressed in L.

2.2. Adsorption Isotherms

Taking into consideration that both adsorption and desorption are dynamic processes, at equilibrium the rates of adsorption and desorption are equated, and the surface coverage of adsorbed atoms is constant. The equilibrium state is a function of partial pressure of the adsorptive species in the gas phase and the system temperature. In general terms:

- a) Increasing the adsorptive partial pressure increases surface coverage up to the point where the surface becomes saturated.
- b) Increasing temperature reduces surface coverage.

These trends are described through adsorption isotherms, which can be used as tools for understanding the mechanism of adsorption and for quantitative assessment of partition or distribution of the adsorbate at equilibrium between the adsorbent and the fluid phase at a given temperature [41]. In the case of adsorbed gases, through adsorption isotherms, the correlation of the amount of adsorbate on the adsorbent with its pressure is extracted. Considering the definition of the adsorption capacity (or loading) as the amount of adsorbate taken up by the adsorbent per unit mass (or volume) of the adsorbent [42], it is evident that the adsorption capacity may be determined by the use of adsorption isotherms.

In isotherm modelling, the concentration of the adsorbate on the adsorbent is expressed as a function of the adsorbate concentration still in solution after equilibrium has been reached.



In Eq. 2-2, S represents a surface site on the adsorbent, B represents the adsorbate, SB represents the adsorbed phase, k_{ads} is the forward (adsorption) rate constant, and k_{des} is the backward (desorption) rate constant.

With the equilibrium constant, K , of the adsorption reaction being given by:

$$K = \frac{k_{ads}}{k_{des}} \quad \text{Eq. 2-2}$$

Several isotherm models are available in the literature that describe experimental data of adsorption isotherms [43, 44]. The most frequently reported is the Langmuir model, which is further analysed. Established in 1918, the Langmuir model is based on the following main assumptions [34, 45]:

- a) The gas is considered ideal.
- b) The surface is characterized by a finite number of identical sites. Each active site interacts with only one adsorbate molecule (localized adsorption).
- c) The adsorption sites are all energetically equivalent (homogeneous surface).
- d) The binding energy of each molecule is independent of the presence or absence of adsorbates on neighboring sites (the energy of adsorption is independent of surface coverage).
- e) Adsorption is exhausted after the formation of the first layer. Hence, it is limited to a monolayer.

Langmuir adsorption isotherm further assumes that the fractional surface coverage θ is in direct proportion to the rate of desorption from the surface, and the adsorption and desorption rates are equal at equilibrium. Those assumptions lead to the more familiar

“Langmuir expression” for fractional site occupation as a function of partial pressure [45], as described in Eq. 2-3.

$$\theta = \frac{K \cdot p^*}{1 + K \cdot p^*} \quad \text{Eq. 2-3}$$

where, θ is the surface coverage, p^* is the partial gas pressure of the adsorbate.

In the present study, adsorption isotherm data of Jones and Perry [16] are used as tool for the calculation of activation energy of desorption as described in Section 7.9.

2.3. Adsorption Kinetics

As in any chemical reaction, surface processes involve breaking and making of bonds. For surface kinetics, the rate of adsorption is similarly expressed to the rate of a chemical reaction (Eq. 2-5), however two-dimensional concentration, related to surface area, must be considered [46].



$$\text{Rate} = -\frac{dN_B}{dt} = +\frac{dN_{SB}}{dt} \text{ in } \left[\frac{\text{particles}}{\text{unit area} \cdot \text{s}} \right] \quad \text{Eq. 2-5}$$

In the case of an initially bare surface exposed to a certain gas pressure, the rate of collision of the gas particles with the unit surface is given by kinetic theory [46]:

$$\frac{dN}{dt} = \frac{p^* N_A}{\sqrt{2\pi M_w RT}} \quad \text{Eq. 2-6}$$

where, N is the number of particles per unit surface area, p^* is the partial pressure of the gas, N_A is the Avogadro’s number, M_w the molecular weight, R the universal gas constant and T the temperature.

Multiplied by a sticking probability factor, s , which is a function of the surface coverage θ , Eq. 2-6 shall be re-written as

$$\frac{dN}{dt} = \frac{p^* N_A}{\sqrt{2\pi M_w RT}} \cdot s \quad \text{Eq. 2-7}$$

The sticking probability reflects whether the impinging particle stays on the surface or it is reflected. As the surface is gradually covered, s decreases – simply because the number of empty adsorption sites gets smaller. The sticking probability is also dependent upon the initial sticking probability s_0 and the order of adsorption, ζ . It varies between 0 and 1.

$$\frac{dN}{dt} = \frac{p^* N_A}{\sqrt{2\pi M_w RT}} \cdot s_0 (1 - \theta)^\zeta \quad \text{Eq. 2-8}$$

If an adsorbed particle statistically occupies a single site, the adsorption is 1st order. If it dissociates, two sites are blocked by one collision event, and the adsorption can be characterized as 2nd order adsorption.

The surface coverage, θ , can be expressed as in Eq. 2-9.

$$\theta = \frac{N}{N_{max}} \quad \text{Eq. 2-9}$$

where, N_{max} is the maximum number of adsorption sites.

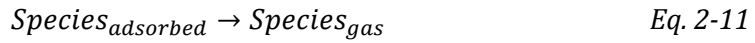
In case the adsorption requires a certain activation energy only particles having this energy will be able to stick. It is generally only second order adsorption processes which have an adsorption activation energy, due to the dissociation of the molecule. Therefore, Eq. 2-10 shall be expressed in terms of surface coverage to calculate the actual coverage after a certain time of gas exposure, simply by integrating the rate equation.

$$Rate_{ads} = \frac{d\theta}{dt} = \frac{p^* N_A}{\sqrt{2\pi M v R T}} \cdot \frac{s_0 (1-\theta)^\zeta}{N_{max}} \cdot \exp\left(-\frac{E_{a,ads}}{RT}\right) \quad Eq. 2-10$$

where, $E_{a,ads}$ is the activation energy for adsorption.

2.4. Desorption Kinetics

The desorption is understood as a normal chemical reaction, thereby it is described by the respective kinetic formalism [46].



with rate constant, k_{des} .

It is stressed that only thermal desorption will be taken into consideration in the mathematical formulation of desorption kinetics. The rate of desorption for an unknown reaction order, ζ , is written as

$$\frac{dN}{dt} = -k_{des} N^\zeta \quad Eq. 2-12$$

Upon introducing the surface coverage and expressing k_{des} in Arrhenius terms, Eq. 2-13 takes the form of the Polanyi-Wigner equation [47].

$$Rate_{des} = \frac{d\theta}{dt} = -\nu \theta^\zeta N_{max}^{\zeta-1} \exp\left(\frac{-E_{a,des}}{RT}\right) \quad Eq. 2-13$$

where, ν is the pre-exponential factor and $E_{a,des}$ the activation energy of desorption.

3. ADSORPTION OF MERCURY ONTO MONOCRYSTALLINE AND POLYCRYSTALLINE SURFACES

The significant impact of contamination and corrosion of gas transportation and processing equipment, caused by the presence of mercury in traces, has sparked scientific interest in the mechanism of mercury adsorption and desorption onto various types of metallic surfaces. The majority of findings is centred upon adsorption on monocrystalline materials, while the study of adsorption kinetics of mercury on polycrystalline materials appears to be limited.

Such work reported in the literature includes mercury adsorption onto gold and silver monocrystals [13] and both monocrystalline and polycrystalline surfaces of copper [14, 15], zinc [14, 15], and iron [14, 16, 17], is presented.

Research on mercury adsorption on the aforementioned polycrystalline metal surfaces bears similar experimental conditions. In particular, for the polycrystalline copper, zinc and iron surfaces, Roseborough et al. [14, 16, 17], experiments were performed in vacuum, using Thermal Desorption Auger Electron Spectroscopy (TDAES) to evaluate samples at both room temperature (RT) of 298 K and low temperature (LT) ranging from 82-111K.

The dependence of mercury adsorption on temperature and the thickness of mercury saturation layer, as calculated by the photoelectron mean free path [40], were determined [14, 17]. Desorption temperatures were monitored in the range of 85 to 298 K to calculate desorption energies. Clean surfaces were, also, pretreated with varying doses of chlorine and oxygen to investigate the effect of "contamination" on the adsorption mechanism and mercury bonding, within the same temperature interval

The reasons behind opting to study the effect of chlorine and oxygen pretreatment on mercury adsorption lie upon the abundance of the two elements in nature and their role as co-adsorbates with mercury on metal surfaces [14, 17]. Firstly, chlorine contamination is known to originate in various sources, due to saltwater and water purified with chlorine. This contamination can lead to chlorine deposition in quantifiable amounts on metal surfaces, such as zinc or iron, when exposed to the atmosphere. Oxygen naturally coats surfaces and it is frequently present on iron surfaces [14, 17].

3.1. Adsorption to Au(111) and Ag(111)

Silver and gold films are used for preconcentration of Hg for analysis of trace amounts of gaseous mercury in ambient air or even in flue gases [48]. It has been theoretically estimated that the amount of mercury needed to form a continuous monolayer on a gold surface is $0.36 \mu\text{g}/\text{cm}^2$. Experimentally determined values for the collection capacity of a gold surface vary from $0.0117 \mu\text{g}/\text{cm}^2$ to $0.7 \mu\text{g}/\text{cm}^2$ [49]. Levlin et al [13] examined the adsorption of gaseous elemental mercury with varying concentrations (30, 130 and 320 ng/L) onto nearly single-crystalline surfaces of gold and silver at different substrate temperatures (22, 60, 90 °C) and exposure times (15-360 min). The data obtained were evaluated using the technique of Scanning Tunneling Microscopy (STM). Exposed surfaces revealed that the saturation level varies according to the adsorption temperature and concentration of mercury in the carrier gas. In detail, the following conclusions can be drawn:

- i. The adsorption rate depends on the substrate temperature, both at the initial stages of adsorption and during the saturation of the surface. High temperature of the substrate leads to lower adsorption rate and less surface coverage.
- ii. The adsorption rate curves for Ag (111) display similar trend as the Au(111) adsorption curves; an initial fast adsorption and a saturation point at a later stage.

Therefore, increasing the concentration of mercury increases the level of saturation. Previous studies show that in a fairly high concentration, practically the whole film is amalgamated [50, 51]. This effect is quite perceivable, given the generally high mercury reactivity with Au and Ag.

Merging the two principal observations, it is apparent that the saturation level reflects the average density of physisorbed Hg atoms, and consequently depends on the adsorption conditions. The density of physisorbed atoms on a surface increases with increasing flux of atoms onto the surface and decreases with increasing temperature.

3.2. Adsorption to Cu(100) and Polycrystalline Copper Surfaces

It has been observed that copper has a high affinity for mercury [52]. In 1989, Dowben et al. [53] studied the electronic structure of mercury overlayers on Cu(100). They determined that mercury atoms are located 3.62 Å apart forming a c(2x2) structure on single-crystal copper, which presumably corresponds to 0.5 ML of adsorbed Hg. They also suggested the presence of strong lateral interactions between mercury atoms in the mercury adlayer.

The experiments on polycrystalline Cu surfaces at LT and RT are summarised in Table 3-1.

- On clean, polycrystalline copper surfaces the mercury coverage is 4.1 ML with a thickness of 1.18 nm at 82 K. On the contrary, at RT mercury reached nearly one ML of coverage which is equal to approximately 0.27 nm of thickness.
- In the case of chlorinated copper surfaces, surface coverage was even greater than clean Cu with thickness of 1.35 nm at LT. This corresponds to nearly 4.5 ML of adsorbed mercury. At RT, mercury adsorbed similarly to the clean Cu surface.
- Modification of polycrystalline Cu with oxygen resulted in the mercury coverage of 0.74 nm, corresponding to just over 2.5 ML. Mercury adsorbed on oxidized Cu at RT appears to form 1 ML of coverage.

Table 3-1: Results of mercury layer thickness on polycrystalline copper surfaces.

	Cu-Hg	Cu-Cl-Hg	Cu-O-Hg
Mercury adlayer thickness at LT	1.18 nm 4.4 ML	1.35 nm 4.5 ML	0.74 nm >2.5 ML
Mercury adlayer thickness at RT	~0.27 nm 1 ML	Similar to Cu-Hg at RT	Similar to Cu-Hg at RT

The results of the experiments point out the critical role of temperature to mercury adsorption processes. In all cases, mercury growth was laminar on the polycrystalline surface. It appears that the first ML on Cu is chemisorbed and stable at RT, whereas following layers, adsorbed at LT, are weakly adsorbed on top of the first mercury ML. Chlorine appears to favour adsorption. The slight increase may be due to a roughening reaction between chlorine and Cu that slightly increases the available surface area.

As far as desorption is concerned, results appear to be consistent with the observations of Paliwal et al. [54] that a mercury multilayer desorbs rapidly followed by slower desorption of the ML on the (111) face of silicon. For the clean and chlorinated Cu surfaces, desorption was completed in two steps; first, the top most layers desorbed at lower temperatures and then, at higher temperature, desorption of the layer bonded to the interface mercury layer, in contact with the substrate, took place. From the oxidized Cu surface, desorption was not as rapid as in the previous cases. This can be explained by

the reduction of bond strength of the first mercury layer due to oxidation, whereas desorption of additional layers occurred at the same temperatures as from the Cu surface. In all studied cases, desorption was complete prior to reaching RT.

3.3. Adsorption to Zn(0001) and Polycrystalline Zinc Surfaces

In all examined cases of Zn(0001) -clean, chlorinated or oxygenated- at any dosage of pretreatment, at RT, exposure to mercury did not result in the formation of a mercury layer. Similar behaviour was observed at LT for clean and chlorinated single-crystal zinc surfaces [15]. In contrast, traces of adsorbed mercury were detected onto oxygen pretreated Zn (0001) at LT, when the surface was treated with high oxygenation prior to mercury dosing. Lower oxygenation, both at RT and LT, did not result in mercury adsorption [15]. Polycrystalline Zn naturally has more available sites for adsorption than a pure Zn crystal. However, similar results of zero mercury coverage were observed onto clean and contaminated polycrystalline zinc at RT.

The set of experiments at LTs revealed different trends, as presented in Table 3-2. Pre-dosing the zinc substrate with chlorine did not aid in mercury capture. An identical pattern was observed after modification of polycrystalline zinc with oxygen, as it did not allow for the formation of a detectable layer of mercury on the zinc oxide surface, despite extended dosing [15]. The only case where mercury adsorbed to zinc surface was for the clean polycrystalline surface [15].

Desorption from polycrystalline Zn behaved similarly to copper surfaces [15], occurring at an initial and secondary desorption step.

Table 3-2: Results of mercury layer thickness on polycrystalline zinc surfaces.

	Zn-Hg	Zn-Cl-Hg	Zn-O-Hg
Mercury adlayer thickness at LT	0.31nm 1 ML	No mercury detected	No mercury detected
Mercury adlayer thickness at RT	No mercury detected	No mercury detected	No mercury detected

3.4. Adsorption to Fe(100) and Polycrystalline Iron Surfaces

Despite the significant effects of mercury contamination, few sources and published data are available concerning adsorption kinetics of mercury on steel. R.G. Jones and D.L. Perry [16] examined the chemisorption of mercury on Fe(100) in Ultra High Vacuum (UHV) conditions above room temperature, where the gas phase was primarily composed of mercury, using Auger Electron Spectrometry, LEED and thermal desorption measurements. The findings of the study are reported:

- For full coverage of the surface, there is one atom per four-fold site.
- Constant sticking probability is close to unity up to surface coverage of 0.85.
- The lattice constant for the Fe(100) is 0.287 nm, whilst the size of the mercury atom is 0.296 nm or 0.3005 nm. It becomes obvious that whichever the case, the mercury atom is slightly bigger than the iron atom, thus it must be compressed for a four-fold site arrangement. Compression would be expected to give rise to repulsive interactions between adsorbed atoms, as confirmed by the adsorption isotherms.
- The saturated room coverage varies with pressure.
- At room temperature, the mercury adlayer is in a state of equilibrium with the mercury vapour at the pressures used and remains immobile in a 1x1 structure.

- There appears to be no activation energy for adsorption. This would be expected given the monatomic nature of mercury gas.
- The activation energy of desorption increases with decreasing coverage, which supports the hypothesis of adsorbate-adsorbate repulsive interactions-less energy required to desorb atoms that repel each other.

As with zinc and copper surfaces, Roseborough et al. [14, 17] studied mercury adsorption and desorption on iron, using TDAES. Dosing mercury at low temperatures onto the clean iron substrate caused mercury adsorption until a saturated layer formed. The coverage corresponded to nearly 3 ML of mercury on the clean iron surface. At RT, mercury dosed onto iron formed only a single monolayer on the surface, whereas at extended dosing, no additional mercury adsorbed.

In the case of oxygen-pretreated polycrystalline iron [14, 17], at low temperature, the saturated coverage of mercury reached a thickness of approximately 2 ML at high dosage. In contrast to LTs, mercury did not adsorb onto the oxygenated iron surfaces at RT. It should be noted that in the case of oxygenated iron, the formation of iron oxide is thermodynamically favoured.

Similar behaviour is displayed by the Fe-Cl-Hg system, where the mercury coverage was just less than 2 ML, after a high mercury dose at LT [14, 17]. Again, at 298 K, mercury did not form a layer onto the chlorinated surface. This is indicative of the intense contrast between low and high temperature, as adsorption is highly dependent on this parameter.

Table 3-3: Results of mercury layer thickness on polycrystalline iron surfaces.

	Fe-Hg	Fe-Cl-Hg	Fe-O-Hg
Mercury adlayer thickness at LT	0.66 3 ML	0.45 <2 ML	0.42 <2 ML
Mercury adlayer thickness at RT	0.23 1 ML	No mercury detected	No mercury detected

Desorption patterns [14, 17] for both the iron-mercury and the chlorinated iron-mercury systems reveal consistency with the results of Paliwal et al. [54], as in the case of polycrystalline copper and zinc surfaces. Desorption takes place in two separate stages. For clean iron surfaces, at room temperature, the coverage left on the surface was ~1 ML. In the case of oxygenated iron, no mercury traces were detected at room temperature. As could be expected due to the stability of iron oxide, the oxygen did not desorb from the surface of the iron at LT or at room temperature, and neither did the mercury on the surface affect the surface concentration of oxygen. Lastly, as with clean iron, at 298 K, considerably less than a ML of Hg remained on the surface of chlorinated iron. However, it shall be noted that the chlorinated and oxygenated iron surfaces have a less steep desorption of mercury as compared to clean iron systems [14, 17].

Summarising the results of mercury adsorption onto polycrystalline metal surfaces, it is established that low temperatures are conducive to mercury adsorption due to physisorption and subsequent lateral mercury interactions in mercury adlayers. Chlorine appeared to favour mercury adsorption, as determined by the increased mercury coverage at low temperatures on the polycrystalline iron, copper and zinc. Oxygen, however, was found to be an inhibitor of mercury, most notably at room temperature. Mercury appeared to desorb in two main steps at increasing temperature, with small differences in desorption effects between chlorinated and oxygenated surfaces. Based on the literature review, with emphasis placed on polycrystalline iron surfaces, it can be concluded that at RT, which are closer to operating temperature of the pipeline, mercury adsorption is limited to monolayer formation. Moreover, contaminants such as oxygen and chlorine on the pipewall might hinder mercury adsorption. However, as natural gas

pipelines are made of steel, the mechanisms of mercury accumulation on steel surfaces, are to be further studied.

3.5. Mercury Adsorption in Operational Gas Pipelines

Bearing in mind that natural gas pipelines are primarily composed of steel, it is important to have a clear picture on the adsorption of mercury in industrial pipelines. The only available data, to the knowledge of the present author, are those of Wilhelm & Nelson [19]. Wilhelm & Nelson [19] suggest that one or more of the following processes are responsible for the concentration of mercury in process equipment and pipelines.

- a) Physical adsorption onto the steel surface;
- b) Physical adsorption onto iron oxide and iron sulphide surface scale deposits;
- c) Reaction with and / or incorporation into surface scale deposits;
- d) Absorption into the steel crystal lattice;
- e) Absorption into steel grain boundaries and reaction with localised compounds.
- f) Formation of an amalgam between mercury and steel;

In consonance with Jones' and Perry's findings [16], Wilhelm & Nelson [19] conclude that absorption of mercury into the crystal lattice of iron is improbable due to the relative size of mercury atoms, the diameter of which equals to 0.296 nm, compared to the interstitial space of iron atoms, the diameter of which is 0.287 nm.

Moreover, the possibility of an amalgam reaction with steel in gas transmission pipelines is not considered when developing the model, since mercury is found solely in gas phase. An amalgam reaction would require liquid mercury in contact with bare metal to proceed [19].

Experiments with steel coupons exposed in mercury vapour revealed that absorption into the crystal lattice or grain boundaries is irrelevant for steel, as no effect on steel mechanical properties was observed [19].

As a result, chemisorption to surface scales and physical adsorption appear to be the primary mechanisms for mercury uptake. A contaminated pipe specimen, which had been in service for 5 to 6 years with a gas stream containing 500 to 800 $\mu\text{g}/\text{Sm}^3$ of mercury, was cut and examined by the analytical techniques of Scanning Electron Microscopy and Energy Dispersive X-ray. A discrete layer of mercury sulphide, formed by the reaction of mercury vapour when gas stream contains H_2S , was found on top of the iron oxide layer. Further analysis showed that HgS and of Hg^{2+} chemically incorporated into the iron oxide accounted for less than 10% of the total mercury adsorbed by the sample. This observation allows chemisorption to be listed out as well, rendering physical adsorption accountable for mercury accumulation along the pipeline [19].

4. MODELLING OF ADSORPTION AND ADSORPTION-RELATED PARAMETER IDENTIFICATION

4.1. Modelling of Adsorption in Pipelines

Modelling of mercury adsorption in natural gas pipelines and estimation of time to breakthrough are, to the knowledge of the present author, lacking. Published scientific work has been primarily focused on the transport of contaminants, such as arsenate and chlorine, in Water Distribution Systems (WDS) [20-22].

The iron pipes, used to transport potable water, are exposed to pipe wall corrosion that poses numerous water quality concerns, including increased demand for disinfectant, release of soluble or particulate iron, and adsorption of contaminants [20]. Due to these concerns, the development of models that include adsorption, desorption and mass transfer phenomena of multiple species acted as a necessary extension onto the EPANET single-species model [23, 24].

Modelling approaches to describe adsorption to metal surfaces fall into two main categories: kinetic and equilibrium [21]. In kinetic models of adsorption, the rates of two distinct processes may contribute to the kinetics of the overall adsorption process: liquid-phase mass transfer of dissolved contaminant from the bulk fluid to the fluid adjacent to the pipe surface, and the kinetics of adsorption from the dissolved phase to the adsorbed phase on the pipe surface. Equilibrium models assume the adsorption reaction occurs quickly enough to be at equilibrium with respect to other transport processes and are, thus, based on isotherm models, such as the Langmuir adsorption isotherm [55].

The majority of adsorption models in WDS are based on the latter approach with the implementation of the Local Equilibrium Assumption (LEA) [21]. LEA allows both fast/equilibrium and slow/kinetic reaction dynamics to be written as a single set of ordinary differential equations (ODEs) that could be integrated over time to simulate changes in species concentrations [22].

Building a model for adsorption in pipelines requires incorporation of flow dynamics and mass transfer principles. The proposed models integrate both in order to describe the dominant phenomena that take place inside a water pipe [20, 21].

When the contaminant enters the pipe carried away in the bulk flow of water, it is subject to advection along the longitudinal axis of the pipe, as well as adsorption to the pipe wall surface [22]. To get to the pipe wall, the contaminant must travel through the laminar sublayer of turbulent flow, as described in Eq. 4-1 and 4-2.

$$\frac{d(C_{bulk}V_{bulk})}{dt} = -k_m A_{stagnant} \left(C_{bulk} - \frac{A_{pipe}}{V_{stagnant}} W \right) \quad Eq. 4-1$$

$$\frac{d(WA_{pipe})}{dt} = k_m A_{stagnant} \left(C_{bulk} - \frac{A_{pipe}}{V_{stagnant}} W \right) \quad Eq. 4-2$$

where, V_{bulk} is the bulk volume, C_{bulk} is the contaminant's volumetric concentration in the bulk phase, $V_{stagnant}$ is the volume of the laminar sublayer of turbulent flow, W the contaminant's areal concentration close to the wall, k_m the mass transfer coefficient, $A_{stagnant}$ the area of the boundary between the bulk flow and wall regions, and A_{pipe} the area of the pipe surface.

Combined with an advection term to describe the time varying concentration at a given point in the bulk flow [22], Eq. 4-1 can be rearranged into Eq. 4-3, whereas the dissolved concentration in the boundary layer is assumed to have zero velocity.

$$\frac{\partial C_{bulk}}{\partial t} = -u \frac{\partial C_{bulk}}{\partial x} - \frac{k_m A_{stagnant}}{V_{bulk}} \left(C_{bulk} - \frac{A_{pipe}}{V_{stagnant}} W \right) \quad Eq. 4-3$$

where, u is the bulk flow velocity and x is the longitudinal axis of the pipe.

After being transported to the surface, the contaminant, expressed by the dissolved concentration in the boundary layer, resides in the exterior portion of the pipe wall corrosion layer, available for adsorption. The adsorption process follows second order kinetics according to the Langmuir adsorption model [22]. In this way, Eq. 4-2 can be transformed into:

$$\frac{dW}{dt} = \frac{k_m A_{stagnant}}{A_{pipe}} \left(C_{bulk} - \frac{A_{pipe}}{V_{stagnant}} W \right) - k_{ads} W (S_{max} - C_{ad}) + k_{des} C_{ad} \quad Eq. 4-4$$

With

$$\frac{dC_{ad}}{dt} = k_{ads} W (S_{max} - C_{ad}) - k_{des} C_{ad} \quad Eq. 4-5$$

where, S_{max} is the maximum surface coverage possible on the pipe wall and C_{ad} the adsorbed concentration on the pipe wall. The LEA states that the contaminant's concentration in the wall region, W , is in equilibrium with the adsorbed concentration, C_{ad} .

The adsorption model, which practically constitutes of three differential equations (Eq. 4-3, 4-4, 4-5) is implemented in EPANET-MSX [56], after necessary modifications, regarding the units used [57], and parameter calculations.

Surface and pore diffusion phenomena may be applicable in the case of contaminants' adsorption when developed for WDS. Nevertheless, detailed analysis of those is excluded in the current study.

4.2. Activation Energy of Desorption and Pre-exponential Factor

Kinetic parameters of desorption are important to be defined for successful model development. It has been reported that for desorption from a monocrystalline surface, the activation energy, $E_{\alpha,des}$ and the pre-exponential factor ν , are not constant but vary with surface coverage. This is often the case due to the adsorbate lateral interactions of attraction or repulsiveness and may lead to multiple binding states [58]. Therefore, the dependence of desorption kinetic parameters on surface coverage may be indicative of changes in the adsorbate structure.

There exist several procedures through which the activation energy, $E_{\alpha,des}$ and/or the pre-exponential factor, ν , can be derived from thermal desorption spectra. The procedures are practically divided into two categories [59]:

1. The integral approach
2. The differential approach

The integral method is used to extract coverage-independent kinetic parameters from a single desorption peak, whereas the differential approach may be applied to derive coverage-dependent kinetic parameters. The differential approach uses pairs of desorption rate/temperature from desorption spectra to prepare an Arrhenius-type plot and relate the slope and intercept to $E_{\alpha,des}$ and ν , respectively. The differential approach, mainly, includes two different methods; Isotherm construction from a series of

desorption spectra or the use of desorption rate/temperature data from the onset of desorption in the low temperature tail (or the threshold region) of a single desorption spectrum [59].

Guo and Yates [59] studied the effect of temperature and surface coverage on the configuration of kinetic parameters, in the case of carbon monoxide adsorption on Pd (111) single-crystal surface. The adsorption and desorption of CO on Pd(111) exhibits similarities to the adsorption of Hg, as far as the nature of adsorption and the order of desorption are concerned. Further explanation on adsorption and desorption kinetics is provided in Sections 5.4 and 5.5. The method chosen to study the kinetic parameters is the TTPD method (Threshold Temperature Programmed Desorption), which falls into the differential approach category. The main findings of the study are listed below.

- 1) Desorption activation energy decreases with surface coverage, probably due to the increasing repulsive lateral interactions.
- 2) The (effective) desorption activation energy at zero coverage remains constant (148.6 kJ/mol), regardless of the adsorption temperature (87 and 200 K).
- 3) For fixed coverage, the activation energy of desorption increases with increasing adsorption temperature.
- 4) The pre-exponential factor decreases with increasing surface coverage and decreasing adsorption temperatures. However, on most occasions, the coverage dependence of the pre-exponential factor is neglected and ν is assumed to be constant.
- 5) A strong linear correlation, well-known as compensation effect, is observed between $E_{\alpha,des}$ and ν . Evidence from the literature shows that the demonstration of the compensation effect often follows the relationship [60]:

$$\ln\nu(\theta) = c \cdot E_{\alpha,des}(\theta) + d \quad \text{Eq. 4-6}$$

where, c and d constants.

Similar trends were observed for mercury desorption off tungsten [18] and iron single-crystal surfaces [16]. In the case of tungsten, it also reaffirmed that the production of identical desorption curves can be achieved by successful adjustment between the values of pre-exponential and the activation energy, each of which could fit the experimental results [18]. Based on these observations, a function between activation energy of desorption, surface coverage and pre-exponential factor was produced for mercury on iron surfaces, as detailed in Section 7.9. Compensation effect was studied, as well, and its impact on surface coverage and breakthrough time was investigated, as a case of sensitivity analysis, in Section 8.2.5.

4.3. Adsorption Capacity and SSA

The results of Jones & Perry [16] reveal that mercury forms a monolayer on the adsorbed surface in full coverage as mercury atoms pack together with a cubic lattice structure on the surface of iron. The adsorption capacity is equal to 0.0038 g/m². An industrial steel gas pipeline adsorbs 0.6 to 3 grams of mercury per unit of pipeline surface area [19], as it takes into account factors such as pipe wall roughness, mill-scale and corrosion products that build up on the pipe wall. The value of adsorption capacity of the pipe is, often, expressed with the term Specific Surface Area (SSA). Specific Surface Area practically describes the portion of the total surface area that is available for adsorption [61]. In the present study, Specific Surface Area is expressed as the fraction of the adsorption capacity of the internal surface of the pipeline to the mass

of the formed mercury monolayer. This approach facilitates its introduction in the model equations.

Gas Adsorption analysis is commonly used for surface area and porosity measurements. This involves exposing solid materials to gases or vapors at a variety of conditions and evaluating either the weight uptake or the sample volume [62]. The Brunauer, Emmett and Teller (BET) technique is the most common method for determining the Specific Surface Area (SSA) [63]. Nevertheless, Specific Surface Area measurements for gas pipeline internal surfaces are not currently available, thus its value constitutes a sensitivity case for modelling.

4.4. UMR-PRU Model

The UMR-PRU model, originally proposed by Voutsas et al. [64] belongs to the class of EoS/ G^E models and combines Peng-Robinson EoS with Original UNIFAC, through the Universal Mixing Rules (UMR) [25], hence the abbreviation Universal-Mixing-Rule-Peng-Robinson-UNIFAC. The UMR mixing rules are modifications of the zero-pressure mixing rule MHV1[65] and are presented in Eq. 4-7 and 4-8.

$$\frac{a}{bRT} = \frac{1}{A_{constant}} \frac{G_{AC}^{E,SG} + G_{AC}^{E,res}}{RT} + \sum_i z_i \frac{a_i}{b_i RT} \quad \text{Eq. 4-7}$$

$$b = \sum_i \sum_j z_i z_j b_{ij} \quad \text{Eq. 4-8}$$

With

$$b_{ij}^{\frac{1}{2}} = \frac{b_i^{\frac{1}{2}} + b_j^{\frac{1}{2}}}{2} \quad \text{Eq. 4-9}$$

where, z_i is the molar fraction of component i in the mixture, a is the EoS attractive parameter, b is the co-volume, R the universal gas constant, T the absolute temperature, $A_{constant}$ an EoS specific constant ($A_{constant} = -0.53$ for PR EoS), $G_{AC}^{E,SG}$, $G_{AC}^{E,res}$ are the Staverman-Guggenheim and the residual terms of original UNIFAC, respectively. The Florry-Hugging term of the UNIFAC combinatorial term is omitted as explained by Voutsas et al. [25].

The UMR-PRU model has been successfully applied to various hydrocarbon mixtures with emphasis on dry natural gases [64, 66], polar and associating mixtures [67] and quite recently, mixtures that contain mercury [32]. From binary mixtures to multi-component systems simulating natural gas, gas condensates and oils, this model yields comparable or superior predictions in various types of vapour-liquid equilibrium, dew points, K values and liquid dropouts [32].

5. MODEL DESCRIPTION

5.1. Model description, assumptions and simplifications

The adsorption of mercury in operational pipelines is considered to comprise of three separate phenomena; the axial flow of the gas and, subsequently, the axial flow of mercury in traces, along the pipeline, the radial flow of mercury from the bulk phase to a stagnant boundary layer at the pipe wall and the adsorption of mercury onto the steel surface. Equally the reverse process can take place where an atom of mercury can desorb off the pipe wall and diffuse back into the bulk gas.

To account for the axial flow of the gas, which is considered fully developed, the pipeline is discretized into a user-selected number of sections in the length direction, called segments, as illustrated in Figure 5-1. Within each segment, it is assumed that the bulk gas flow is well mixed, due to turbulence, and as a result, gas composition, and all intensive and extensive properties of the gas are uniform. Segmentation is also used to estimate the pressure drop due to friction.

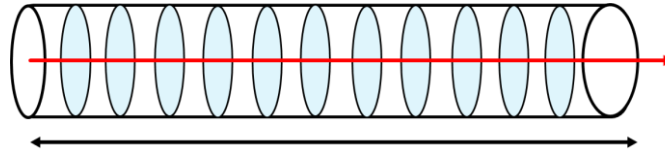


Illustration 5-1: Pipeline segmentation.

The phenomenon is considered isothermal. Properties are calculated either from the UMR-PRU model [25] or from appropriate methods at the temperature and pressure of each segment. The axial flow of mercury is mathematically described by the respective mass balance in the bulk gas.

Mercury also flows in the radial direction from the bulk gas to the stagnant boundary layer. The classical boundary layer approach is used to determine the mass transfer rate for adsorption and desorption of mercury. The mercury atoms diffuse from the bulk gas through the stagnant boundary layer, which accounts for all mass transfer resistance, before they are adsorbed onto the non-occupied spots of the pipe wall. The mercury concentration inside the boundary layer close to surface of the pipeline is assumed to be in equilibrium with the adsorbed mercury onto the pipe wall.

Due to the turbulence of the flow, the bulk gas phase is well-mixed. As a result, the radial concentration profile is constant. In the axial direction, the velocity is assumed zero in the stagnant boundary layer. Therefore, any axial mass transfer is neglected. The concentration of mercury in the stagnant layer is mathematically formulated by the mercury mass balance in the stagnant layer.

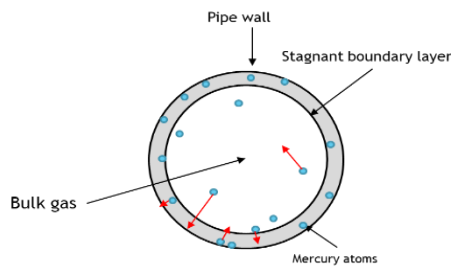


Illustration 5-2: Illustration of the radial direction of the pipe.

As adsorption is a dynamic process, the reverse process also takes place where an atom of mercury can desorb off the pipe wall and diffuse back into the bulk gas. At equilibrium,

the rate of adsorption and desorption are balanced (Figure 5-2). The available mercury in the stagnant layer is then adsorbed onto and desorbed from the pipe wall. This is formulated as two different phenomena, governed by two different rates. The adsorption is considered as non-activated, monolayer physical adsorption onto the steel pipeline surface, which is considered smooth and free of surface-scale deposits. The desorption is treated as a chemical reaction, between the adsorbed and desorbed mercury atoms.

In the rest of the chapter, each term of the model is described in detail.

5.2. Mass Transfer in the Bulk Gas

The mass balance of mercury in the bulk gas in each n segment, for non-steady state conditions, contains the terms of inflow, outflow, mercury diffusion from the bulk gas into the stagnant layer and vice-versa and mercury accumulation in the bulk.

$$0 = F_{vol\ in(total)}^v(n) [C_{bulk(Hg)}(t, (n-1)) - C_{bulk(Hg)}(t, n)] + k_m(n) A_{stagnant} [C_{stagnant(Hg)}(t, n) - C_{bulk(Hg)}(t, n)] - \frac{dC_{bulk(Hg)}(t, n) V_{bulk}(n)}{dt} \quad Eq. 5-1$$

where, $F_{vol\ in(total)}^v$ is the inlet volumetric flowrate, $C_{bulk(Hg)}$ is the mercury concentration in the bulk phase, k_m the mass transfer coefficient, $C_{stagnant(Hg)}$ the mercury concentration in the stagnant boundary layer, V_{bulk} is the volume of the bulk gas and the index n refers to each segment.

Assuming that the bulk volume of a segment is independent of time and rearranging Eq. 5-2 gives

$$\frac{dC_{bulk(Hg)}(t, n)}{dt} = \frac{F_{vol\ in(total)}^v(n) [C_{bulk(Hg)}(t, (n-1)) - C_{bulk(Hg)}(t, n)] + k_m(n) A_{stagnant} [C_{stagnant(Hg)}(t, n) - C_{bulk(Hg)}(t, n)]}{V_{bulk}(n)} \quad Eq. 5-2$$

For $n=1$, the concentration of the previous segment is set to the inlet concentration of the transport pipeline.

5.3. Mass Transfer in the Stagnant Boundary Layer

For the stagnant boundary layer, it is assumed that the velocity is zero. Using the same principles as for the bulk gas, the resulting mass balance describes the phenomena of mercury diffusion from the bulk gas into the stagnant layer and vice-versa, adsorption on or desorption from the steel surface and accumulation in the stagnant layer, respectively.

$$\frac{dC_{stagnant(Hg)}(t, n)}{dt} = \frac{k_m(n) A_{stagnant} [C_{bulk(Hg)}(t, n) - C_{stagnant(Hg)}(t, n)] - \frac{d\theta(t, n)}{dt} A_{pipe} q_{max} SSA}{V_{stagnant}(n)} \quad Eq. 5-3$$

where, $V_{stagnant}$ is the volume of the stagnant boundary layer, A_{pipe} is the internal area of the pipe, SSA is the Specific Surface Area, q_{max} the maximum surface concentration, as defined in the next subsection, and $\frac{d\theta(t, n)}{dt}$ refers to the rate difference between the adsorption and desorption processes, as analysed in Section 5.4 and 5.5.

5.4. Adsorption Kinetics on Iron Surfaces

Jones & Perry [16] experiments are conducted at a low vacuum to ensure that the vapour phase is composed of pure mercury. This approach ensures that the gas phase is

homogeneous. Hence, any gas phase mass transfer resistance is eliminated, and the intrinsic rate of adsorption and desorption is to be determined. According to Jones and Perry [16], for the first-order adsorption of mercury on iron, there is zero activation energy associated with adsorption, due to the monoatomic nature of mercury. Therefore, in Eq. 2-10, the exponential term that includes activation energy for adsorption is set equal to 1 and it shall, then, be written as

$$Rate_{ads} = \frac{d\theta}{dt} = \frac{pN_A}{\sqrt{2\pi M_{w(Hg)}RT}} \cdot \frac{s_o(1-\theta)}{N_{max}} \quad Eq. 5-4$$

Moreover, it is convenient to express surface coverage in terms of mercury concentration to relate mass transfer to kinetics. Since the mixture of gas and mercury does not behave ideally during gas transportation, partial pressure may be substituted with the fugacity of mercury and Eq. 5-4 is transformed as

$$\frac{d\theta}{dt} = \frac{\varphi_{(Hg)}^v C_{stagnant(Hg)} ZRTN_A}{M_{w(Hg)} \sqrt{2\pi M_{w(Hg)}RT}} \cdot \frac{s_o(1-\theta)}{N_{max}} \quad Eq. 5-5$$

where, $\varphi_{(Hg)}^v$ is the fugacity coefficient of mercury in the gas mixture, Z is the compressibility factor and $M_{w(Hg)}$ the molecular weight of mercury.

N_{max} can be calculated knowing that one mercury atom adsorbs per unit cell surface area.

$$N_{max} = \frac{1 \text{ atom}_{(Hg)}}{d_{(Fe)}^2} \quad Eq. 5-6$$

For Eq. 5-3, the maximum surface concentration, q_{max} , can be calculated as in Eq. 5-7.

$$q_{max} = N_{max} \cdot \frac{M_{w(Hg)}}{N_A} \quad Eq. 5-7$$

5.5. Desorption Kinetics on Iron Surfaces

Jones' & Perry's [16] experiments indicated that the desorption kinetics of mercury on iron are first order with activation energy that increases with decreasing coverage, which confirms the hypothesis of adsorbate-adsorbate repulsive interactions. Therefore, the rate of mercury desorption from the pipe wall is described by Eq. 5-8.

$$Rate_{des} = \frac{d\theta}{dt} = -\nu\theta \exp\left[-\frac{(151-28.82\theta)}{RT}\right] \quad Eq. 5-8$$

The replacement of the energy activation of desorption by the expression of surface coverage is justified by calculations based on the Jones' & Perry's observations [16] and the process of extracting the correlation between $E_{\alpha,des}$ and θ is thoroughly explained in Section 7.9. As it has already been mentioned in Section 3.4, the activation energy for desorption is a function of surface coverage, due to the repulsive adsorbate-adsorbate interactions that exist between mercury atoms and depends on the pre-exponential factor.

The differential equation for surface coverage (Eq. 5-9) derives from merging the adsorption and the desorption kinetics terms

$$\frac{d\theta}{dt} = \frac{\varphi_{(Hg)}^v C_{stagnant(Hg)} ZRTN_A}{M_{w(Hg)} \sqrt{2\pi M_{w(Hg)}RT}} \cdot \frac{s_o(1-\theta)}{N_{max}} - \nu\theta \exp\left[-\frac{(151-28.82\theta)}{RT}\right] \quad Eq. 5-9$$

6. MODEL IMPLEMENTATION

6.1. Fixed Parameters

The dynamic adsorption model of mercury in gas pipelines has been applied to study the breakthrough profile in a 20 km long pipeline that operates at 6°C. Natural gas enters the pipeline at 143.2 bara, with composition and flowrate, as detailed in Table 6-1.

Table 6-1: Pipeline characteristics and natural gas inlet conditions

Parameter	Value
P_{in}	143.2 bara
$F_{vol,in total}$	24E6 Sm ³ /d
T	279.15 K
L	20,000 m
d_{pipe}	0.7112 m
Composition	
Component	Molar fraction
Mercury	5.87462E-10
Carbon Dioxide	2.86724E-2
Methane	8.04302E-1
Ethane	9.4531E-2
Propane	4.45561E-2
i-butane	5.77915E-3
n-butane	1.14475E-2
i-pentane	2.30854E-3
n-pentane	2.26116E-3
Water	6.60068E-8
Nitrogen	6.14254E-3

6.2. Model Solving

The model comprises three ordinary differential equations (ODEs). The two equations describe gas phase bulk and stagnant layer concentration of mercury and adsorbed on the pipe wall (Eq.5-2 & Eq.5-3), while the third equation expresses the coverage of the surface as determined by the rate of adsorption and desorption (Eq.5-7). The system is solved sequentially for all segments at each timestep.

In the model development, variables are registered either as space-dependent or as time-and-space dependent. This categorisation facilitates solving mass balances and adsorption kinetics equations. It is highlighted that space-dependent variables are only affected by the pipeline's pressure profile, whereas time dependent variables are mostly correlated with kinetics. Moreover, time is treated as a continuous variable, while space is a discretised variable.

The necessary steps to build the model are primarily based on:

1. The calculation of pressure drop along the pipeline as physical properties are highly affected by pressure changes.
2. The determination of mass transfer coefficient across the stagnant boundary layer.
3. The use of mass transfer coefficient to calculate the surface area of the stagnant boundary layer and the volumes of the bulk gas and stagnant boundary layer, respectively, which act as defined control volumes for solving ODEs.
4. The determination of adsorption and desorption kinetics, specifically for mercury on iron, including the maximum surface concentration at saturation.

The model is implemented in MATLAB [10] and solved using the built-in MATLAB solver ode15s for stiff systems of ordinary differential equations, with timestep chosen internally by the solver [68].

6.3. Initial Conditions and Specification Limits

To run the model, the initial and exit conditions must be set. In more detail, when the flow enters the pipeline for the first time:

- a) The pipe-wall is considered smooth and free of surface-scale deposits, therefore pipe roughness is set to zero.
- b) The mercury concentration of the stagnant boundary layer is set to zero as an initial condition.
- c) The surface coverage of adsorbed mercury is set to zero as an initial condition.

The amount of time it takes for the mercury concentration to reach a critical point, above which the installation of removal systems becomes imperative, is defined as time to breakthrough. The concentration of mercury for entry in the reception facility is limited to 10 ng/Sm^3 , which is considered the critical mercury concentration in the outlet of the pipeline, for the gas industry. For mercury concentrations higher than 10 ng/Sm^3 , the installation of a Mercury Removal Unit (MRU) is obligatory for natural gas treatment.

7. MODEL COMPONENTS AND PARAMETERS

7.1. Segmentation

In order to investigate the effect of segmentation on breakthrough time, simulations were performed for mercury inlet concentration equal to 5000 ng/Sm³ and SSA equal to 1, for varying segment number from 50 segments to 1000. In finite element analysis, mesh density is a critical issue which closely relates to the accuracy of the finite element models while directly determines their complexity level [26]. Increased number of segments is expected to produce more accurate results. However, higher density meshes usually take longer to analyse. In Figure 7-1, it is observed that the model is very sensitive when only few segments are implemented, and breakthrough time differences are levelled off as the number of segments increases. Namely, when opting for a number of 500 segments or higher, the solution appears insensitive to segmentation. To verify this claim, the deviations in breakthrough time due to segmentation are reported in Table 7-1.

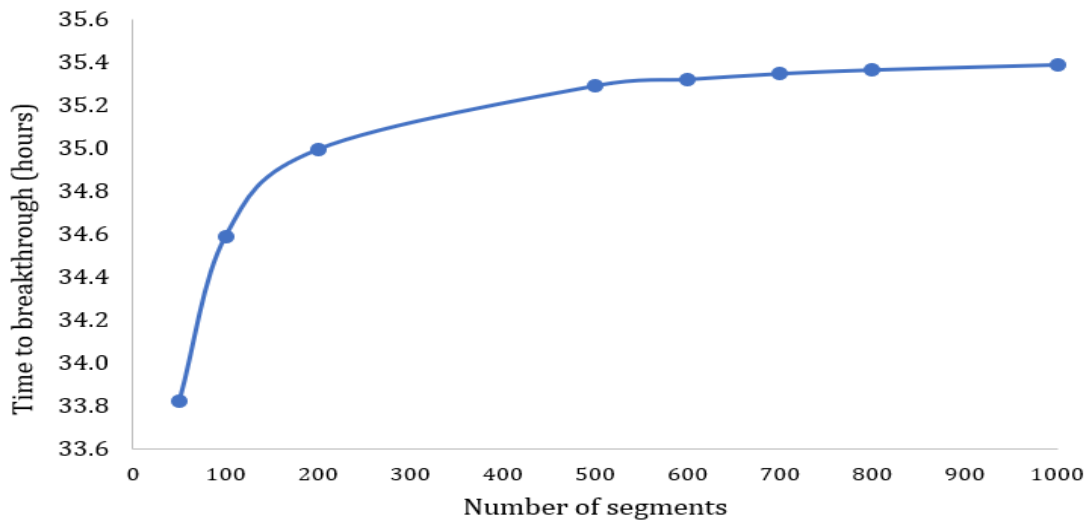


Figure 7-1: The effect of segmentation on the accuracy of model's solution (breakthrough time).

Table 7-1: Deviations in breakthrough time due to segmentation (Mercury Inlet concentration: 5000 ng/Sm³ and SSA=1).

Number of segments	Time to breakthrough (h)	% RD*
50	33.8	-
100	34.6	2.3
200	35.0	1.2
500	35.3	0.9
600	35.3	0.1
700	35.3	0.1
800	35.4	0.1
1000	35.4	0.1

*The relative difference is calculated as:

$$RD = \frac{\text{Time to breakthrough (current value of segments)} - \text{Time to breakthrough (previous value of segments)}}{\text{Time to breakthrough (previous value of segments)}}$$

The main criterion for segmentation in the developed model is a trade-off between computational time and deviation in model results. Computational time is measured in

CPU time that is defined as the time for which a Central Processing Unit (CPU) was used for processing instructions of a computer program or operating system [69]. In Figure 7-2, the CPU time used by MATLAB, for each run, shows an exponential increase as segmentation becomes denser. Given the results of Table 7-1 and Figure 7-2, the number of segments chosen for model development is 800, which also ensures relatively smooth mercury concentration and adsorption profiles.

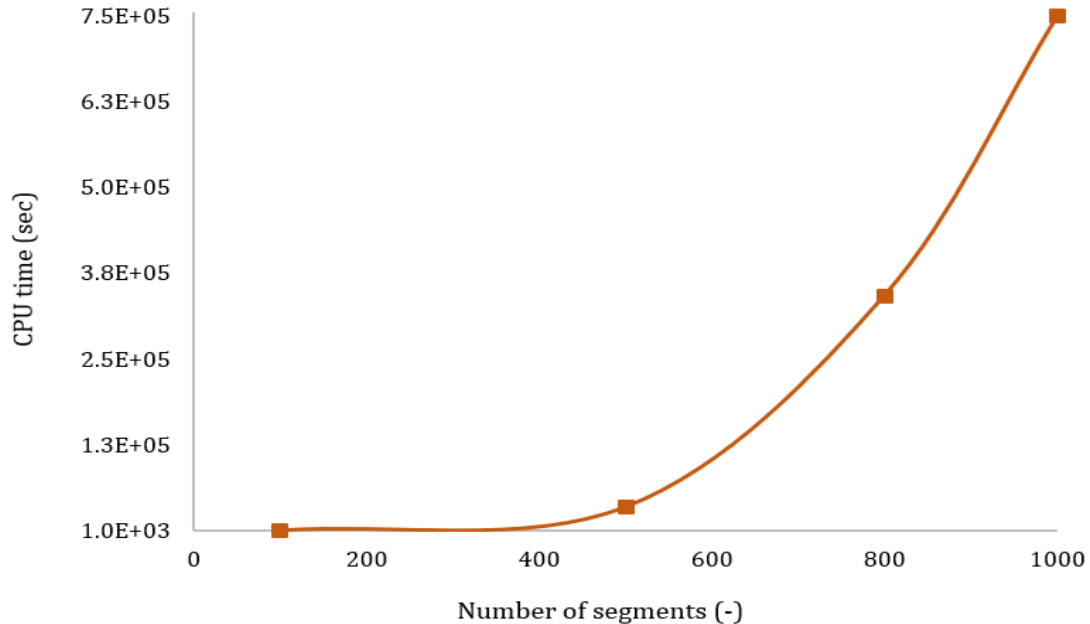


Figure 7-2: CPU time vs number of segments.

7.2. Investigation of Flow's Compressibility

It is of paramount importance to investigate whether the natural gas flow, at given pressure, temperature and gas composition, is compressible or not, as compressibility directly affects pressure drop along the pipeline.

The criteria set out for compressibility are mainly based on the calculation of the Mach number (M_a). For an incompressible flow, M_a shall be equal to or less than 0.3 [70].

$$M_a = \frac{u}{w} \quad \text{Eq. 7- 1}$$

where, u is the fluid velocity and w is the speed of sound at given conditions.

Assuming an outlet pipeline pressure of 140.0 bar, the speed of sound calculated for pure methane at 6°C is 452.41 m/s, calculated by NIST [71]. For the gas mixture, excluding water and mercury traces, at the same conditions, the sound velocity is calculated with UMR-New model equal to 400.40 m/s. The calculated speed of the natural gas in the inlet and outlet of the pipe, respectively, is listed in the Appendix.

Table 7-2: Calculation of the Mach number.

M_a	Mixture
0.066	Pure Methane
0.074	Natural gas

It is evident that in the case of the examined flow, whichever speed of sound is used for the calculation of the Mach number (Table 7-2), $M_\alpha \ll 0.3$. Hence, the flow shall be considered incompressible.

7.3. Pressure Drop

In the case of an incompressible gas flow, pressure drop along the pipeline can be calculated using the Darcy-Weisbach equation [72].

$$P_{out}(n) = P_{in}(n) - f_D(n) \cdot \frac{x(n)}{d_{pipe}} \cdot \frac{\rho(n)u(n)^2}{2} \quad Eq. 7-2$$

where, P_{in} and P_{out} is the pressure in the inlet and exit of each n segment, f_D is the friction factor, x is the length of discrete section, d_{pipe} is the internal diameter of the pipe, ρ the gas density and u the fluid's velocity.

The friction factor is given by Petukhov's equation (Eq. 7-8) for smooth tubes [73]

$$f_D(n) = (0.79 \ln(Re(n)) - 1.64)^{-2} \quad Eq. 7-3$$

With Reynolds number (Re) given by the formula

$$Re = \frac{\rho \cdot u \cdot d_{pipe}}{\mu} \quad Eq. 7-4$$

where, μ accounts for the dynamic viscosity.

7.4. Mass Transfer Coefficient

The mass transfer coefficient quantifies the diffusion of mercury from the bulk gas into the stagnant layer and vice-versa. It can be found from [74]:

$$k_m(n) = \frac{Sh(n)D(n)}{d_{pipe}} \quad Eq. 7-5$$

where, k_m is the mass transfer coefficient, Sh is the Sherwood dimensionless number, D is the diffusion coefficient.

Assuming fully developed turbulent flow, as Eq. 7-6 is applicable to $Re > 2100$ and $0.6 < Sc < 3$ for gas flowing inside a pipe [75], the Sherwood number can be calculated according to the following equation.

$$Sh(n) = 0.023 Re(n)^{4/5} Sc(n)^{1/3} \quad Eq. 7-6$$

Where, Sc is the Schmidt number, calculated as in Eq. 7-7 [74]:

$$Sc(n) = \frac{\mu(n)}{\rho(n)D(n)} \quad Eq. 7-7$$

7.5. Stagnant Boundary Layer in a Discrete Section

The hydrodynamics boundary layer thickness is defined as the distance from a solid object to where the fluid velocity is 99% of the bulk velocity. Moreover, the mass transfer layer thickness describes the distance from a solid object to where the concentration of the diffusing species is 99% of the bulk concentration [76, 77]. It is typical for diffusive

transport to be modelled by treating the fluid layer next to a solid boundary as a stagnant film of thickness δ [78].

Assuming that the thickness of the stagnant boundary layer is half of the thickness of the concentration boundary layer [20], the diameter of the bulk region can be calculated as

$$\delta(n) = \frac{\delta_c(n)}{2} = \frac{1}{2} \cdot \frac{D(n)}{k_m(n)} \quad \text{Eq. 7-8}$$

$$d_{bulk}(n) = d_{pipe} - 2\delta(n) \quad \text{Eq. 7-9}$$

where, δ is the thickness of the stagnant boundary layer, δ_c is the thickness of the concentration boundary layer and d_{bulk} is the diameter of the bulk control volume.

Taking into consideration Eq. 7-8 & 7.9, the volume of the bulk gas, V_{bulk} , the volume of the pipe, V_{pipe} , and the volume of the boundary layer, $V_{stagnant}$, of each discrete section are, respectively, given by:

$$V_{bulk}(n) = \pi \cdot \left(\frac{d_{bulk}(n)}{2}\right)^2 \cdot \frac{L}{n} \quad \text{Eq. 7-10}$$

$$V_{pipe} = \pi \cdot \left(\frac{d_{pipe}}{2}\right)^2 \cdot \frac{L}{n} \quad \text{Eq. 7-11}$$

$$V_{stagnant}(n) = V_{pipe} - V_{bulk}(n) \quad \text{Eq. 7-12}$$

Similarly, the surface area of the stagnant boundary layer, $A_{stagnant}$, as well as the internal surface area of the pipe, A_{pipe} , are described by the following equations.

$$A_{stagnant}(n) = \pi \cdot d_{bulk}(n) \cdot \frac{L}{n} \quad \text{Eq. 7-13}$$

$$A_{pipe} = \pi \cdot d_{pipe} \cdot \frac{L}{n} \quad \text{Eq. 7-14}$$

7.6. Other properties

The UMR-PRU model [25] is used for calculation of various properties such as density, fugacity coefficient and compressibility factor of the fluid. Approximate values of these properties are shown in the Appendix.

7.7. Diffusivity

To simplify the calculation of diffusion coefficient, D , it is assumed that natural gas is a binary mixture of mercury and methane. A predictive theoretical equation, which can be used to determine diffusivity at low and moderate pressures is Chapman-Enskog equation [79]. Chapman-Enskog theory [79] presents equations for dynamics of a multicomponent gas mixture in states close to local equilibrium.

Mutual-diffusion, defined by the coefficient D , can be viewed as diffusion of species A at infinite dilution through species B, or equivalently, diffusion of species A at infinite dilution through species B [80].

$$D = \frac{1.86 \cdot 10^{-3} \cdot T^{3/2} \cdot \left(\frac{1}{Mw_A} + \frac{1}{Mw_B}\right)^{1/2}}{P \cdot \sigma_{AB}^2 \cdot \Omega} \quad \text{Eq. 7-15}$$

where, Ω is the collision integral for the Lennard-Jones potential and σ_{AB} is the arithmetic average of the collision diameter of the two components, A and B, as expressed in Eq. 7-16.

$$\sigma_{AB} = 0.5(\sigma_A + \sigma_B) \quad \text{Eq. 7-16}$$

The dimensionless quantity Ω is usually of order one and depends on an integration of the interaction between two species, as described by the Lennard-Jones potential [81]. It virtually corrects the above stated equation for deviations from an idealised, rigid-sphere model for the interaction of gas molecules. In the present study, the value of Ω is interpolated and reported in Table 7-3.

To calculate theoretical binary diffusion coefficients for a given gas pair, one uses values of σ_{AB} and Ω , which are tabulated in Hirschfelder et al. [82]. The collision integral Ω can be obtained from tables when the energy of interaction ε_{AB} is known.

$$\frac{\varepsilon_{AB}}{k} = \frac{\sqrt{\varepsilon_A \varepsilon_B}}{k} \quad \text{Eq. 7-17}$$

where, $\frac{\varepsilon}{k}$ is the parameter of the Lennard Jones potential.

Table 7-3: Parameters used for the calculation of diffusion coefficient.

	Methane	Mercury	Gas mixture of Methane and Mercury
$\sigma(\text{\AA})$	3.758	2.969	3.364
ε/k	148.6	750	338.8
Ω			1.578

Chapman-Enskog theory [79] agrees with experiment at low pressures. At higher pressures, few binary data are available. A sensible empirical suggestion [83] is:

$$P \cdot D = P_0 \cdot D_0 \quad \text{Eq. 7-18}$$

in which, subscript 0 indicates values at pressure of one atmosphere and at the same temperature. The value of the diffusion coefficient in this report is adjusted to the inlet pressure of the gas and remains constant along the pipeline.

7.8. Viscosity

The method of Lee et al. [84] is a simple relation for the calculation of gas viscosity in typical natural gas mixtures with low non-hydrocarbon content.

$$\mu = K_1 \exp(X \cdot P^Y) \quad \text{Eq. 7-19}$$

where,

$$K_1 = \frac{(0.00094 + 2 \cdot 10^{-6} M_{w, gas}) T^{1.5}}{(209 + 19 M_{w, gas} + T)} \quad \text{Eq. 7-20}$$

$$X = 3.5 + \frac{986}{T} + 0.01 M_{w, gas} \quad \text{Eq. 7-21}$$

$$Y = 2.4 - 0.2X \quad \text{Eq. 7-22}$$

When using the equation of Lee et al. [84], emphasis shall be given to the units of each parameter as μ is expressed in cP, ρ in g/cm³, P in psia and T in °R.

7.9. Calculation of Activation Energy of Desorption and Pre-exponential Factor

Although the idealised nature of Jones & Perry [16] experiments is unable to simulate the complexity of the adsorption and desorption process inside an industrial gas pipeline, it constitutes the only available literature reference with adsorption isotherm data for mercury on iron. Jones & Perry [16] found that the activation energy for desorption is a function of surface coverage due to the repulsive adsorbate-adsorbate interactions which exist between mercury atoms. They also found that the value of the activation energy changes depending on the value of the pre-exponential factor used. In detail, at zero surface coverage, using the Quasi Chemical Approximation, the variation of desorption activation energy with pre-exponential factor is presented in Table 7-4.

Table 7-4: Variation of E_0 with ν using the quasi-chemical approach [16].

ν (s ⁻¹)	E_0 (kJ/mol)
1E+13	118
1E+14	126
1E+15	134
1E+16	142
1E+17	151

The surface coverage for a range of pressures is presented in the equilibrium adsorption isotherm plot (Figure 7-3). The adsorption isotherm chosen is 322.5 K, as its data is the most readily extracted and close to the operational temperature of the pipe. The results produced are summarised in Table 7-5.

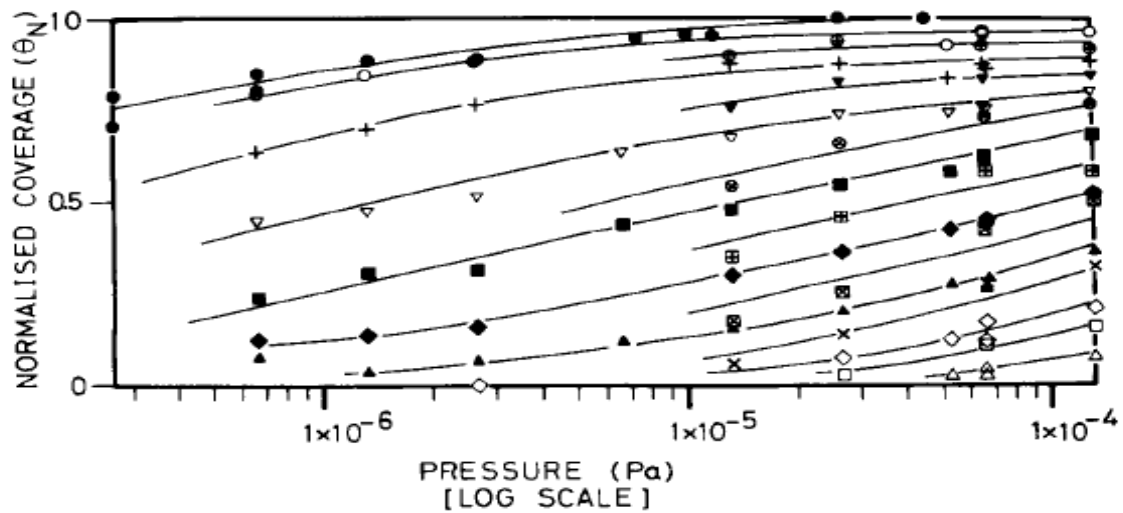


Figure 7-3: Equilibrium adsorption isotherms for Hg on Fe(100) at various temperatures [16]. The temperatures are \bullet 309.2K (room temp), \circ 322.5 K, \oplus 334.5 K, $+$ 346.7 K, ∇ 358.7 K, ∇ 370.7 K, \otimes 383.0 K, \blacklozenge 419.6 K, \blacksquare 395.0 K, \boxplus 407.2 K, \boxtimes 432.0 K, \times 457.0 K, \blacktriangle 444.5 K, \diamond 469.7 K, \square 482.0 K, \triangle 494.5 K.

Table 7-5: Variation of surface coverage with pressure at 322.5 K [16].

P (Pa)	θ (-)
6.70E-07	0.780
1.33E-06	0.825
2.70E-06	0.870
6.70E-06	0.920
1.33E-05	0.950
2.70E-05	0.960
6.70E-05	0.970
1.33E-04	0.980

To calculate the activation energy as a function of surface coverage, Eq. 5-4 was used to determine the rate of adsorption. At equilibrium, the rate of adsorption is equal to the rate of desorption.

Table 7-6: Rate of adsorption for varying values of surface coverage, equal to the rate of desorption at equilibrium.

θ (-)	Rate of adsorption=Rate of desorption (1/s)
0.780	1.258E-04
0.825	1.986E-04
0.870	2.995E-04
0.920	4.574E-04
0.950	5.674E-04
0.960	9.215E-04
0.970	1.715E-03
0.980	2.270E-03

From Table 7-5 and Eq. 2-13, the following values for the activation energy of desorption are calculated for the varying values of the pre-exponential factor.

Table 7-7: Activation energy of desorption as a function of surface coverage and pre-exponential factor.

$E_{\alpha,des}$ (J/mol)	θ	$\nu=1.00E+13 s^{-1}$	$\nu=1.00E+14 s^{-1}$	$\nu=1.00E+15 s^{-1}$	$\nu=1.00E+16 s^{-1}$	$\nu=1.00E+17 s^{-1}$
	0		1.180E+05	1.260E+05	1.340E+05	1.420E+05
0.780		1.037E+05	1.099E+05	1.160E+05	1.222E+05	1.284E+05
0.825		1.026E+05	1.088E+05	1.155E+05	1.211E+05	1.273E+05
0.870		1.016E+05	1.078E+05	1.140E+05	1.202E+05	1.263E+05
0.920		1.007E+05	1.068E+05	1.130E+05	1.192E+05	1.254E+05
0.950		1.002E+05	1.063E+05	1.125E+05	1.187E+05	1.249E+05
0.960		9.890E+04	1.051E+05	1.112E+05	1.174E+05	1.236E+05
0.970		9.726E+04	1.034E+05	1.096E+05	1.158E+05	1.220E+05
0.980		9.654E+04	1.027E+05	1.089E+05	1.151E+05	1.212E+05

The correlation between the pair $E_{\alpha,des}-\nu$ and θ is presented in Figure 7-4. In each of the presented cases, the intercept with the y-axis is set to the initial desorption activation energy for zero coverage. The graph with the R^2 closest to 1, which accounts for the best fit, is the one of $E_0=151$ kJ/mol και $\nu=10^{17} s^{-1}$.

Based on that, the dependency of $E_{\alpha,des}$ on surface coverage is expressed by Eq. 7-23 and it can be substituted in Eq. 2-13.

$$E_{\alpha,des} = -28820 \cdot \theta + 151000 \text{ (J/mol)} \quad \text{Eq. 7-23}$$

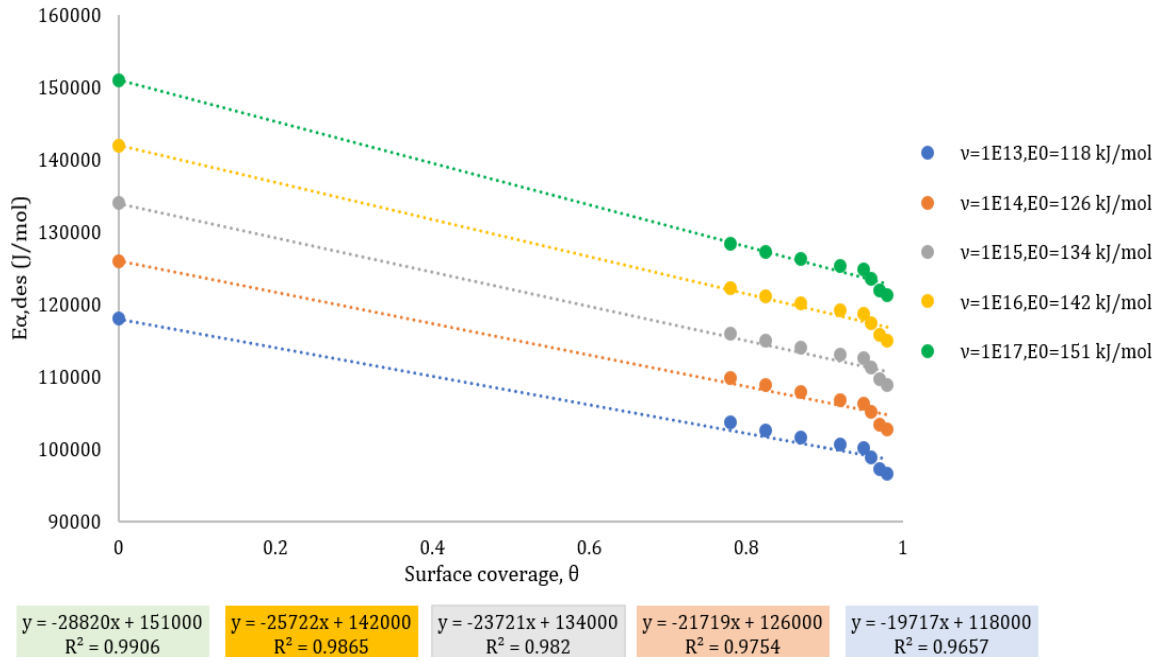


Figure 7-4: Activation energy of desorption vs surface coverage with varying pairs of v and E_0 .

7.10. Adsorption Capacity and Specific Surface Area of the Pipe

To calculate the Specific Surface Area per 1 m² of internal pipe area, Eq. 7-24 to 7-27 are employed, which express the correlation between the SSA, the adsorption capacity and the mercury monolayer mass adsorbed onto the surface of the pipe. It is underlined that diffusion into the steel surface is not dealt within the model. The pipe wall scales are accounted for by adjusting the Specific Surface Area available for adsorption to match the mercury loading factor of the steel surface. Taking into account that for full coverage of the surface, there is one atom of mercury per four-fold site of iron atoms [16], *surface atoms of mercury* are calculated as in Eq. 7-24.

$$atoms_{(Hg)} = \frac{Unit\ area}{d_{(Hg)}^2} \quad Eq. 7-24$$

Expressing *surface atoms* in terms of *surface moles*,

$$moles_{(Hg)} = \frac{atoms_{(Hg)}}{N_A} \quad Eq. 7-25$$

Transforming mercury moles to *mercury monolayer mass*,

$$monolayer\ mass_{(Hg)} = moles_{(Hg)} \cdot M_w_{(Hg)} \quad Eq. 7-26$$

For the basis of 1 m² of internal surface area, using *pipeline adsorption capacity* values, the SSA is given by Eq. 7-27.

$$SSA = \frac{Pipeline\ adsorption\ capacity}{monolayer\ mass_{(Hg)}} \quad Eq. 7-27$$

8. RESULTS & DISCUSSION

8.1. Results

Breakthrough estimates for 12 different cases from the adsorption model are summarised in Table 8-1. It is reminded that in the present model, the time to breakthrough is defined as the time taken from the start of the simulation for bulk gas mercury concentration to reach the specification of 10 ng/Sm³ in the outlet of the pipe.

The cases study three different mercury inlet concentration scenarios: high, likely and low and for each case, it covers 4 different values of adsorption capacity; the smaller value of Jones & Perry [16], two moderate estimates from Wilhelm and Nelson [19] study on operational gas pipeline and a high value. It is stressed that the adsorption capacity term enters mass balances equations in the form of Specific Surface Area (SSA) and the two variables are proportional.

Table 8-1: Pipeline adsorption model results.

Case	Mercury Inlet Concentration (ng/Sm ³)	Adsorption capacity (g/m ²)	SSA(m ² /m ²)	Time to Breakthrough	
				days	years
1-0	5000	0.0038	1	1.5	-
1-1	5000	0.6	160	223.4	-
1-2	5000	1	263	367.1	1.0
1-3	5000	10	2632	3673.3	10.1
2-0	1000	0.0038	1	7.2	-
2-1	1000	0.6	160	1141.8	3.1
2-2	1000	1	263	1876.8	5.1
2-3	1000	10	2632	18781.9	51.5
3-0	100	0.0038	1	73.6	-
3-1	100	0.6	160	11759.1	32.2
3-2	100	1	263	19329.0	53.0
3-3	100	10	2632	193436.3	530.0

Pipeline outlet concentration profiles with time are shown for two different mercury inlet concentrations in Figures 8-1 to 8-4. For each case study, there are two figures for different SSA values. Moreover, for the same SSA value, the pipeline outlet concentration is depicted for two different mercury inlet concentrations in Figures 8-4 and 8-5. Surface coverage along the pipeline is, also, depicted at breakthrough time for different SSA values in Figure 8-6 and 8-7.

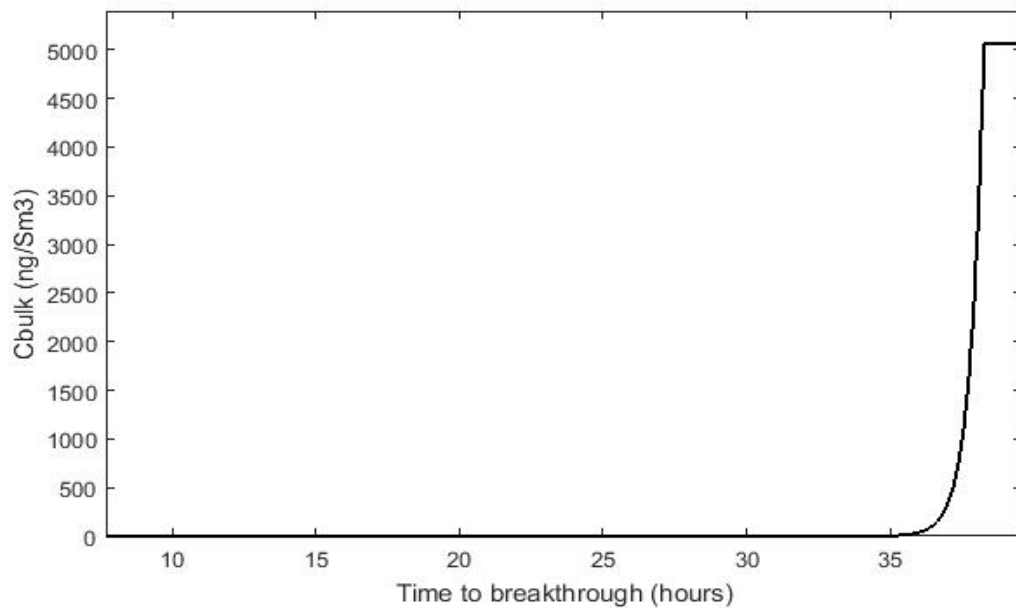


Figure 8-1: Mercury outlet concentration vs time for Case 1-0.

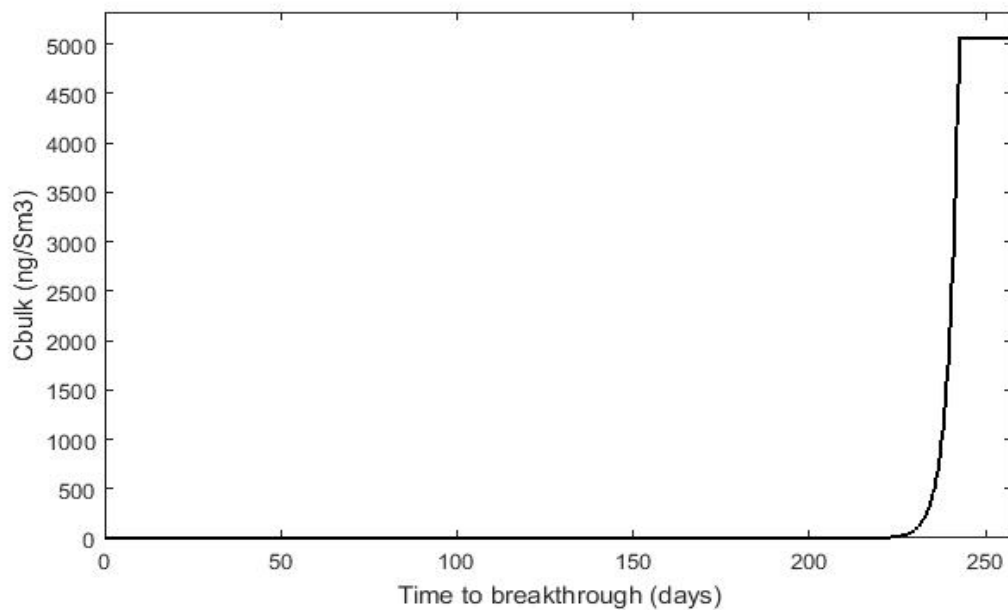


Figure 8-2: Mercury outlet concentration vs time for Case 1-1.

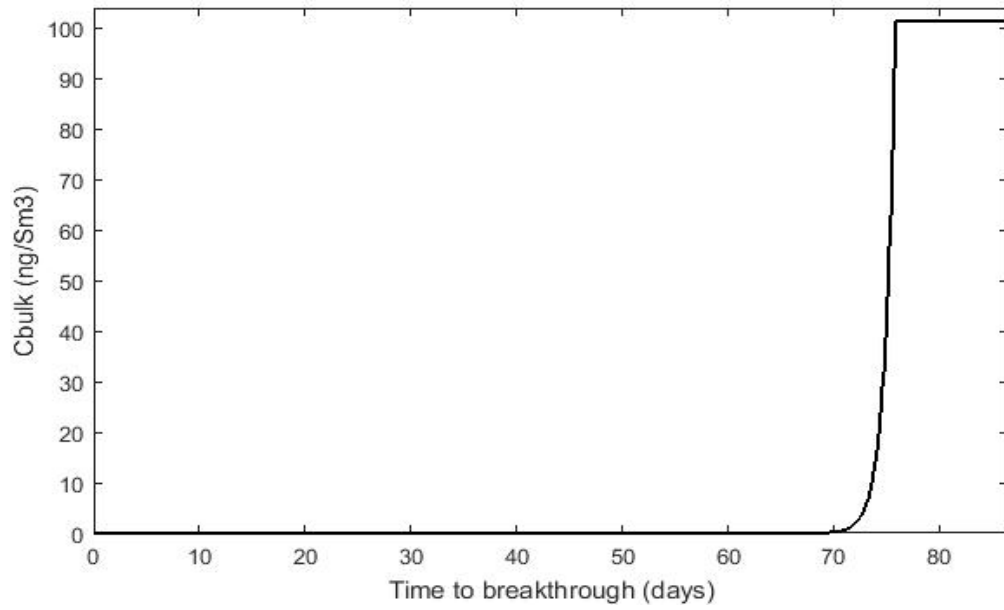


Figure 8-3: Mercury outlet concentration vs time for Case 3-0.

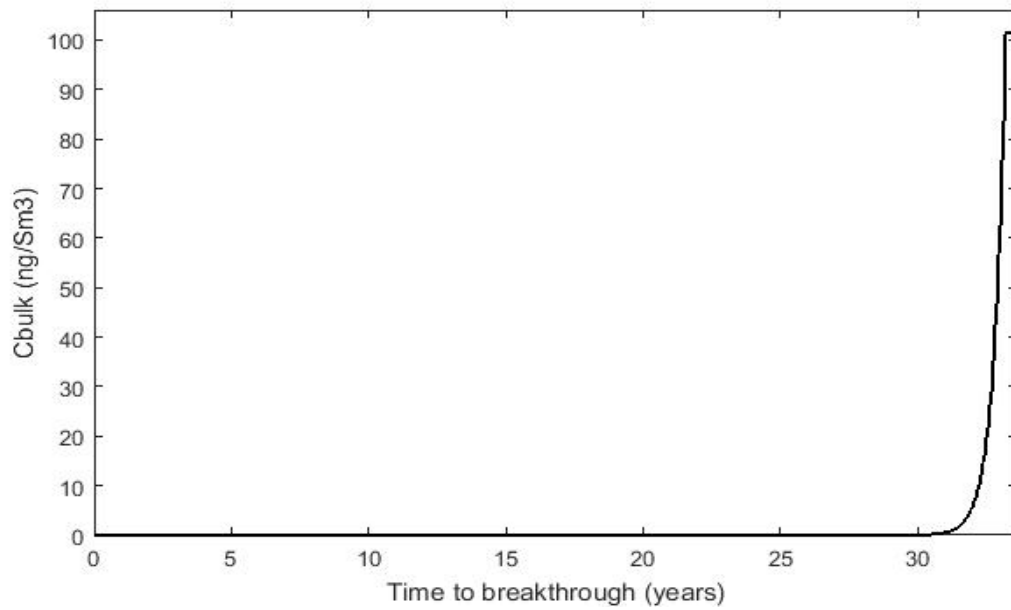


Figure 8-4: Mercury outlet concentration vs time for Case 3-1.

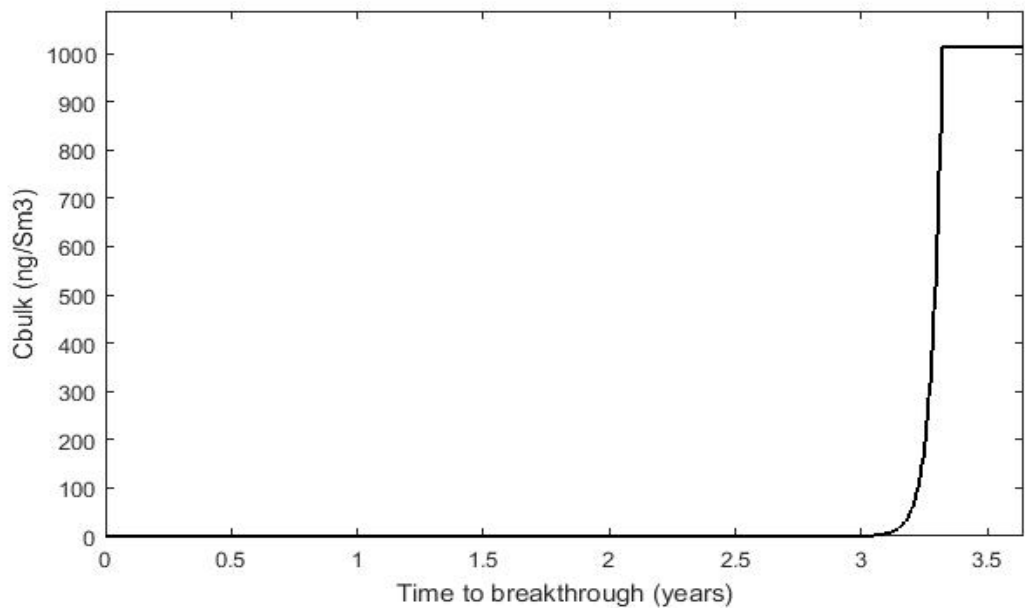


Figure 8-5: Mercury outlet concentration vs time for Case 2-1.

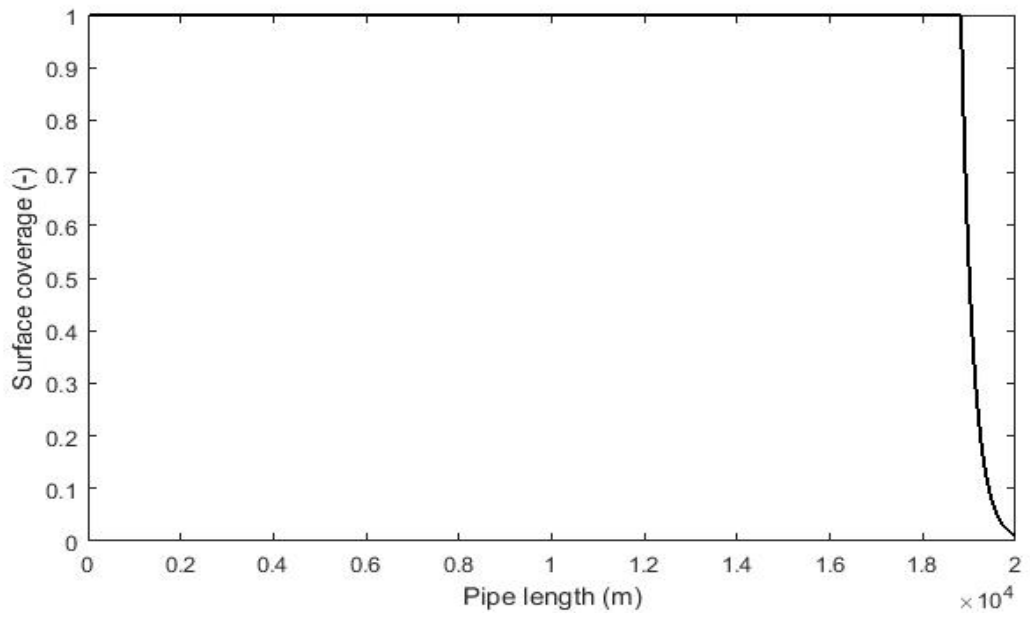


Figure 8-6: Length of Mercury Adsorption Front for Case 2-1.

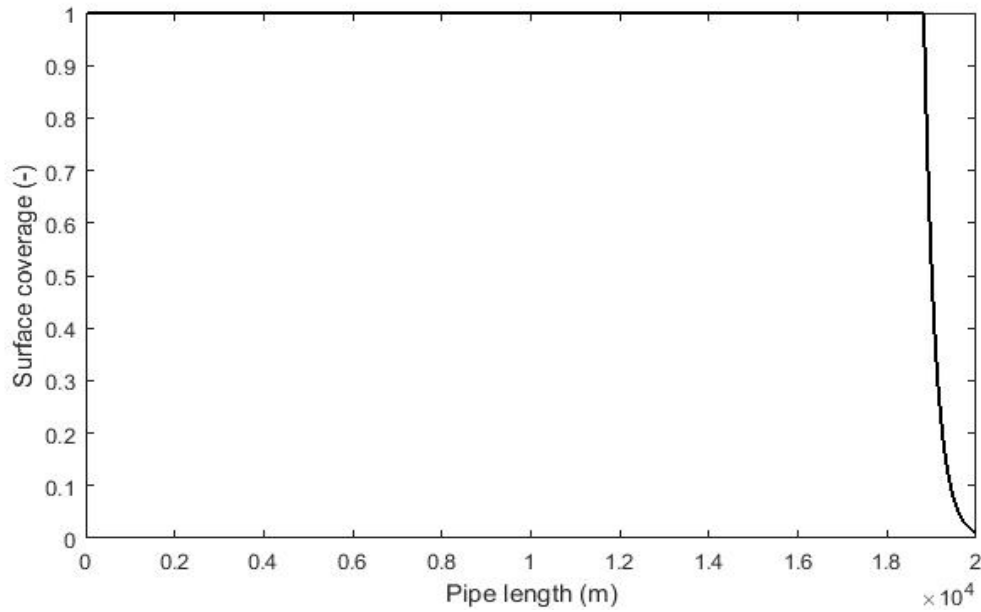


Figure 8-7: Length of Mercury Adsorption Front for Case 2-2.

The results reveal the following main trends:

- a. Prior to breakthrough, there is zero mercury detected at the exit of the pipe.
- b. An increase in the mercury inlet concentration leads to a decrease, as expected, in the breakthrough time for the same adsorption capacity, or equivalently for the same SSA. The breakthrough time is almost inversely proportional to the mercury inlet concentration.
- c. The breakthrough time varies almost proportional to the adsorption capacity or equivalently to the SSA for the same mercury inlet concentration.
- d. The value of SSA does not affect the adsorption profile.
- e. By joining observations b and c, a very successful correlation (Eq. 8-1) of the breakthrough time with the Specific Surface Area of the pipe and the mercury inlet concentration is extracted. The results of the Eq. 8-1 are graphically depicted in Figure 8-8.

$$Breakthrough\ time\ (days) = 7153.08 * \frac{SSA\ (\frac{m^2}{m^2})}{Mercury\ Inlet\ Concentration\ (\frac{ng}{Sm^3})} + 0.08 \quad Eq. 8-1$$

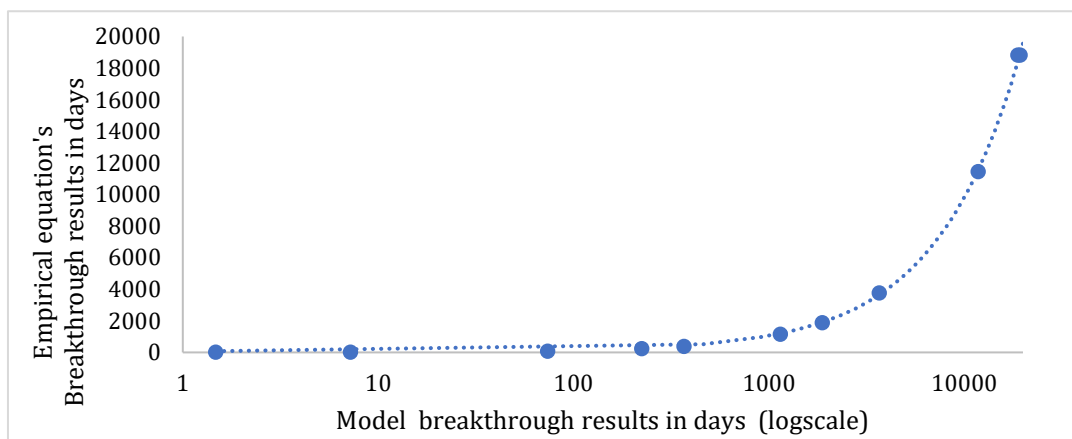


Figure 8-8: Breakthrough time estimated by the model vs the corresponding time estimated by Equation 8-1.

Furthermore, for an already operating gas pipe, it is of great interest to examine the level of pipe wall saturation to moderately predict the time for mercury breakthrough. The mercury adsorption profile is plotted in Figure 8-9 as the fractional surface coverage (θ) against number of segments for Case 2-2 (Mercury Inlet Concentration=1000 ng/Sm³, SSA = 263 m²/m²), for four different times (note that for this case, the breakthrough time is 5.1 years).

It is observed that close to breakthrough time, the greatest part of the pipe surface is covered. Moreover, the mercury adsorption front appears rather steep.

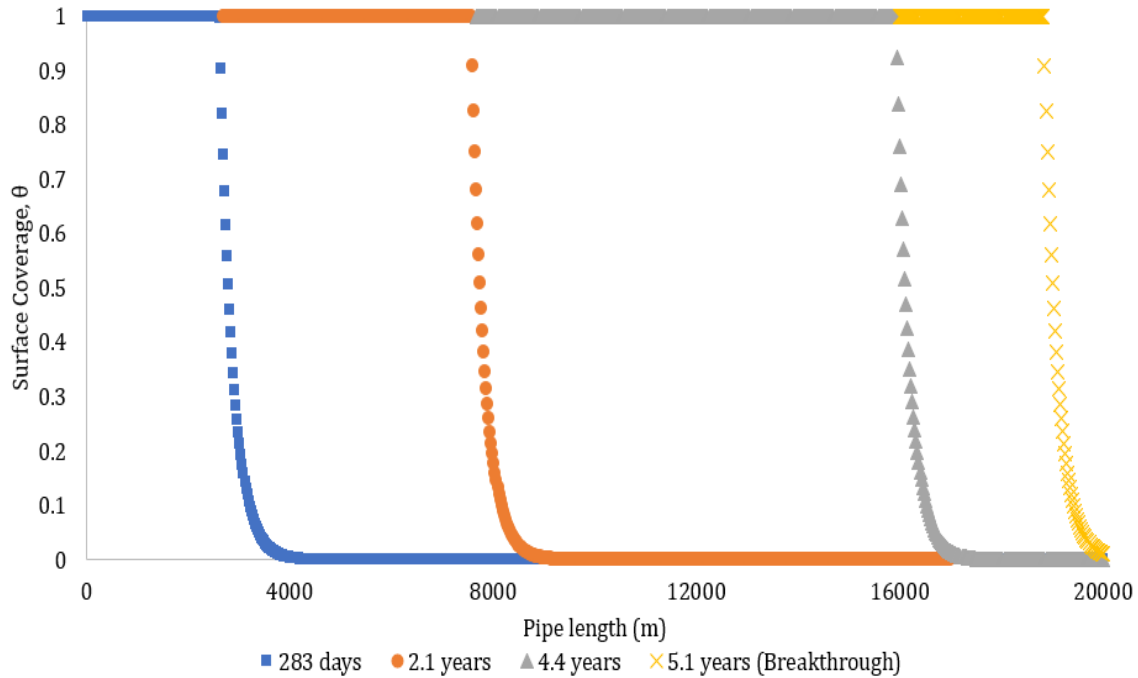


Figure 8-9: Length of mercury adsorption front for Case 2-2.

8.2. Sensitivity Analysis

Parametric sensitivity analysis is a systematic approach to analyse dynamics of mercury adsorption in natural gas pipelines and to simulate and predict how sensitive the observed system appears to be in possible changes. Seeking to ensure robustness of the model's results and increase understanding of the relationships between input and output variables, the identification of uncertain parameters is accomplished and their effect on the model's time to breakthrough and surface coverage is investigated.

In the preliminary stages, a subscript that acts as an extension of the MATLAB solver `odes15s`, is implemented. Through this, it is feasible to calculate derivatives of the model variables, C_{bulk} , $C_{stagnant}$ and θ , dependent on parameters that display uncertainty, and determine those that contribute significantly to successful model development. In this work, the main parameters tested are the mass transfer coefficient, k_m that determines the rate of mercury mass transfer from the bulk gas phase to the pipe wall and vice-versa, the fugacity coefficient of mercury, φ^{Hg} and the compressibility factor, Z , both of which are directly calculated from the thermodynamic model in use and are, respectively, introduced in the surface coverage equation. Figure 8-10 and 8-11, the effect of the main parameters on mercury bulk concentration at the inlet of the pipe, and surface coverage at its outlet, is demonstrated, respectively, for Case 1-0. The change in derivatives is rather obvious during segment saturation. The mass transfer coefficient, k_m , appears to have,

undoubtedly, the greatest impact on the mercury adsorption process. Despite the ostensibly minor sensitivity of the solution referring to $\varphi^{v_{Hg}}$ and Z , a thorough analysis reveals their real influence, as described in Sections 8.2.2 and 8.2.3.

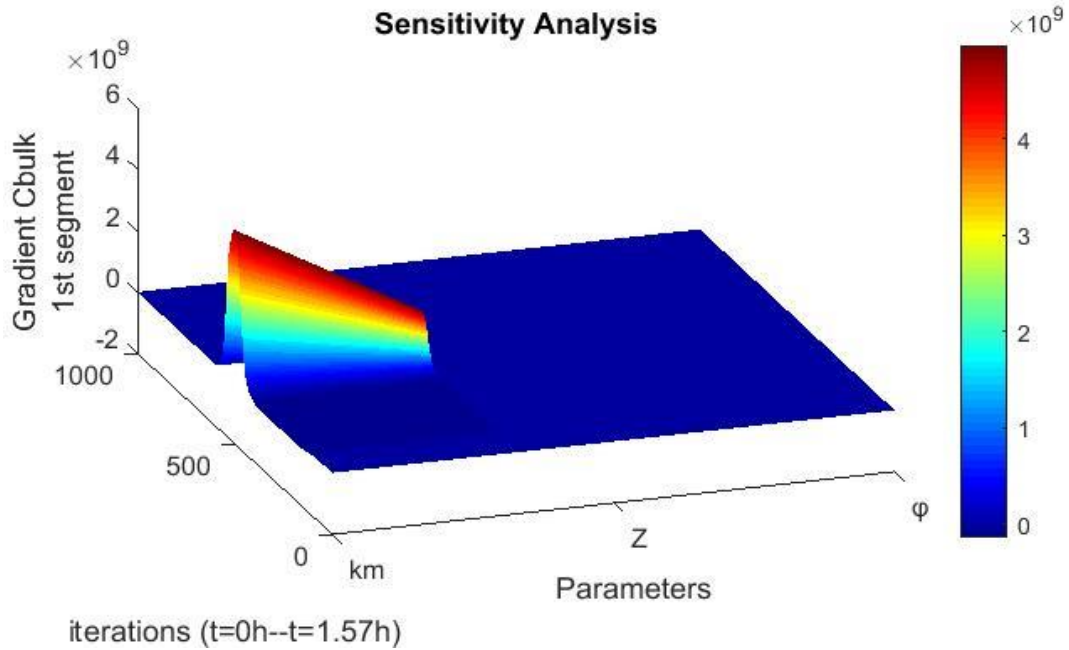


Figure 8-10: Derivates of bulk gas mercury concentration for the first segment dependent on the model parameters k_m , Z and $\varphi^{v_{Hg}}$ for Case 1-0.

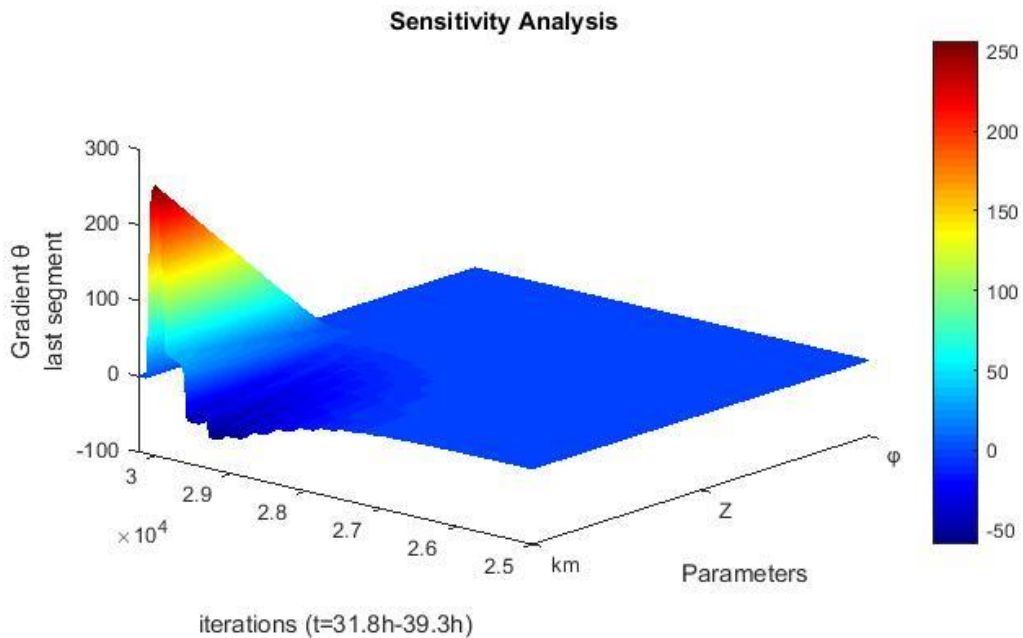


Figure 8-11 Derivates of surface coverage for the last segment dependent on the model parameters k_m , Z and $\varphi^{v_{Hg}}$ for Case 1-0.

8.2.1. Effect of Mass Transfer Coefficient

The gas phase mass transfer coefficient, k_m , for mercury diffusion through the stagnant boundary layer is calculated as described in Section 7.4. The model's sensitivity to k_m is shown in Figure 8-12 and 8-13. It appears that the length and shape of the mercury adsorption profile is determined by the gas phase mass transfer coefficient and therefore by the rate of mass transfer. A slight decrease in the mass transfer coefficient contributes to lower rates of mass transfer and hence, causes more prolonged, yet, shallower adsorption fronts and a sharp decline in mercury breakthrough time, as diffusion becomes the rate-limiting step of the process. On the contrary, by increasing the value of k_m , breakthrough time is not significantly affected, although the adsorption profile appears rather steep.

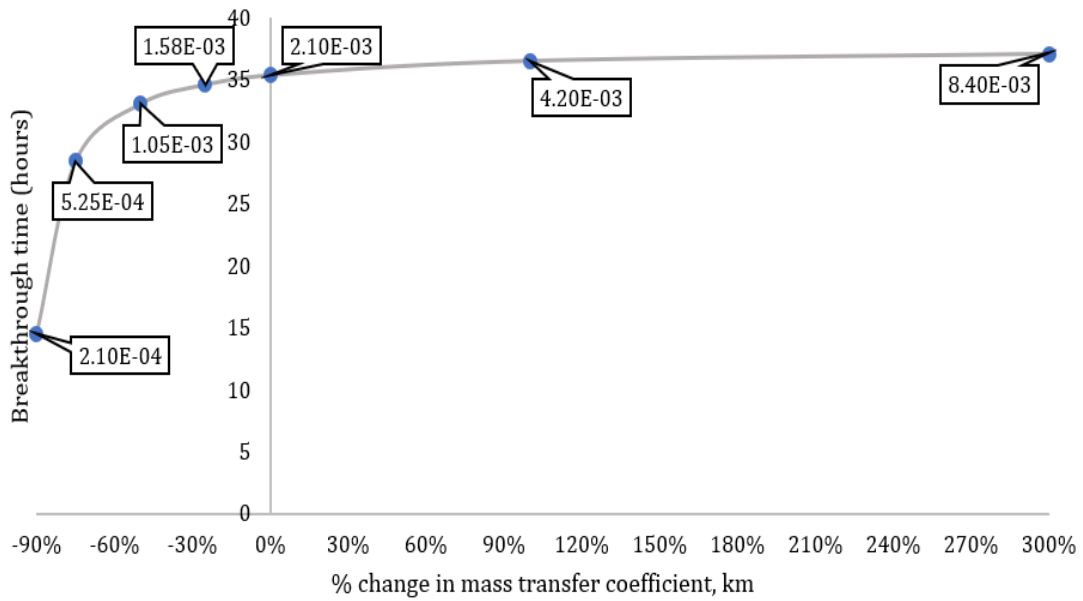


Figure 8-12: Effect of mass transfer coefficient on breakthrough time for Case 1-0.

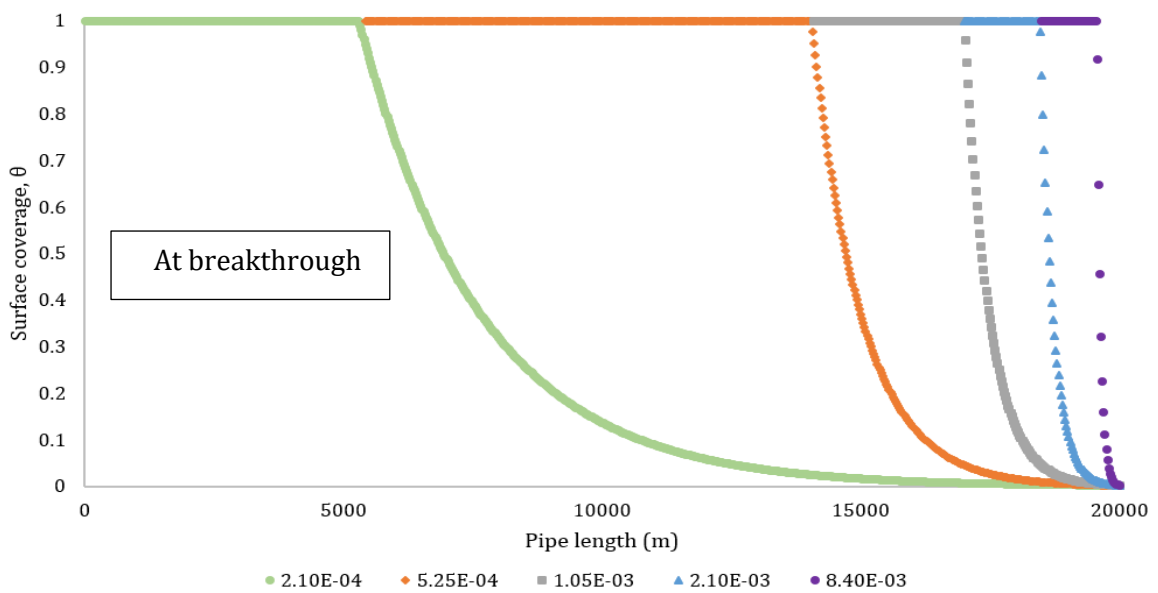


Figure 8-13: Effect of mass transfer coefficient on mercury adsorption front for Case 1-0 at breakthrough.

This observation indicates the sensitivity of the model in the calculation of mass transfer coefficient as underestimating k_m results in an early breakthrough time. In all cases, k_m is dependent on viscosity, density and diffusion coefficient and it is, therefore, the value with the highest uncertainty. An accurate estimate of k_m is a prerequisite for successful model development.

8.2.2. Effect of Compressibility Factor

A change of $\pm 10\%$ in compressibility factor, Z , is tested and the impact on surface coverage and breakthrough time are shown below for the Case 1-0 (Figure 8-14 & Table 8-2). The standard value of Z is 0.6074, calculated by UMR-PRU model [25].

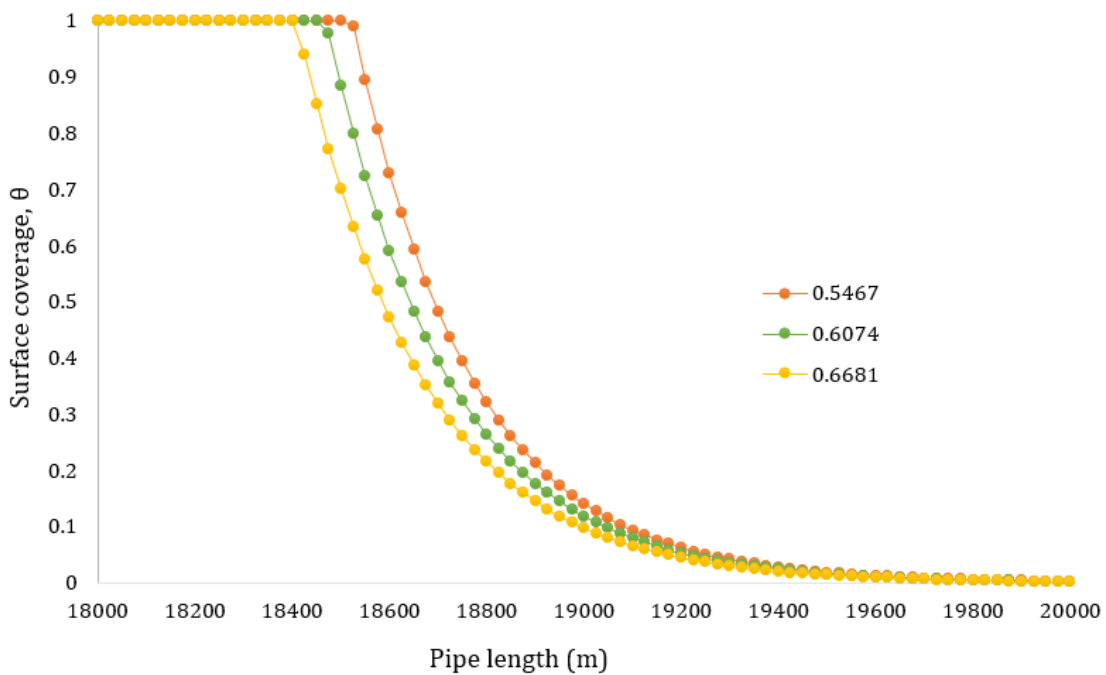


Figure 8-14: The effect of compressibility factor on surface coverage at breakthrough for Case 1-0.

Table 8-2: The effect of compressibility factor on breakthrough time for varying Z .

Compressibility factor, Z	Breakthrough time (hours)
0.5467	39.4
0.6074	35.4
0.6681	32.0

It is observed that the adsorption front is offset to a higher number of saturated sections, when Z is decreased. An increase in the overall surface coverage causes an expected increase in mercury breakthrough time. However, it shall be noted that an increase in the compressibility factor results in a rather prolonged adsorption front. For n saturated segments, the higher the Z value, the less gradual the decrease in the coverage of the next segments, compared to the standard case. Due to fine gridding, this effect cannot be easily perceived by studying Figure 8-14. For this purpose, the values of $(n+1)$ and $(n+2)$ unsaturated segments are reported in Table 8-3.

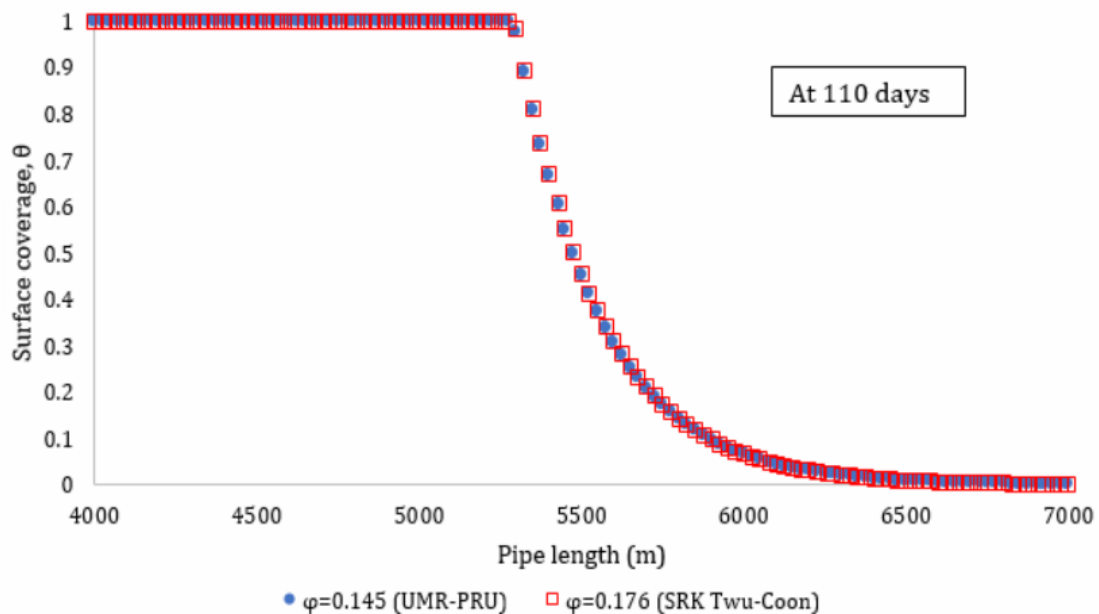
Table 8-3: The effect of varying Z on the steepness of adsorption front at breakthrough time.

$\theta(-)$ at breakthrough			
Compressibility factor, Z	0.5467	0.6074	0.6681
Last saturated segment, n	1.000	1.000	1.000
$n+1$ segment	0.989	0.976	0.940
$n+2$ segment	0.894	0.884	0.852

8.2.3. Effect of Fugacity Coefficient

The fugacity coefficient, which is considered constant along the pipe, constitutes part of the mathematical formulation of surface coverage and it is possible to influence the adsorption-desorption kinetics. It is evident that a small fugacity coefficient of mercury is indicative of strong affinity with the natural gas mixture. Taking this into consideration, the use of a fugacity coefficient for ideal gas behaviour of mercury in the gas mixture would be absurd.

In Figure 8-15, it is shown the effect of mercury fugacity coefficient on the adsorption front for Case 1-2 at 110 days. A new value of $\varphi^{v_{(Hg)}}$ tested is calculated using SRK Twu-Coon [85]. It appears that the model is insensitive to small changes in fugacity coefficient as the calculated time for mercury breakthrough, in each case, is 367.1 days and the adsorption fronts are identical.

Figure 8-15: Adsorption front at 110 days for varying fugacity coefficient, $\varphi^{v_{Hg}}$, for Case 1-2.

8.2.4. Effect of the Stagnant Boundary Layer Thickness

During model development, it was assumed that the thickness of the stagnant boundary layer is half of the thickness of the concentration boundary layer [20] and since δ is introduced in the system of ODEs by defining the respective control volume, it can be considered a parameter whose value needs further examination on model results. For this reason, several approaches shall be tested.

The first two approaches focus on flow above a semi-infinite plate. Since, the Schmidt number is close to unity, the momentum boundary layer thickness can be assumed equal to the concentration boundary layer [80].

$$\delta = \delta_c \quad \text{Eq. 8-2}$$

Empirically extending the solution for laminar velocity profile in the boundary layer above a semi-infinite plate to include fluids with Pr E. Polhausen [86] found that for Prandtl and Schmidt number greater than 0.6, the relation between δ and δ_c can be described by Eq. 8-3.

$$\frac{\delta}{\delta_c} = Sc^{1/3} \quad \text{Eq. 8-3}$$

To include all possible scenarios, the last two approaches assume that the thickness of the wall region, δ , is equal to one third and double, respectively, of the concentration boundary layer.

$$\delta = \frac{1}{3} \delta_c \quad \text{Eq. 8-4}$$

$$\delta = 2\delta_c \quad \text{Eq. 8-5}$$

In Figure 8-16, the results of the change in the stagnant boundary layer on mercury adsorption front and breakthrough time are depicted for the lower and the higher value tested. The same trend applies for the other cases, reported in Table 8-4.

Table 8-4: Tested values of stagnant boundary layer thickness.

Stagnant boundary layer thickness, δ , as calculated by	m
[Eq.7-8]	2.13E-5
[Eq.8-2]	4.25E-5
[Eq.8-3]	4.48E-5
[Eq.8-4]	1.42E-5
[Eq.8-5]	8.51E-5

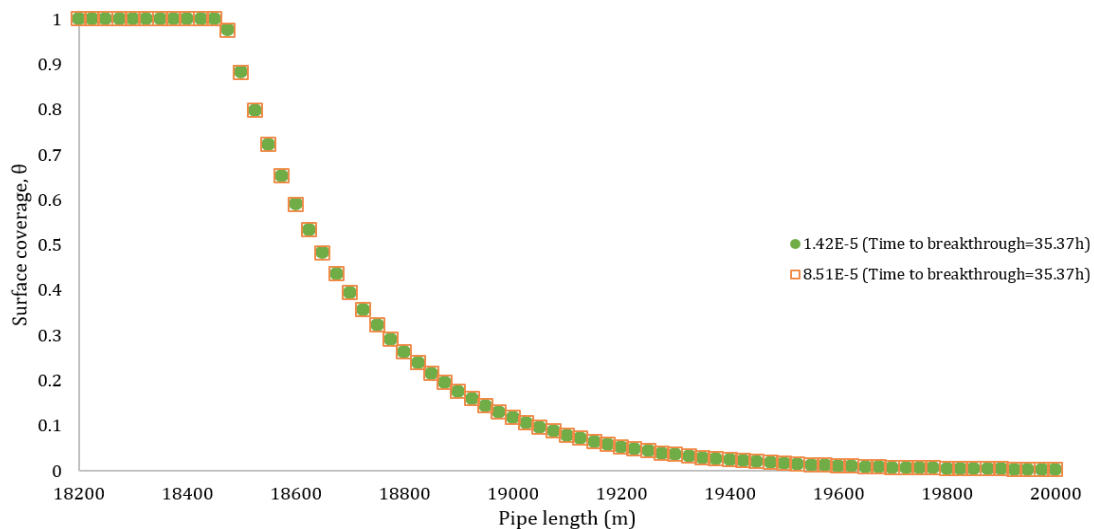


Figure 8-16: Adsorption front for varying stagnant boundary layer thickness, at breakthrough, for Case 1-0.

It can be, therefore, concluded that whichever approach is used, the time to breakthrough and mercury adsorption front are identical. This observation validates that the initial assumption for the calculation of the stagnant boundary layer does not affect model results.

8.2.5. Confirmation of the Compensation Effect

This initial desorption energy E_0 is a characteristic quantity for a given adsorption system which reflects the strength of the interaction between the adsorbed phase and the substrate [46]. Based on the results of Jones and Perry [16] on the activation energy of desorption at zero coverage paired up with the pre-exponential factor, it is investigated whether the compensation effect is demonstrated. According to Figure 8-17, the function, which best relates them, is of the exact same logarithmic form as Eq. 4-6.

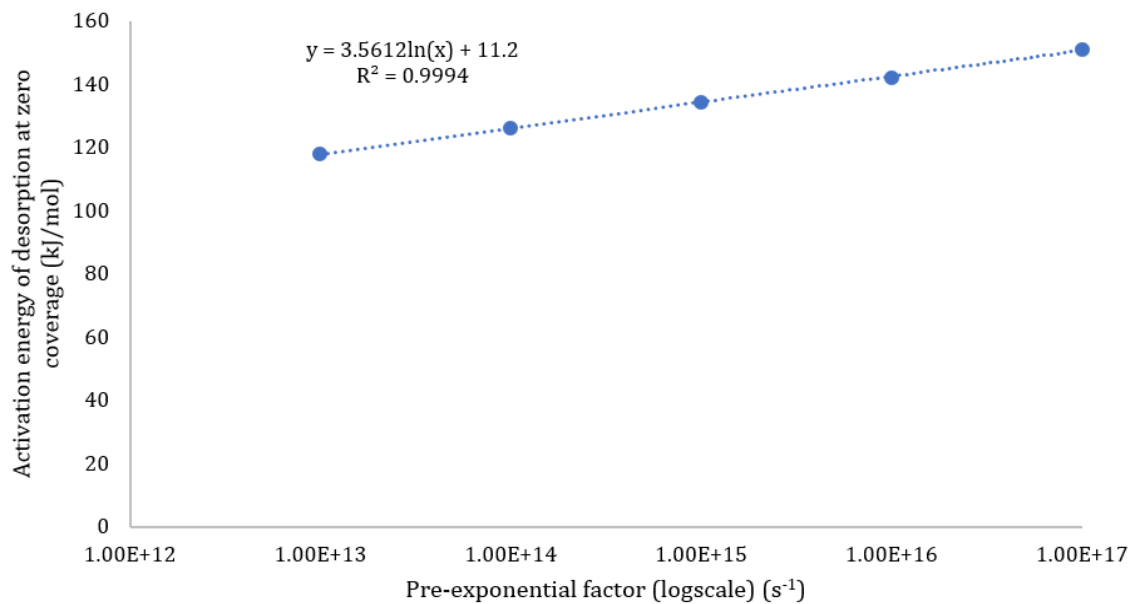


Figure 8-17: Relation between activation energy for adsorption at zero coverage and pre-exponential factor, v .

To evaluate the impact of compensation effect on breakthrough time (Table 8-5) and surface coverage of the pipe wall (Figure 8-18 and 8-19), the model runs for the higher and lower value of E_0 - v , considering the respective dependence on surface coverage, for 2 different inlet concentrations (1000 and 100 ng/ Sm^3) and SSA=160. It is apparent that the compensation effect allows to use whichever pair of E_0 - v without significant difference on either the breakthrough time or the adsorption front.

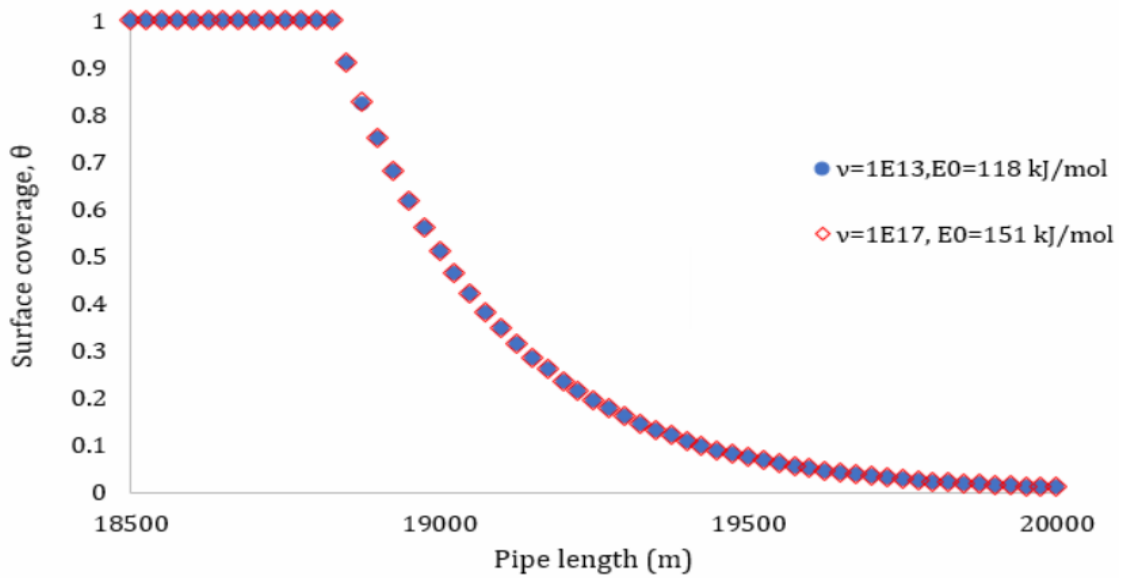


Figure 8-18: Adsorption front length at breakthrough for Case 2-1 for different pairs of E_0 - v .

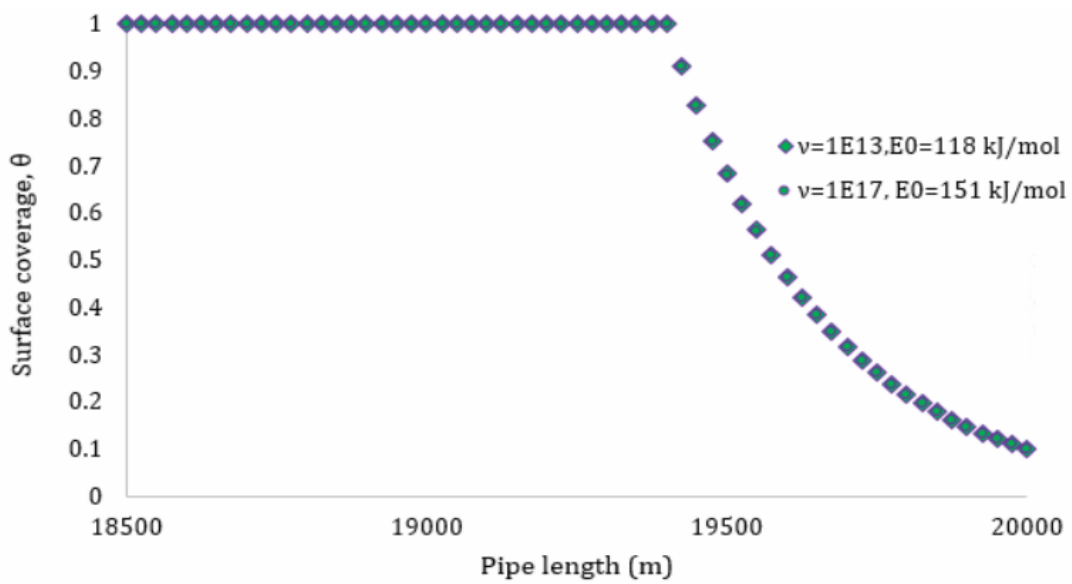


Figure 8-19: Adsorption front length at breakthrough for Case 3-1 for different pairs of E_0 - v .

Table 8-5: Compensation effect vs time to breakthrough for Cases 2-1 & 3-1.

Mercury Inlet Concentration (ng/Sm ³)	SSA(m ² /m ²)	Time to breakthrough (years) for $v=10^{13}$, $E_0=118$ kJ/mol	Time to breakthrough (years) for $v=10^{17}$, $E_0=151$ kJ/mol
1000	160	3.13	3.13
100	160	32.21	32.22

To further underline the importance of using pairs of E_0 - v , separate changes in the initial desorption activation energy and pre-exponential factor are applied for the pair used in the model ($v=10^{17} \text{ s}^{-1}$ and $E_0=151 \text{ kJ/mol}$) and their effect on results is investigated.

As far as a change in E_0 is concerned, in Figure 8-20, it is observed that the time to breakthrough is insensitive to the increase in desorption activation energy by 50%, in the examined case. On the contrary, the time to breakthrough dramatically decreases when the activation energy for desorption is halved (Table 8-6). A similar trend occurs for surface coverage, as in the case of 50% decreased E_0 , the surface coverage is close to zero (Figure 8-21). Therefore, it can be concluded that the lesser the activation energy of desorption, thus the lesser the energy barrier that mercury atoms must pass to escape into the gaseous phase, results in an extremely small percentage of mercury atoms remaining in the saturated surface, due to an increase in the desorption rate, and early breakthrough, respectively.

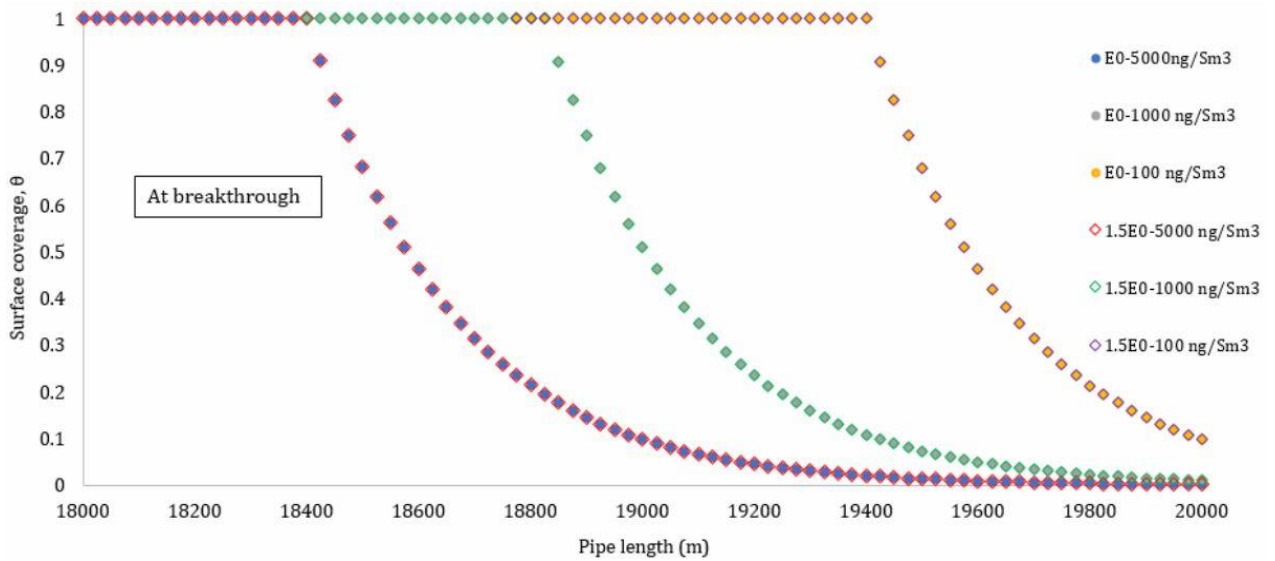


Figure 8-20: Comparison of adsorption length at breakthrough for Cases 1-1, 2-1 and 3-1 with $E_0=151 \text{ kJ/mol}$ and 302 kJ/mol .

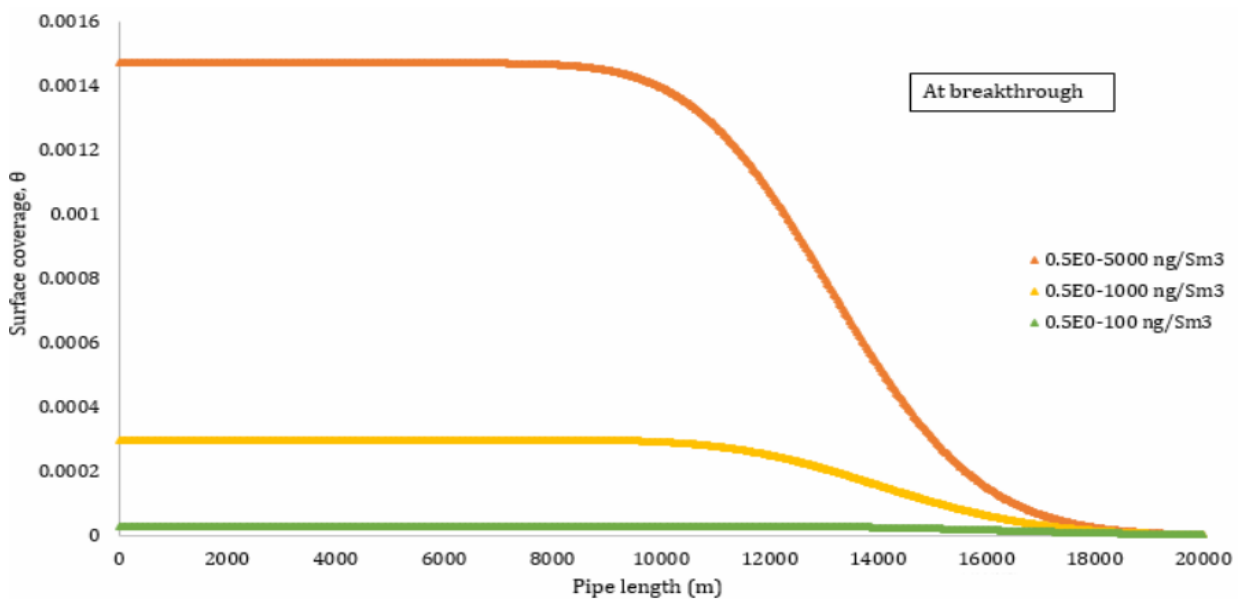


Figure 8-21: Adsorption length at breakthrough for Cases 1-1, 2-1 and 3-1 with $E_0=75.5 \text{ kJ/mol}$.

Table 8-6: Effect of E_0 on time to breakthrough.

Mercury inlet concentration (SSA=160 m ² /m ²)	Time to breakthrough (days)		
	0.5E ₀	E ₀	1.5E ₀
5000	0.3	223.4	223.4
1000	0.3	1141.8	1141.8
100	0.4	11759.1	11759.8

Regarding the pre-exponential factor (Figure 8-22 & Figure 8-23), an increase of its value leads to earlier times to breakthrough and less surface coverage. However, its effect is, unambiguously, of smaller magnitude than that of the activation energy.

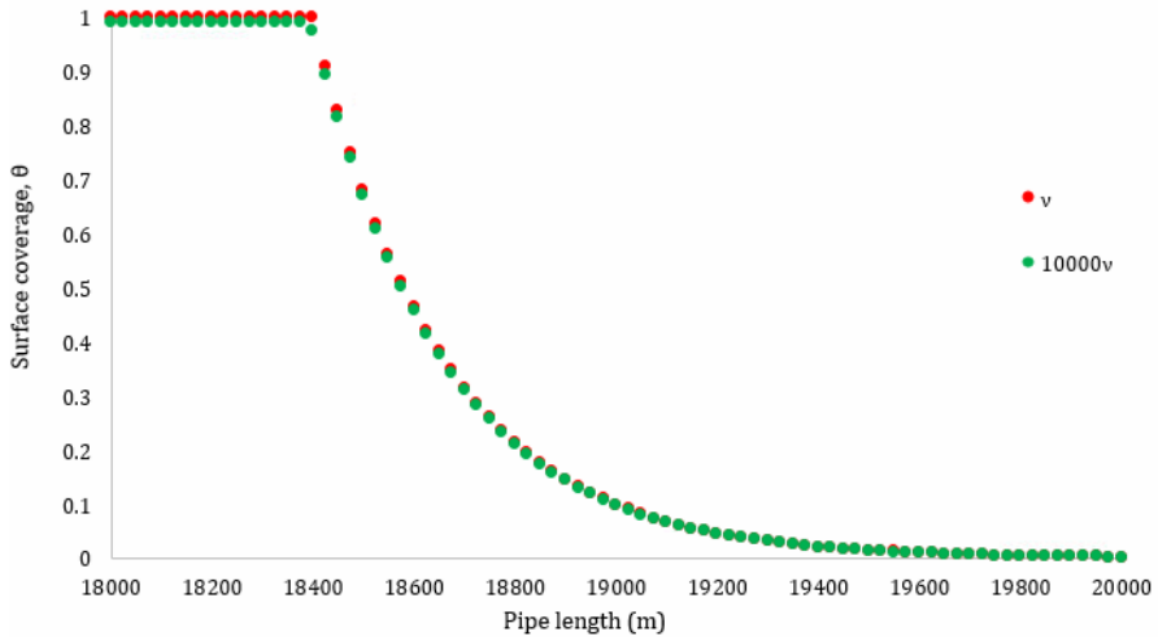


Figure 8-22: Effect of varying pre-exponential factor on maximum surface coverage for Case 1-1.

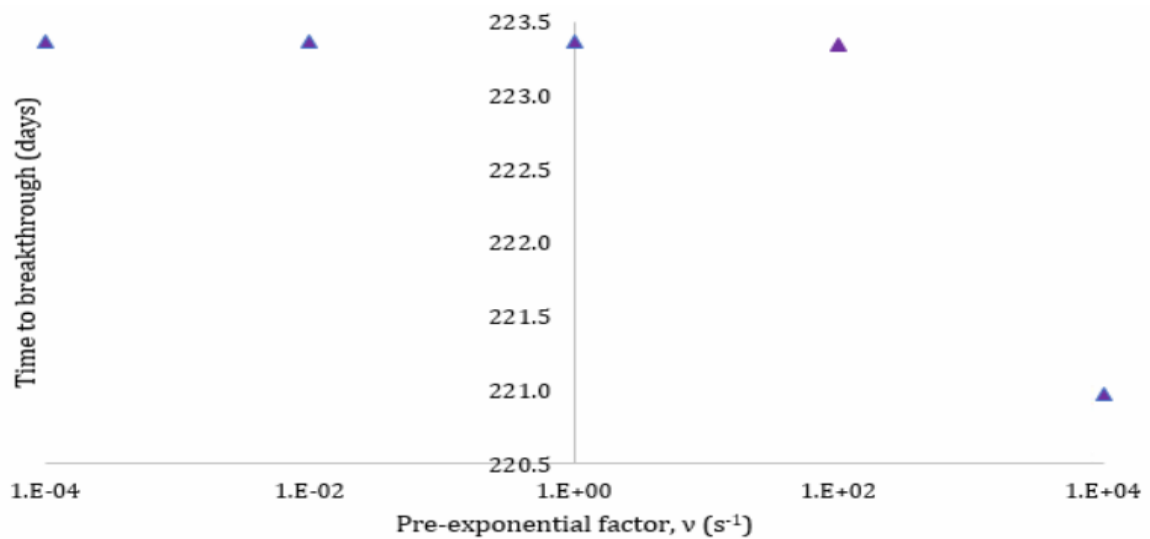


Figure 8-23: Effect of varying pre-exponential factor on breakthrough time for Case 1-1.

Based on these observations, it shall be concluded that it is imperative to investigate whether there is tentative evidence for a possible compensation effect, prior to determining desorption kinetic parameters, and select the right pair of values.

8.2.6. Curve Fitting for the Activation Energy of Desorption and Surface Coverage

Guo and Yates [59] study of CO adsorption on Pd (111) confirmed that the desorption activation energy decreases with surface coverage. In the case of mercury on iron, as described in detail in Section 3.4, a similar descending trend is noted, which can be described well by a linear function. However, due to a profound lack of experimental data below surface coverage of 0.7 and the uncertainty of linearity, it deems necessary to search for a curve that describes more precisely ($R^2 \approx 1$), the relation between the activation energy of desorption and surface coverage. Moreover, the effect of incorporating a new relationship in the model equations on breakthrough time and surface coverage is investigated. It was found that the best approximation is achieved by a second order polynomial (Eq. 8-6).

$$E_{\alpha,ads} = -3771,5 \cdot \theta^2 - 25361 \cdot \theta + 151000 \text{ (J/mol)} \quad \text{Eq. 8-6}$$

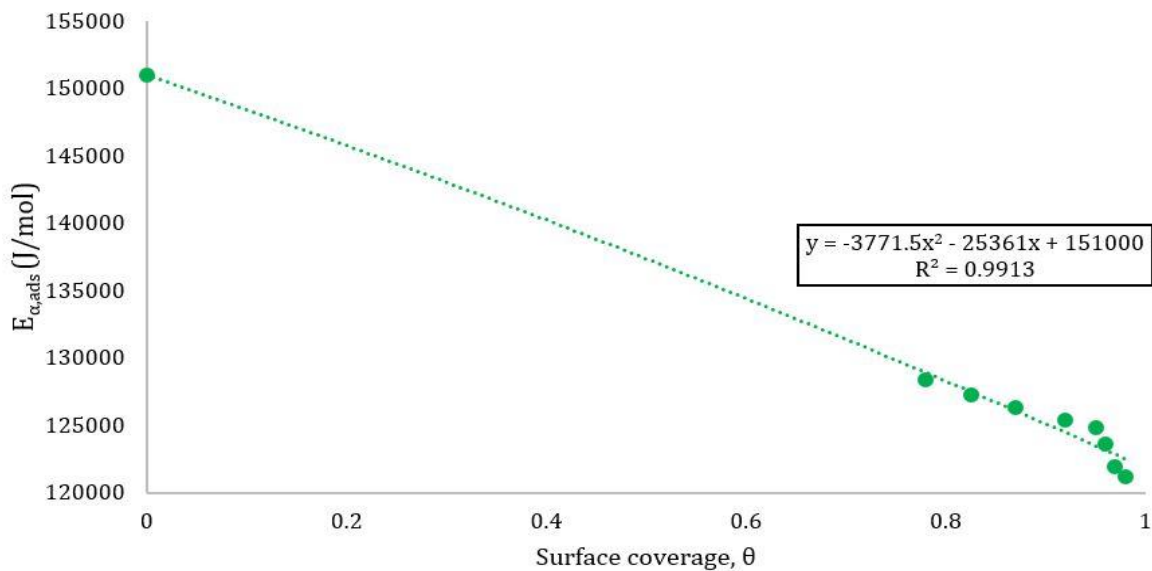


Figure 8-24: Best fit for activation energy of desorption vs surface coverage.

Based on the results of Table 8-7 and Figure 8-25, it is apparent that even the best fit curve has negligible effect on breakthrough time and surface coverage.

Table 8-7: Effect of best fit curve of $E_{\alpha,des}-\theta$ on breakthrough time and comparison with the linear function used in the model.

Mercury Inlet Concentration (ng/Sm ³)	SSA(m ² /m ²)	$E_{\alpha,des} = -3771,5 \cdot \theta^2 - 25361 \cdot \theta + 151000$ (J/mol)	$E_{\alpha,des} = 151000 - 28820 \cdot \theta$ (J/mol)
		Breakthrough (years)	
5000	160	0.61	0.61
1000	160	3.13	3.13
100	160	32.22	32.22

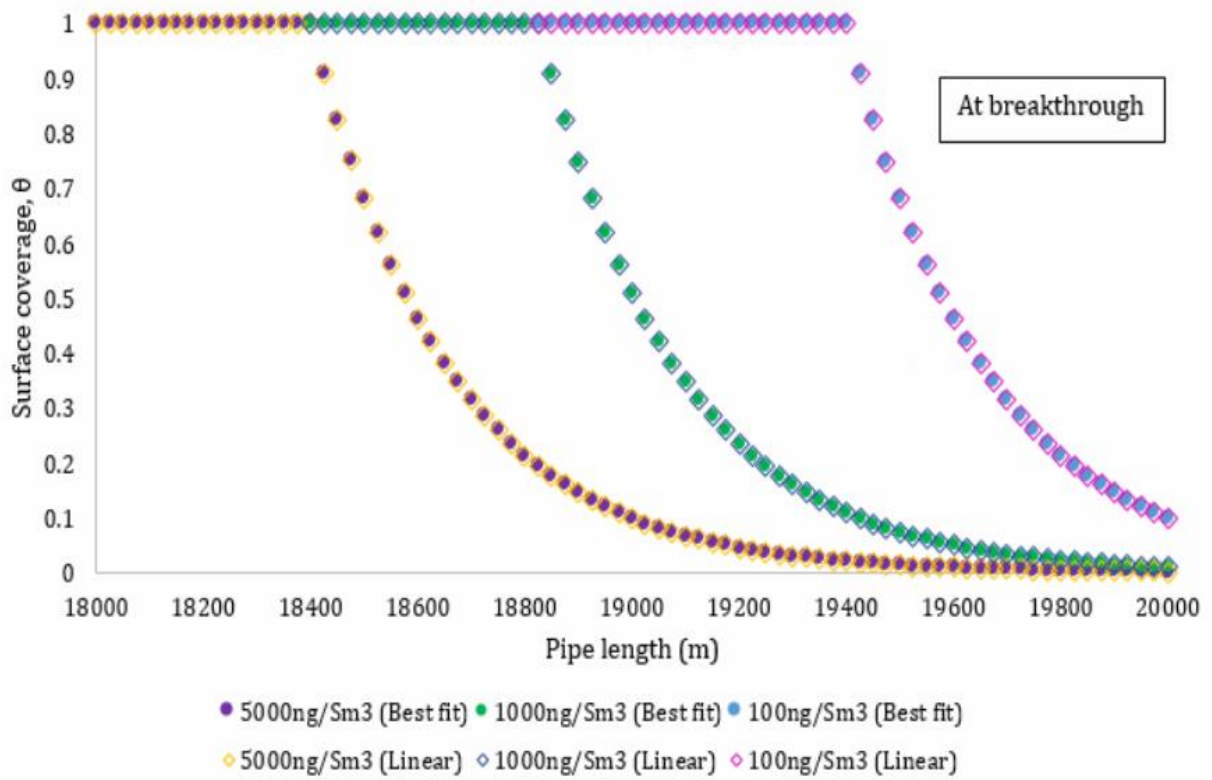


Figure 8-25: Comparison of adsorption profile for 2nd order polynomial and linear function of $E_a, des-\theta$ for Cases 1-1, 2-1 and 3-1 at breakthrough.

9. MODEL IMPLEMENTATION IN ASPEN CUSTOM MODELER

9.1. Aspen Custom Modeler

Aspen Custom Modeler (ACM) constitutes a core element of ASPEN Tech's AspenONE® Engineering applications [27]. It is an easy-to-use tool for creating, editing and re-using models of process units. It allows performing dynamic and steady-state simulations, while, also, supports parameter estimation and optimization. ACM uses an object-oriented modelling language, editors for icons and tasks, and Microsoft Visual Basic for scripts. Its readily customisable nature and extensive automation features render it ideal for combination with other products, such as Microsoft Excel and Visual Basic. This allows the user to build complete applications for non-experts to use [87].

9.2. ACM Model Development

In ACM, each variable and parameter are to be, first, declared in the model script, prior to compiling the model. Variables are registered as fixed, free, initial. Fixed variables are those whose value is known and fixed, free are those whose value is being solved for and initial variables include variables known and fixed at time zero for an initialisation or dynamic run. The mercury concentration in the bulk gas, C_{bulk} , the concentration in the stagnant boundary layer, $C_{stagnant}$, and surface coverage, θ , which are calculated by integrating the system of ODEs (Eq.5-2, 5-3 & 5-7), are registered as initial variables. In this way, the initial conditions are set.

The system of ODEs is solved numerically in ACM using the "Method of Lines" approach, where time is a continuous variable and distance along the pipeline is treated as a discrete variable. The pipeline length is effectively being discretised and is described by a set of finite difference equations, which are integrated over time by using either Implicit Euler or the Runge-Kutta methods [29]. The time step is internally selected and may vary to ensure convergence.

As the model requires a number of physical properties to be calculated that depend on time and distance, ACM allows procedural calls to be made to the Aspen Physical Properties Engine to calculate these parameters and hence, the solving process is simplified. Namely, density of the mixture and mercury fugacity coefficient are calculated internally, using the thermodynamic model Peng Robinson [28] with zero binary interaction parameters, as well as the molecular weight of the natural gas.

The implementation of the model in ACM is rather advantageous compared to the model in MATLAB, as ACM offers a user-friendly interface (Illustration 9-1).

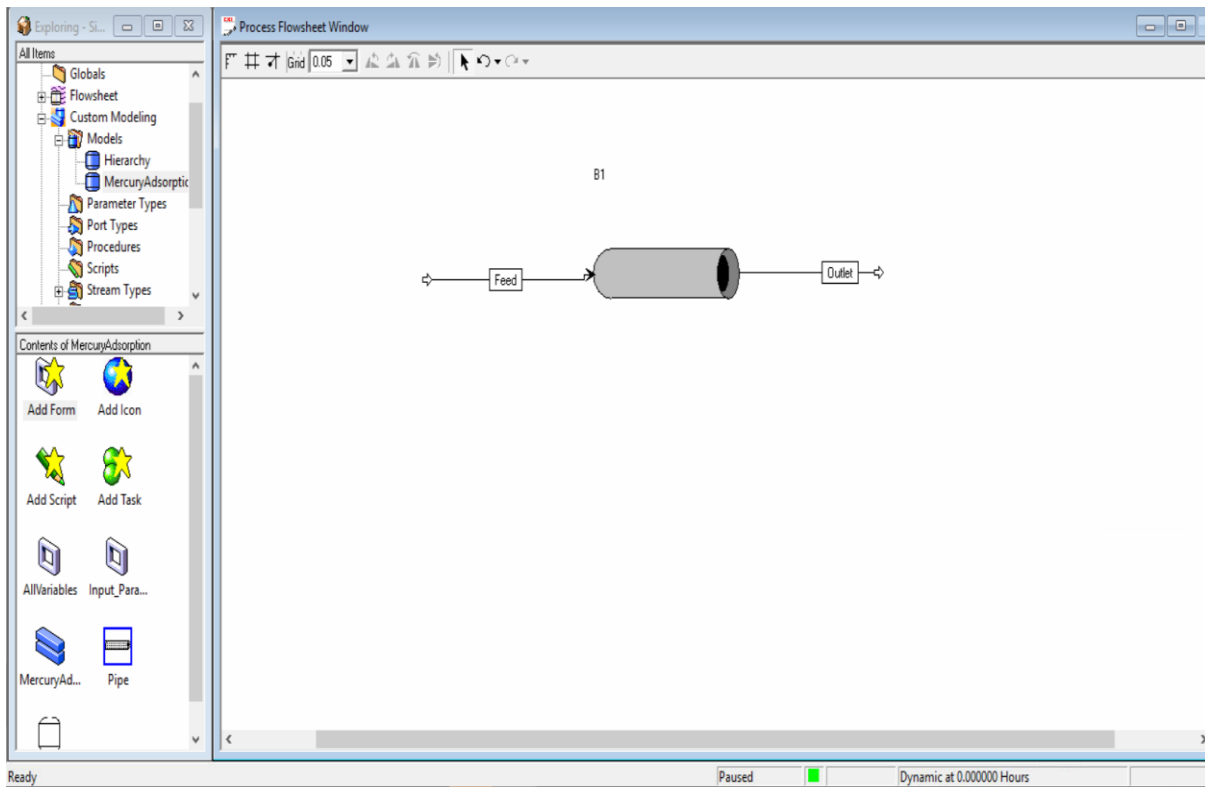
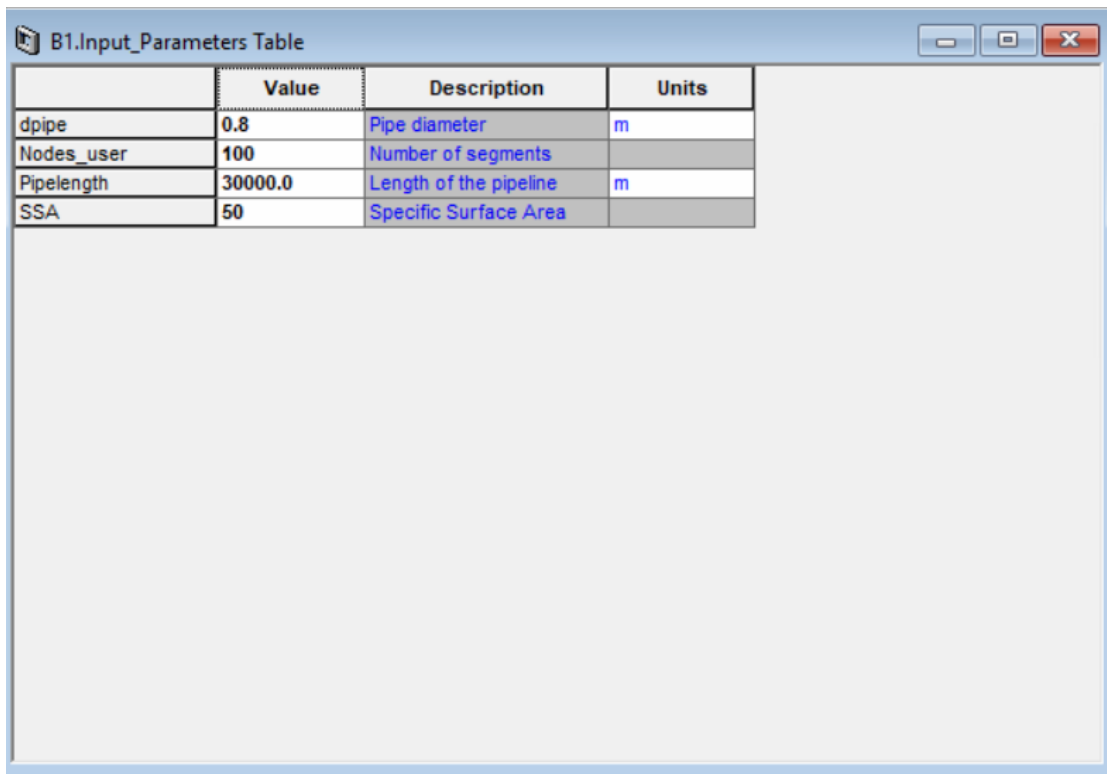


Illustration 9-1: The ACM mercury adsorption model flowsheet.

The flowsheet of the mercury adsorption model includes the pipeline block, as well as two streams connected to it, the “feed” and the “outlet” stream (Illustration 9-2). The other features of the model include a table named “Input Parameters” that lets the user define the pipeline geometry design, the Specific Surface Area of the pipe and the desired number of segments to be used, simply by double-clicking on the pipeline icon (Illustration 9-3). It is noted that opting for dense discretisation of the pipe results in accurate model solutions and high computational time. The evolution of the adsorption phenomenon in time is calculated in hours.



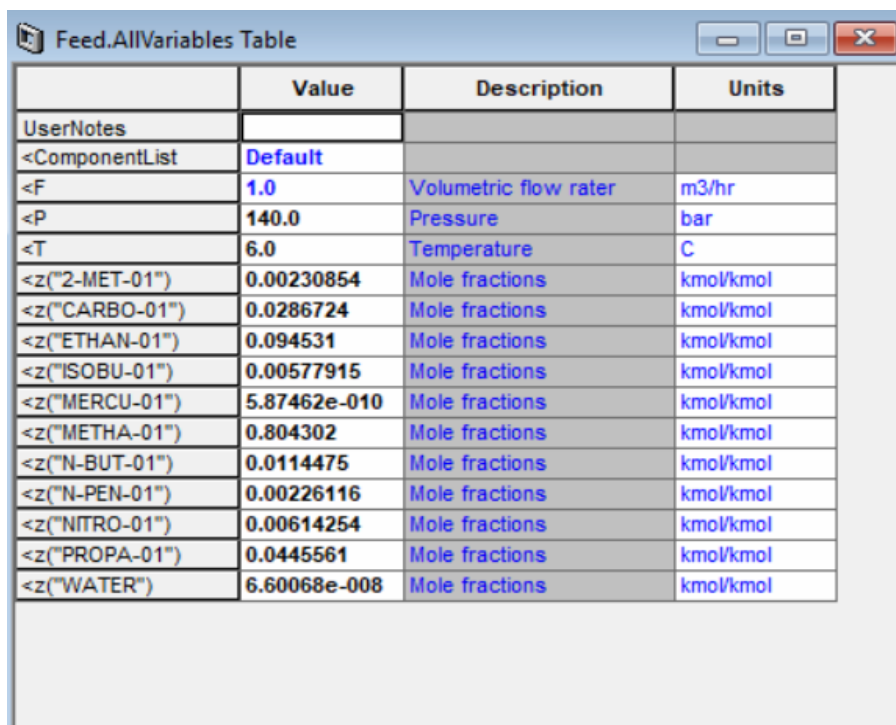
Illustration 9-2: Pipeline icon in ACM.



	Value	Description	Units
dpipe	0.8	Pipe diameter	m
Nodes_user	100	Number of segments	
Pipelength	30000.0	Length of the pipeline	m
SSA	50	Specific Surface Area	

Illustration 9-3: User-defined pipe characteristics and segmentation.

To run the model, the user shall insert, in the “feed” stream, the total inlet volumetric flowrate (F) in m³/h, the inlet pressure (P) in bar, the temperature of the feed (T) in °C, as well as the natural gas composition (z) in molar fractions, as pictured in Illustration 9-4.

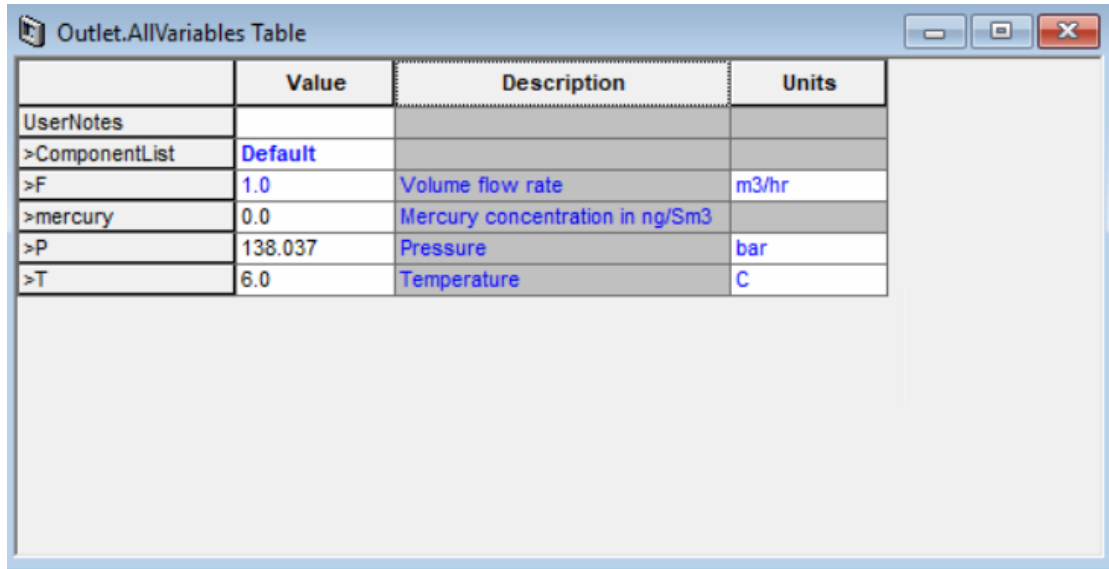


	Value	Description	Units
UserNotes			
<ComponentList	Default		
<F	1.0	Volumetric flow rater	m3/hr
<P	140.0	Pressure	bar
<T	6.0	Temperature	C
<z("2-MET-01")	0.00230854	Mole fractions	kmol/kmol
<z("CARBO-01")	0.0286724	Mole fractions	kmol/kmol
<z("ETHAN-01")	0.094531	Mole fractions	kmol/kmol
<z("ISOBU-01")	0.00577915	Mole fractions	kmol/kmol
<z("MERCU-01")	5.87462e-010	Mole fractions	kmol/kmol
<z("METHA-01")	0.804302	Mole fractions	kmol/kmol
<z("N-BUT-01")	0.0114475	Mole fractions	kmol/kmol
<z("N-PEN-01")	0.00226116	Mole fractions	kmol/kmol
<z("NITRO-01")	0.00614254	Mole fractions	kmol/kmol
<z("PROPA-01")	0.0445561	Mole fractions	kmol/kmol
<z("WATER")	6.60068e-008	Mole fractions	kmol/kmol

Illustration 9-4: User-defined feed inlet conditions.

In return, the model provides, at each time step, the concentration of Hg (mercury) at the outlet in ng/Sm³, the outlet volumetric flowrate (F), temperature (T) in °C and pressure (P) in bar, which can be found in “outlet” stream table (Illustration 9-5).

During the simulation, the plots for outlet mercury concentration with time and surface coverage along the pipeline are, simultaneously, produced.



	Value	Description	Units
UserNotes			
>ComponentList	Default		
>F	1.0	Volume flow rate	m3/hr
>mercury	0.0	Mercury concentration in ng/Sm3	
>P	138.037	Pressure	bar
>T	6.0	Temperature	C

Illustration 9-5: Outlet stream conditions in simulation time.

9.3. Validation of MATLAB Model Results

Prior to embarking on implementing the model for any given case, it is critical to determine whether the results of ACM are consistent with the developed model in MATLAB. To validate the results, at least one of the considered cases shall be tested. The attempt centres upon the reproduction of Case 1-0 results.

It shall be noted that a rigorous validation requires that the values of parameters used are the exact same in both cases. For this reason, procedural calls to the Aspen Physical Properties Engine are avoided and physical properties' values, such as fugacity and compressibility factor, are manually added. Time is measured in hours.

In Table 9-1, the time to breakthrough is reported. Figures 9-1 to 9-2 show the coverage of the pipe walls with mercury at the start of the phenomenon and around halfway through breakthrough. Figure 9-3 compares the adsorption front at breakthrough, as produced by the two models. The results of the model developed in MATLAB are identical to those of ACM. It is, subsequently, confirmed that the ACM model for mercury adsorption in natural gas pipelines is successfully developed.

Table 9-1: Time to breakthrough estimated by ACM and MATLAB.

Time to breakthrough (hours)	
Aspen Custom Modeler	35.3667
MATLAB	35.3661

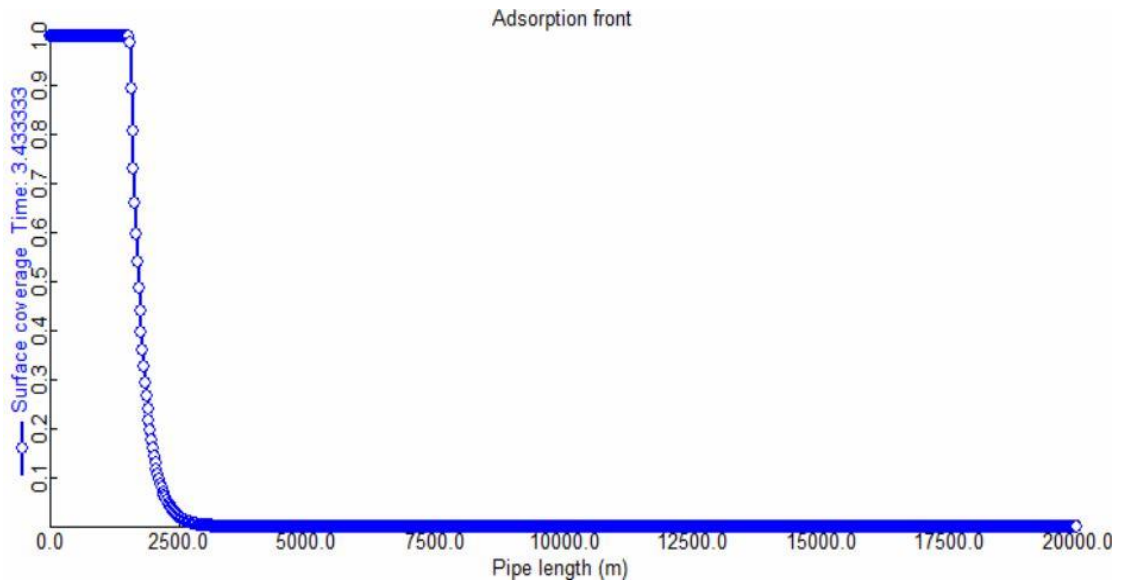


Figure 9-1: Adsorption front for Case 1-0 at the start of the phenomenon (3.43 hours), as produced in ACM.

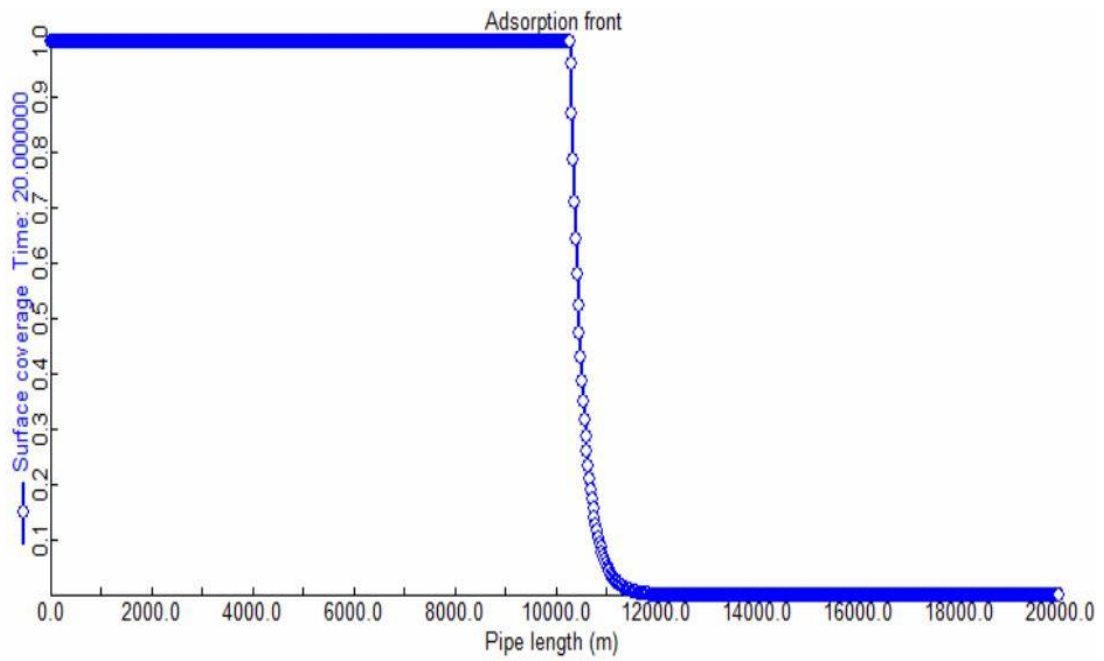


Figure 9-2: Adsorption front for Case 1-0 at 20 hours, as produced in ACM.

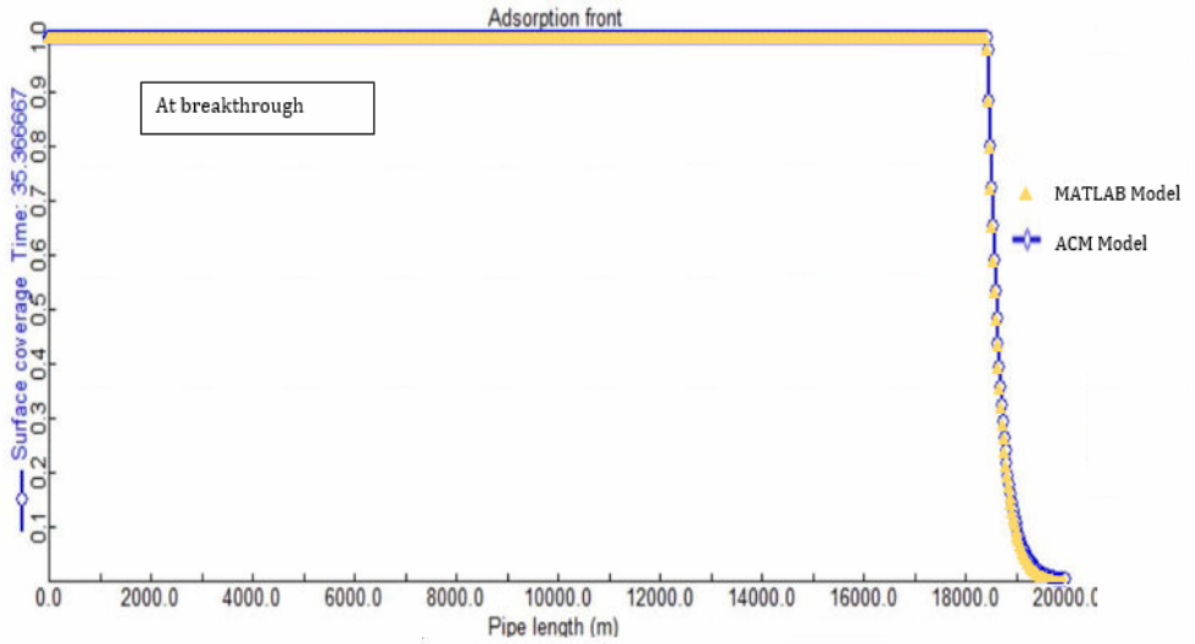


Figure 9-3: Comparison of adsorption front length at breakthrough, as produced in MATLAB and ACM.

9.4. ACM Model Testing

After successfully implementing the model in ACM, a Trial Case is performed. In Figures 9-5 and 9-6, the results of the simulation are reported. Breakthrough time, as well as inlet and outlet conditions can be found in Table 9-2, whilst the value of the parameters are detailed in the Appendix.

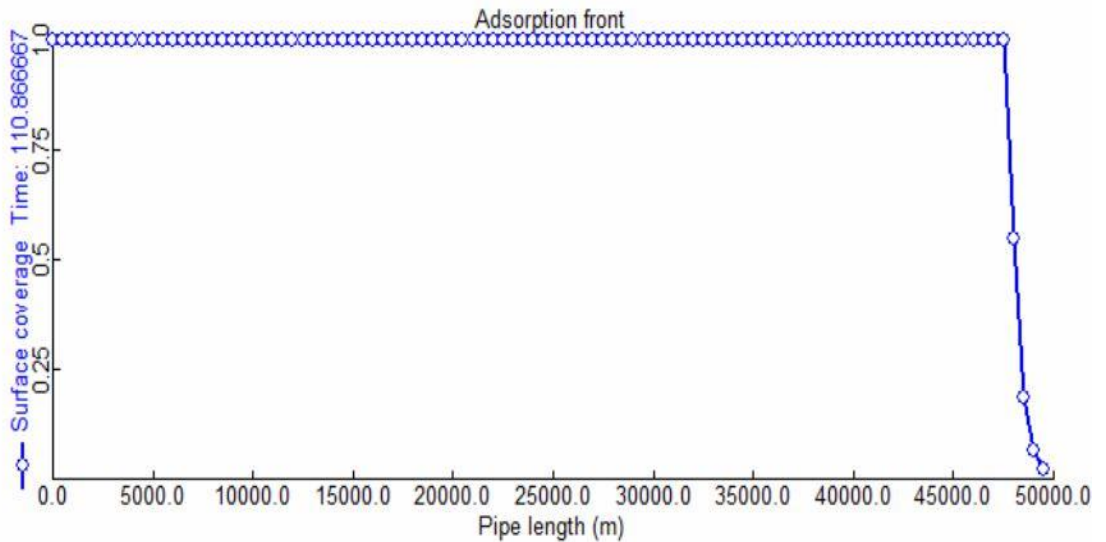


Figure 9-4: Adsorption front for Trial Case after breakthrough.

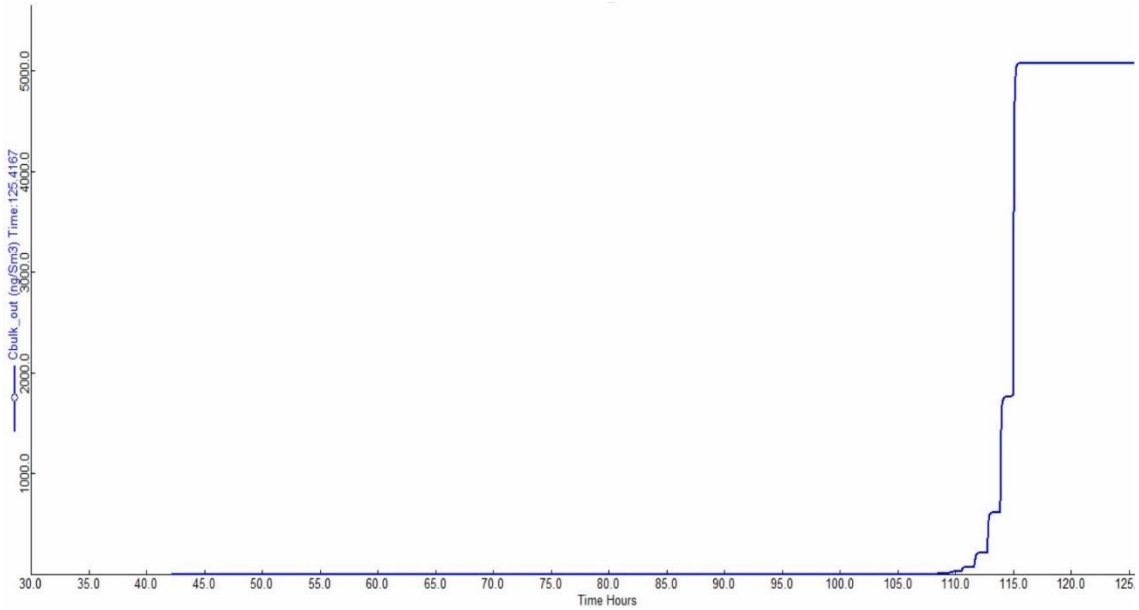


Figure 9-5: Mercury outlet concentration at steady state conditions.

Table 9-2: Data of Trial Case.

Parameter	Value
P_{in}	140.0 bara
P_{out}	137.7 bara
$F_{vol,in total}$	4000 m ³ /h
$F_{vol, out total}$	4013.3 m ³ /h
$C_{Hg,in}^{std}$	4992.27 ng/Sm ³
T	280.15 K
L	50,000 m
d_{pipe}	0.8 m
SSA	1
n	100
Breakthrough time	4.56 d
Composition	
Component	Molar fraction
Mercury	5.87462E-10
Carbon Dioxide	2.86724E-2
Methane	8.04302E-1
Ethane	9.4531E-2
Propane	4.45561E-2
i-butane	5.77915E-3
n-butane	1.14475E-2
i-pentane	2.30854E-3
n-pentane	2.26116E-3
Water	6.60068E-8
Nitrogen	6.14254E-3

The successful introduction of the adsorption model from MATLAB to Aspen Custom Modeler has proved to constitute a user-friendly tool, able to estimate breakthrough time for any given pipeline, natural gas composition and inlet conditions. Running the simulation in dynamic mode allows stakeholders to follow the adsorption process in real

time, while observing the development of the mercury adsorption front and the increase of mercury outlet concentration until full pipeline saturation. The ACM mercury adsorption model has, moreover, the potential to be exported as unit of the process units palette in ASPEN PLUS/Hysys [30] with the necessary modifications to fit the simulation environment.

10. CONCLUSIONS AND RECOMMENDATION

10.1. Conclusions

In the present Diploma Thesis, a model for mercury adsorption in natural gas pipelines was introduced. The adsorption and desorption processes of mercury onto steel pipe walls of a 20 km pipeline were studied for a range of mercury inlet concentrations between 100 and 5000 ng/Sm³ and considering different adsorption capacities reported in the research literature (0.0038-10 g/m²). The time taken to exceed the inlet specification limit of 10 ng/Sm³ at the entrance of the reception facility has been estimated for each case, and the time dependent concentration and surface coverage profiles have been reported.

The model, developed and solved in MATLAB, revealed that an increase in the mercury inlet concentration decreases breakthrough time at reception facilities, whereas increasing adsorption capacity of the pipe increases the time for mercury breakthrough, as it is expected by the theoretical background of adsorption process. An empirical equation for the prediction of the breakthrough time as a function of the mercury concentration in the pipeline inlet and Specific Surface Area (SSA) has been developed.

Due to a profound lack in real data on mercury adsorption on industrial pipelines, it was of paramount importance to investigate the effect on the assumptions used and parameters calculated, during model development. After a successful preliminary test of model's main parameters, a thorough parametric analysis reaffirmed the sensitivity of the model to the mass transfer coefficient and compressibility factor, whereas mercury fugacity coefficient and the thickness of the stagnant boundary layer appear to have, practically, no effect on the phenomenon.

Moreover, sensitivity analysis focused on kinetic parameters used to describe the adsorption and desorption process with emphasis on the dependence of the activation energy of desorption on the pre-exponential factor of desorption and surface coverage. The "compensation effect" between the activation energy of desorption and pre-exponential factor in the case of mercury on iron was investigated and confirmed. The interdependence of the aforementioned parameters imposes their use in pairs. A correlation between the activation energy and surface coverage showed signs of a second-order relation, however resulted in the same breakthrough time and adsorption front length, when a linear function was used. The above-mentioned shed light on the necessity for further research on mercury adsorption kinetics on steel in operating conditions.

The model was also implemented in Aspen Plus Custom Modeler. The thermodynamic model used is Peng-Robinson with zero binary interaction parameter. The molecular weight of the gas, its density, as well as mercury fugacity coefficient are calculated internally using Aspen Physical Properties Engine, which limits the volume and intensity of calculations performed in the model. Initially, the simulation was run in dynamic and steady state mode with fixed parameters, to validate MATLAB model results, at given composition, flowrate, pressure and temperature conditions and fixed parameters. The model results are successfully reproduced, thus, fostering the model extension to receive user input. For a successful run, the user needs to define stream inlet conditions, pipe characteristics and segmentation approach. The plots for surface coverage along the pipeline and outlet mercury concentration in time were created during each run, thus allowing the user to have a clear picture of the adsorption phenomenon in real time. The results of a Trial Case are reported. The successful implementation of the mercury adsorption model from MATLAB to Aspen Custom Modeler, not only provides estimates of mercury breakthrough for any tested pipeline, but also, constitutes an easy-to-use tool for pipeline simulation, developed in a rather commercial software.

10.2. Recommendations

Based on the conclusions of the present study, the following suggestions can be made for further improvement of the mercury adsorption model:

- Integration of chemical reactions of mercury with components present in natural gas, such as H_2S , or with localised compounds on the pipe wall. In this case, all possible methods of mercury uptake will be tested.
- Consideration of energy balances to allow the determination of a temperature profile, as temperature affects the adsorption phenomenon.
- Investigation of possibilities for experimental verification of the model and respective fitting of the model to field or experimental measurements.
- Laboratory analysis of a representative sample to determine SSA and the capacity of operating steel pipelines to adsorb mercury will increase confidence in the pipeline adsorption results.

REFERENCES

1. Radford, R., *Mercury Management and Chemical Decontamination [White Paper]*, ed. Retrieved May 28, from Portnoy Environmental, Inc. : <http://cdn2.hubspot.net/hub/22765/file-599028159-pdf/docs/mmsmercurydecontaminationwhitepaperfinal-100314092414-phppapp01.pdf>. 2010.
2. Wilhelm, S.M. and D.A. Kirchgessner, *Mercury in Petroleum and Natural Gas--estimation of Emissions from Production, Processing, and Combustion*. 2001: United States Environmental Protection Agency, National Risk Management.
3. Korkor, H., A. Ai-Alf, and S. Ei-Behairy. *Mercury Removal from Natural Gas in Egypt*. in *Prospects of Oil, Gas and Petrochemical Industries in the Arab Region: Opportunities and Challenges, Volume 1 and Volume 2*. 2004. Egypt.
4. S. Mark Wilhelm, *The interaction of mercury with metal surfaces-Engineering implications in Mercury Seminar*. 2009.
5. Dadashzadeh, M., et al., *An integrated approach for fire and explosion consequence modelling*. Fire Safety Journal, 2013. **61**: p. 324-337.
6. Falk, J. and D. Settle, *Australia: Approaching an energy crossroads*. Energy Policy, 2011. **39**(11): p. 6804-6813.
7. Gallup, D.L., D.J. O'Rear, and R. Radford, *The behavior of mercury in water, alcohols, monoethylene glycol and triethylene glycol*. Fuel, 2017. **196**: p. 178-184.
8. Radford, R., *Lessons learned in mercury management*. 2013 [cited 2019 06/10]; Available from: <https://www.hartenergy.com/exclusives/lessons-learned-mercury-management-19775>.
9. Panduan, G., *Guidelines on Mercury Management in Oil & Gas Industry*, D.o.O.S.a. Health, Editor. 2011, M.o.H.R. : Malaysia.
10. The Mathworks Inc., *Matlab – The Language of Technical Computing*. 2015.
11. Kumar, A. and A. Awasthi, *Bioseparation engineering*. 2009: IK International Pvt Ltd. pp. 96.
12. Fomkin, A.A., *Nanoporous materials and their adsorption properties*. Protection of Metals and Physical Chemistry of Surfaces, 2009. **45**(2): p. 133-149.
13. Levlin, M., E. Ikävalko, and T. Laitinen, *Adsorption of mercury on gold and silver surfaces*. Fresenius' journal of analytical chemistry, 1999. **365**(7): p. 577-586.
14. Orrling, D., *Towards Abatement of Selected Emissions from Metals Manufacturing*. 2010, KTH.
15. Roseborough, D., et al., *Surface chemistry of mercury on zinc and copper*. Metallurgical and Materials Transactions B, 2006. **37**(6): p. 1057-1066.
16. Jones, R. and D. Perry, *The chemisorption of mercury on Fe (100): adsorption and desorption kinetics, equilibrium properties and surface structure*. Vacuum, 1981. **31**(10-12): p. 493-498.
17. Roseborough, D., et al., *The surface behavior of mercury on iron systems*. Metallurgical and Materials Transactions B, 2006. **37**(6): p. 1049.
18. Jones, R.G. and D.L. Perry, *The chemisorption of mercury on tungsten (100): Adsorption and desorption kinetics, equilibrium properties and surface structure*. Surface Science, 1978. **71**(1): p. 59-74.
19. Wilhelm, M. and M. Nelson, *Interaction of Elemental Mercury with Steel Surfaces*. The Journal of Corrosion Science and Engineering, 2010. **13**.
20. Klosterman, S., *Modeling Adsorption and Its Effects on the Fate and Transport of Contaminants in a Water Distribution System*. 2009, University of Cincinnati.
21. Klosterman, S.T., et al., *Adsorption model for arsenate transport in corroded iron pipes with application to a simulated intrusion in a water distribution network*. Journal of Water Resources Planning and Management, 2013. **140**(5): p. 649-657.

22. Shang, F., J.G. Uber, and L.A. Rossman, *Modeling reaction and transport of multiple species in water distribution systems*. Environmental science & technology, 2007. **42**(3): p. 808-814.
23. Rossman, L.A., R.M. Clark, and W.M. Grayman, *Modeling chlorine residuals in drinking-water distribution systems*. Journal of environmental engineering, 1994. **120**(4): p. 803-820.
24. Rossman, L.A., *EPANET 2: users manual*. 2000.
25. Voutsas, E., K. Magoulas, and D. Tassios, *Universal Mixing Rule for Cubic Equations of State Applicable to Symmetric and Asymmetric Systems: Results with the Peng–Robinson Equation of State*. Industrial & Engineering Chemistry Research, 2004. **43**(19): p. 6238-6246.
26. Liu, Y., *Effects of Mesh Density on Finite Element Analysis*. Vol. 2. 2013.
27. Meissner III, R. and U. Wagner, *Low-energy process recovers CO/sub 2*. Oil Gas J.;(United States), 1983. **81**(5).
28. Chen, C.C. and P.M. Mathias, *Applied thermodynamics for process modeling*. AIChE Journal, 2002. **48**(2): p. 194-200.
29. Venkateshan, S.P. and P. Swaminathan, *Chapter 10 - Initial Value Problems*, in *Computational Methods in Engineering*, S.P. Venkateshan and P. Swaminathan, Editors. 2014, Academic Press: Boston. p. 385-446.
30. ASPEN Technology Inc. *ASPEN PLUS - Design and Steady State Simulation and Optimization*. Available from: <https://www.aspentech.com/en/products/engineering/aspens-plus>.
31. Rios, J.A., et al., *Removal of trace mercury contaminants from gas and liquid streams in the LNG and gas processing industry*. Conference: 77. annual meeting of the Gas Processors Association (GPA), Dallas, TX (United States), 16-18 Mar 1998; Other Information: PBD: [1998]; Related Information: Is Part Of Seventy-seventh annual convention Gas Processors Association: Proceedings; PB: 288 p. 1998: Gas Processors Association, Tulsa, OK (United States). Medium: X; Size: pp. 191-196.
32. Koulocheris, V., et al., *Modelling of elemental mercury solubility in natural gas components*. Fuel, 2018. **233**: p. 558-564.
33. Tareq, R., N. Akter, and M.S. Azam, *Chapter 10 - Biochars and Biochar Composites: Low-Cost Adsorbents for Environmental Remediation*, in *Biochar from Biomass and Waste*, Y.S. Ok, et al., Editors. 2019, Elsevier. p. 169-209.
34. Cerofolini, G.F. and W. Rudziński, *Chapter 1. Theoretical principles of single- and mixed-gas adsorption equilibria on heterogeneous solid surfaces*, in *Studies in Surface Science and Catalysis*, W. Rudziński, W.A. Steele, and G. Zgrablich, Editors. 1997, Elsevier. p. 1-103.
35. Banerjee, S., et al., *11 - Super-Strong, Super-Modulus Materials*, in *Functional Materials*, S. Banerjee and A.K. Tyagi, Editors. 2012, Elsevier: London. p. 467-505.
36. Weissenrieder, J., *Division of Materials and Semiconductor Physics*. 2003, KTH: Stockholm.
37. Hu, X., et al., *Chapter 8 - Hydrogen Adsorption and Storage*, in *Coal Gasification and Its Applications*, D.A. Bell, B.F. Towler, and M. Fan, Editors. 2011, William Andrew Publishing: Boston. p. 157-245.
38. Ghosh, P., *Adsorption at Fluid–Solid Interface*. 2013, NPTEL, Chemical Engineering.
39. Stuckless, J.T., et al., *Oxygen chemisorption and oxide film growth on Ni{100}, {110}, and {111}: Sticking probabilities and microcalorimetric adsorption heats*. The Journal of Chemical Physics, 1997. **106**(5): p. 2012-2030.
40. Lüth, H. and H. Lèuth, *Solid surfaces, interfaces and thin films*. Vol. 4. 2001: Springer.
41. Pal, P., *Chapter 4 - Physicochemical Treatment Technology*, in *Industrial Water Treatment Process Technology*, P. Pal, Editor. 2017, Butterworth-Heinemann. p. 145-171.

42. Mokhatab, S., W.A. Poe, and J.Y. Mak, *Chapter 9 - Natural Gas Dehydration and Mercaptans Removal*, in *Handbook of Natural Gas Transmission and Processing (Fourth Edition)*, S. Mokhatab, W.A. Poe, and J.Y. Mak, Editors. 2019, Gulf Professional Publishing. p. 307-348.
43. Ozkaya, B., *Adsorption and desorption of phenol on activated carbon and a comparison of isotherm models*. J Hazard Mater, 2006. **129**(1-3): p. 158-63.
44. Singh, K.P., et al., *Liquid-phase adsorption of phenols using activated carbons derived from agricultural waste material*. J Hazard Mater, 2008. **150**(3): p. 626-41.
45. Ballantine, D.S., et al., *Chapter 5 - Chemical and Biological Sensors*, in *Acoustic Wave Sensors*, D.S. Ballantine, et al., Editors. 1997, Academic Press: Burlington. p. 222-330.
46. Christmann, K., *Introduction to surface physical chemistry*. Vol. 1. 2013: Springer Science & Business Media.
47. Redhead, P., *Thermal desorption of gases*. vacuum, 1962. **12**(4): p. 203-211.
48. Temmerman, E., et al., *Sensitive determination of gaseous mercury in air by cold vapour atomic fluorescence spectrometry after amalgamation*. Analytica chimica acta, 1990. **236**: p. 371-376.
49. Levlin, M., et al., *Mercury adsorption on gold surfaces employed in the sampling and determination of vaporous mercury: a scanning tunneling microscopy study*. Fresenius' journal of analytical chemistry, 1996. **355**(1): p. 2-9.
50. Nowakowski, R., et al., *Atomic force microscopy of AuHg alloy formation on thin Au films*. Applied surface science, 1997. **115**(3): p. 217-231.
51. Battistoni, C., et al., *Interaction of mercury vapour with thin films of gold*. Applied surface science, 1996. **103**(2): p. 107-111.
52. Massalski, T.B., et al., *Binary alloy phase diagrams*. 1986, Metals Park, Ohio: American Society for Metals.
53. Dowben, P.A., et al., *The energetics of mercury adsorption on Cu(100)*. Surface Science, 1990. **230**(1): p. 113-122.
54. Paliwal, V.K., A.G. Vedeshwar, and S.M. Shivaprasad, *Residual thermal desorption study of the room-temperature-formed Sb/Si(111) interface*. Physical Review B, 2002. **66**(24): p. 245404.
55. Pierce, M.L. and C.B. Moore, *Adsorption of arsenite and arsenate on amorphous iron hydroxide*. Water Research, 1982. **16**(7): p. 1247-1253.
56. F. Shang, J.G.U., L. Rossman, *EPANET Multi-Species Extension Software and User's Manual*. 2008, U.S. Environmental Protection Agency: Washington, DC.
57. Shang, F., J.G. Uber, and L. Rossman, *EPANET multi-species extension user's manual*. Risk Reduction Engineering Laboratory, US Environmental Protection Agency, Cincinnati, Ohio, 2008.
58. Yates Jr, J., *Methods of experimental physics*. Solid State Physics: Surfaces, 1985. **22**: p. 425-464.
59. Guo, X. and J.T. Yates Jr, *Dependence of effective desorption kinetic parameters on surface coverage and adsorption temperature: CO on Pd (111)*. The Journal of Chemical Physics, 1989. **90**(11): p. 6761-6766.
60. Niemantsverdriet, J.W., K. Markert, and K. Wandelt, *The compensation effect and the manifestation of lateral interactions in thermal desorption spectroscopy*. Applied Surface Science, 1988. **31**(2): p. 211-219.
61. Sahu, O. and N. Singh, *13 - Significance of bioadsorption process on textile industry wastewater*, in *The Impact and Prospects of Green Chemistry for Textile Technology*, I. Shahid ul and B.S. Butola, Editors. 2019, Woodhead Publishing. p. 367-416.
62. Zielinski, J.M. and L. Kettle, *Physical characterization: surface area and porosity*. London: Intertek, 2013.
63. Fagerlund, G., *Determination of specific surface by the BET method*. Vol. 6. 1973. 239-245.

64. Louli, V., et al., *Application of the UMR-PRU model to multicomponent systems: Prediction of the phase behavior of synthetic natural gas and oil systems*. Fluid Phase Equilibria, 2007. **261**(1): p. 351-358.
65. Michelsen, M.L., *A modified Huron-Vidal mixing rule for cubic equations of state*. Fluid Phase Equilibria, 1990. **60**(1): p. 213-219.
66. Louli, V., et al., *Measurement and prediction of dew point curves of natural gas mixtures*. Fluid Phase Equilibria, 2012. **334**: p. 1-9.
67. Petropoulou, E., G.D. Pappa, and E. Voutsas, *Modelling of phase equilibrium of natural gas mixtures containing associating compounds*. Fluid Phase Equilibria, 2017. **433**: p. 135-148.
68. Underwood, C., *The MATLAB Handbook*. 2016: CreateSpace Independent Publishing Platform. 114.
69. Thimmannagari, C., *CPU design: answers to frequently asked questions*. 2004: Springer Science & Business Media.
70. Johnson, R.W., *Handbook of fluid dynamics*. 2016: Crc Press.
71. NIST Chemistry WebBook. *Thermophysical Properties of Fluid Systems*. 2018 July 15, 2018]; Available from: <https://webbook.nist.gov/chemistry/fluid/>.
72. Brown, G., *The History of the Darcy-Weisbach Equation for Pipe Flow Resistance*. Vol. 38. 2002.
73. Petukhov, B., *Heat transfer and friction in turbulent pipe flow with variable physical properties*, in *Advances in heat transfer*. 1970, Elsevier. p. 503-564.
74. Edwards, D.K., V.E. Denny, and A.F. Mills, *Transfer processes. an introduction to diffusion, convection and radiation*. Series in Thermal and Fluids Engineering, New York: McGraw-Hill, and Washington: Hemisphere Publication Co., 1978, 2nd ed., 1978.
75. Geankoplis, C.J., *Transport processes and separation process principles:(includes unit operations)*. 2003: Prentice Hall Professional Technical Reference.
76. Whitty K., *Lecture notes on "Heat Transfer"*. 2014, The University of Utah.
77. Thirumaleshwar, M., *Fundamentals of heat and mass transfer*. 2006: Pearson Education India.
78. Kraft M.L., *Power Point slides on "External Diffusion Effects"*. 2017, University of Illinois.
79. Poling, B.E., J.M. Prausnitz, and J.P. O'connell, *The properties of gases and liquids*. Vol. 5. 2001: Mcgraw-hill New York.
80. Wegner. K., *Lecture on Mass Transfer: Estimation of Diffusivities*. 2017, ETH Zurich.
81. Cussler, E.L., *Diffusion: mass transfer in fluid systems*. 2009: Cambridge university press.
82. Hirschfelder, J.O., R.B. Bird, and E.L. Spotz, *The transport properties for non-polar gases*. The Journal of Chemical Physics, 1948. **16**(10): p. 968-981.
83. Pavlin, T., *Hyperpolarized gas polarimetry and imaging at low magnetic field*. 2003, California Institute of Technology.
84. Lee, A.L., M.H. Gonzalez, and B.E. Eakin, *The viscosity of natural gases*. Journal of Petroleum Technology, 1966. **18**(08): p. 997-1,000.
85. Twu, C.H., et al., *CEOS/AE mixing rules from infinite pressure to zero pressure and then to no reference pressure*. Fluid Phase Equilibria, 1999. **158**: p. 271-281.
86. Pohlhausen, E., *Der Wärmeaustausch zwischen festen Körpern und Flüssigkeiten mit kleiner reibung und kleiner Wärmeleitung*. ZAMM - Journal of Applied Mathematics and Mechanics / Zeitschrift für Angewandte Mathematik und Mechanik, 1921. **1**(2): p. 115-121.
87. ASPEN Technology Inc., *Aspen Custom Modeler Modeling Language Reference Guide*. 2005.

APPENDIX

MATLAB Model Values

Symbol	Value	Unit
P_{in}	143.2	bara
P_{out}	141.3	bara
T	6	°C
L	20000	m
d_{pipe}	711.2	mm
δ	2.13E-05	m
δ_c	4.25E-05	m
$F_{vol\ total,in}^{std}$	24E6	Sm ³ /d
$F_{vol,in}$	1.1586	m ³ /s
$F_{vol,out}$	1.1738	m ³ /s
$E_{a,desorption}$	151-28.820	kJ/mol
n	800	-
ν	1.0E17	1/s
Z	0.6074	-
$\varphi^{V_{Hg}}$	0.144992321	-
ρ	205.3-207.98	kg/m ³
μ	2.15E-5-2.18E-5	kg/m·s
D	8.92314E-8	m ² /s
Sc	1.1665	-
Sh	1.16650027541785	-
SSA	1-2632	m ² /m ²
N_{max}	1.2140E19	atoms/m ²
$C_{Hg,in}^{std}$	100-5000	ng/Sm ³
S_0	1	-
$M_{w,Hg}$	0.20059	kg/mol
$C_{max,out}^{std}$	10	ng/Sm ³
k_m	0.0021	m/s
f_D	0.0074	-
u_{in}	2.9165	m/s
u_{out}	2.9546	m/s
Re_{in}	1.9786E7	-
Re_{out}	2.0038E7	-

ACM Model Values for Trial Case

Symbol	Value	Unit
$F_{vol,in}$	1.1111	m ³ /s
$F_{vol,out}$	1.1299	m ³ /s
$E_{a,desorption}$	151-28.820	kJ/mol
ν	1.0E17	1/s
Z	0.6086	-
$\varphi^{V_{Hg}}$	0.13137	-
ρ	198.8-202.2	kg/m ³
μ	2.09E-5-2.12E-5	kg/m·s

D	9.1726E-008	m ² /s
SSA	1	m ² /m ²
N _{max}	1.2140E19	atoms/m ²
s ₀	1	-
M _{w,Hg}	0.20059	kg/mol
C _{max,out} ^{std}	10	ng/Sm ³
k _m	0.00167	m/s
f _D	0.0075	-
u _{in}	2.2105	m/s
u _{out}	2.2478	m/s
Re _{in}	1.68332E7	-
Re _{out}	1.70992E7	-